ALMA MATER STUDIORUM
UNIVERSITÀ DI BOLOGNA

DOTTORATO DI RICERCA IN

INGEGNERIA E TECNOLOGIA DELL'INFORMAZIONE PER IL MONITORAGGIO STRUTTURALE E AMBIENTALE E LA GESTIONE DEI RISCHI - EIT4SEMM

Ciclo 37

Settore Concorsuale: 09/F1 - CAMPI ELETTROMAGNETICI

Settore Scientifico Disciplinare: ING-INF/02 - CAMPI ELETTROMAGNETICI

INTELLIGENT WALLS BY THE USE OF RECONFIGURABLE INTELLIGENT SURFACES

Presentata da: Silvi Kodra

Coordinatore Dottorato

Luca De Marchi

Supervisore

Vittorio Degli Esposti

Co-supervisore

Marina Barbiroli

Esame finale anno 2025

I would like to dedicate this thesis to my loving partner and family ...

Declaration

I hereby declare that except where specific reference is made to the work of others, the contents of this dissertation are original and have not been submitted in whole or in part for consideration for any other degree or qualification in this, or any other university. This dissertation is my own work and contains nothing which is the outcome of work done in collaboration with others, except as specified in the text and Acknowledgements. All research work presented in this dissertation has been published or submitted for publication in IEEE journals or conference proceedings, as cited throughout the thesis.

Silvi Kodra
February 2025

Acknowledgements

I would like to express my heartfelt gratitude to all the members of my research group for their constant support and encouragement throughout these three years. First and foremost, my sincere thanks go to my supervisor, Prof.Vittorio Degli-Esposti, and my co-supervisor, Prof.Marina Barbiroli, for the trust they placed in me and the collaborative, positive work environment they cultivated. I am grateful for them being such remarkable mentors, always ready with advice and assistance. Their experience and openness have greatly enriched my PhD journey. Their guidance and countless late hours spent together-especially in the intense days before deadlines-were invaluable, and I could not have achieved the same outcomes without their insights and dedication.

Going through the challenges of a PhD is far from easy, with many ups and downs, and I am incredibly thankful to my partner for his steadfast support. His presence was truly essential in helping me through the toughest moments. Lastly, I extend my thanks to my friends and colleagues around the world. The times we shared, whether in laughter or engaging conversations about our research, have made this journey all the more meaningful. And, not to be forgotten, I would like to thank myself for not giving up, even in the hardest moments when everything felt impossible.

Abstract

The convergence of advancements in the construction industry with the growing demands of wireless communication technologies is central to the development of next-generation networks. However, modern construction techniques often hinder signal propagation, and as transmission frequencies shift higher in the spectrum, achieving reliable coverage becomes increasingly challenging. These challenges underscore the urgent need for innovative techniques to enhance signal penetration and RF coverage within buildings. To this aim, this thesis explores macroscopic but yet realistic models for the design and integration of Reconfigurable Intelligent Surfaces (RIS) into buildings structures, offering a novel approach to addressing the signal propagation challenges faced in higher frequency bands such as those utilized in 5G and 6G networks. RIS, which can be embedded within walls, windows, and other architectural elements, provides a flexible and energy-efficient solution for enhancing wireless communication by dynamically shaping electromagnetic wave behavior. This dissertation positions RIS as a key technology in the future of smart building design, where construction and communication needs intersect.

A significant part of this research focuses on the development of macroscopic RIS models: a Huygens based bilateral (both for reflective and transmissive RIS) model and a ray-based macroscopic model that simulates signal re-radiation through reflective RIS. The latter is validated against existing physical optics methods, demonstrating high accuracy while maintaining computational efficiency. This thesis highlights the potential to optimize indoor and outdoor wireless coverage in a way that complements modern architectural trends by integrating RIS into building structures. Additionally, experimental studies were conducted to assess material penetration losses across multiple frequency bands, specifically mm-wave and sub-THz. The results indicate substantial signal attenuation through common construction materials which further underscores the importance of intelligent surface deployment in overcoming these obstacles.

By aligning advancements in construction with the needs of wireless communication, this thesis presents RIS as a potential transformative solution for modern urban environments. The proposed framework not only addresses the challenges of high-frequency signal propagation but also emphasizes the possibility of integrating communication technologies within building

designs. This work is a contribution to the development of smart buildings and cities, where architectural innovations and wireless communication systems work in harmony to support future applications, including autonomous systems, virtual reality, and the massive Internet of Things (IoT).

Table of contents

List of figures

List of tables

Nomenclature

Greek Symbols

j	unit imaginary number $\sqrt{-1}$
λ	wavelength
π	$\simeq 3.14\ldots$
$\sum$	Summation symbol

Other Symbols

e	Exponential function
GHz	Giga Hertz
std	Standard deviation

Acronyms / Abbreviations

$1G$	First generation of wireless networks
$2G$	Second generation of of wireless networks
$3G$	Third generation of wireless networks
$3GPP$	3rd Generation Partnership Project
$4G$	Fourth generation of wireless networks
$5G$	Fifth generation of wireless networks
$6G$	Sixth generation of wireless networks
AAL	Antenna Array-Like

ARSB Anomalous Reflection Shadow Boundary

BEL Building Entry Loss

BPL Building Penetration Loss

FEM Finite Element Method

GO Geometrical Optics

ISB Incidence Shadow Boundary

ITU International Telecommunication Union

LTE Long-Term Evolution

MEMS Micro Electro-Mechanical Systems

mm − wave Millimeter Wave

O2I Outdoor to Indoor

PEC Perfect Electric Conductor

PGM Phase Gradient Metasurface

PO Physical Optics

RF Radio Frequency

RIS Reconfigurable Intelligent Surfaces

RL Ray Launching

RMS Root Mean Square

RSB Reflection Shadow Boundary

RX Receiver

SB Shadow Boundary

SMC Spatial Modulation Coefficient

SMS Short Message Service

sub − THz Sub-Terahertz

TE Transverse Electric

TEM Trasverse Electro Magnetic

TM Transverse Magnetic

TX Transmitter

UTD Uniform Theory of Diffraction

Introduction

Open research questions

The primary objective of this thesis is to explore solutions for enhancing indoor wireless coverage in the context of future mobile networks operating at high frequencies. To achieve this, two distinct yet complementary goals are defined: 1) Investigate Reconfigurable Intelligent Surfaces as a potential technology to mitigate poor indoor coverage by engineering wireless propagation. 2) Address Outdoor-to-Indoor signal propagation challenges at mm-Wave and sub-THz frequencies, focusing on attenuation by construction materials. Therefore, this thesis facilitates the understanding and possible practical implementation of Reconfigurable Intelligent Surfaces in future smart building designs. This research seeks to answer the following open research questions:

- How can macroscopic models be developed to accurately and efficiently characterize the physically consistent behavior of Reconfigurable Intelligent Surfaces, accounting for both reflective and transmissive functionalities?
- What are the macroscopic parameters governing the performance of Reconfigurable Intelligent Surfaces in real-world deployments, and how can they be effectively incorporated into system simulations?
- How can Reconfigurable Intelligent Surfaces be designed and strategically deployed to enhance indoor wireless coverage?
- To what extent and how do different construction materials interact with mid-band and high-frequency signal?

Key Scientific Contributions

- Introduction of a heuristic macroscopic Huygens-based bilateral model for both reflective and transmissive modes, providing a computationally efficient way to analyze Reconfigurable Intelligent Surfaces impact in wireless networks.
- Development of a more rigorous ray-based macroscopic model to simulate the scattering effects of Reconfigurable Intelligent Surfaces in reflection mode, offering a balance between accuracy and computational efficiency compared to full-wave electromagnetic methods.
- An in-depth evaluation of signal attenuation due to different building materials at mm-Wave and sub-THz frequencies is conducted, emphasizing the impact of structural materials on signal penetration.
- A detailed analysis of the 3GPP TR 138 901 model reveals its underestimation of building penetration loss as the mobile terminal moves indoors, particularly in dense south-European building structures, leading to the proposal of a new frequency-dependent model for Outdoor-to-Indoor penetration.
- A first-attempt model for through-floor propagation loss is introduced, accounting for building type and emphasizing the growing challenges for attenuation in modern, highly insulated structures.

Chapter 1

From conventional to smart propagation environments

1.1 Signal propagation in future wireless generation

The continuous evolution of wireless communication has been a fundamental driver of progress in society and technology, transforming how we interact, work, and innovate. As we move toward an increasingly interconnected world, emerging applications such as autonomous systems, virtual reality, and massive Internet of Things deployments demand ever-greater bandwidth, lower latency, and higher reliability. These advancements, however, are pushing current wireless technologies to their limits, exposing significant challenges that the next generation, 6G, is envisioned to overcome, offering transformative capabilities over its predecessors.

To understand the need for 6G, it is essential to trace the development of mobile network generations (see Fig.1.1). 1G, deployed in the early 1980s, introduced analog voice communication, enabling mobile telephony for the first time. However, 1G networks were characterized by poor voice quality, limited coverage, and lack of security, as well as the complete absence of data services. The transition to 2G networks in the 1990s marked a pivotal shift from analog to digital communication. 2G provided enhanced voice quality, greater capacity, and secure communication. More importantly, it introduced SMS and basic data services, laying the groundwork for the integration of mobile internet. However, the bandwidth limitations of 2G soon became apparent, especially as consumer demand for data-intensive applications began to rise. 3G networks, launched in the early 2000s, addressed the growing need for mobile data by offering higher data rates and enabling internet browsing, video calls, and multimedia messaging. Network efficiency and data throughput

Fig. 1.1 Mobile Networks Evolution from 1G to 5G

were greatly improved, facilitating the rise of smartphones and app-driven ecosystems. Yet, despite its advances, 3G struggled to meet the increasing demands of real-time applications and high-bandwidth services. The introduction of 4G networks, specifically through LTE in the 2010s, revolutionized mobile communication by providing broadband-like speeds to mobile devices. This leap enabled a wide range of new applications, from high-definition video streaming to cloud-based services and the Internet of Things. However, even with these improvements, 4G networks began to encounter bottlenecks in densely populated areas and latency-sensitive applications, leading to the development of 5G. 5G networks are currently being deployed worldwide and promise unprecedented speeds, ultra-low latency, and the capacity to support massive device connectivity. However, 5G is not without its limitations: it still cannot meet the extremely low-latency requirements of emerging applications such as real-time industrial automation, and remote surgeries. As we approach the physical and architectural limits of 5G, the necessity for sixth-generation (6G) networks becomes apparent. Central to promise of 6G is the exploration and utilization of higher frequency bands. These high-frequency bands, while providing vast unused bandwidth, introduce significant propagation challenges, particularly in terms of signal coverage in complex and harsh environments. This is because high-frequency signals have significantly different propagation characteristics compared to lower-frequency signals. While they offer higher data rates and capacity due to their shorter wavelengths and larger available bandwidth, they are prone to severe path loss, which limits their effective range. Moreover, the propagation of high-frequency signals is heavily influenced by environmental factors such as obstacles that give rise to phenomena such as reflection, diffraction, and absorption of the signal. One of the most notable limitations of high-frequency signals is their inability to penetrate common building materials, a problem that becomes increasingly critical as modern society spends most of its time in indoor environments where seamless connectivity is expected. As a consequence, even though mm-Wave and sub-THz communication systems represent a promising frontier in wireless technologies, the upper mid-band within the 7-24 GHz range (known as FR3 band) has gained importance as it has emerged as a possible candidate for early 6G applications [1].

In parallel to the developments in wireless technology, the design and construction of modern buildings introduce further complexities for signal propagation. The use of advanced materials for energy efficiency and sustainability, such as Low-Emissivity glass, steel-reinforced concrete, and multilayer insulation, often aggravates the attenuation of high-frequency signals [2–4]. Moreover, the trend towards denser urban environments, with skyscrapers and multilayered infrastructure, introduces additional challenges in ensuring reliable signal coverage [5–7]. Since 80% of data traffic originates within indoor environments [8], understanding how different frequencies interact with various indoor structures and building materials is crucial for effective coverage planning [9, 10]. While the increase in isotropic free-space path loss with frequency is well-known, the attenuation a signal goes through due to the presence of building materials between transmitter and receiver is less straightforward [11]. Surprisingly, some materials exhibit minimal losses even at high frequencies, challenging common assumptions. Therefore it is crucial to understand the interaction mechanisms induced by the building materials. The consideration of future building construction materials and techniques is essential, as the architectural environment can no longer be viewed as separate from the technological ecosystem. The symbiotic relationship between building design and wireless network deployment will become a critical factor in the performance of next-generation wireless networks.

From these parallel developments in wireless and construction technologies, significant questions araise about how to balance the push for more sustainable and energy-efficient building practices with the need for uninterrupted and reliable high-frequency signal propagation. To that end, it is necessary to develop new solutions that can address these challenges. Various approaches have been explored for indoor coverage improvement, which can generally be categorized into active and passive solutions.

Active solutions, such as repeaters, indoor base stations and novel antenna designs have been under investigation. These methods are effective in overcoming indoor penetration losses but require additional infrastructure, increased power consumption, and careful interference management. Indoor base stations offer the highest capacity and dedicated coverage but come with high deployment and maintenance costs, energy consumption and interference challenges [12]. Repeaters provide a cost-effective alternative by amplifying outdoor signals, though they may require a power source and energy consumption remains still an issue [13]. Novel antenna designs, such as beamforming and MIMO-enabled systems, enhance signal propagation and adaptability but may be complex and costly to implement [14]. Passive solutions, on the other hand, aim to facilitate signal penetration without active amplification. Examples include signal-transparent windows [15] and passive antenna systems embedded in walls [16] [17] . The latter present a seamless and energy-efficient approach by integrating

passive antenna systems directly into building structures, though building modifications are required for this solution. While these passive methods are energy-efficient and seamlessly integrated into building design, their adaptability across different deployment scenarios may be limited due to cost constraints or the need for modifications to existing structures. In contrast, Reconfigurable Intelligent Surfaces (RIS) offer a paradigm shift by enabling dynamic control over the wireless environment while maintaining low power consumption [18–22]. This flexibility makes RIS a promising candidate for coverage enhancement, particularly in environments where infrastructure deployment is limited or impractical. By coating buildings with RIS, also known as 'Smart Skins,' and thereby creating the base technology for Smart Radio Environments (SRE), it will be possible to improve signal coverage for the end user (see [23] for more details), even in Non-Line-of-Sight (NLoS) conditions, as depicted in Fig.1.2.

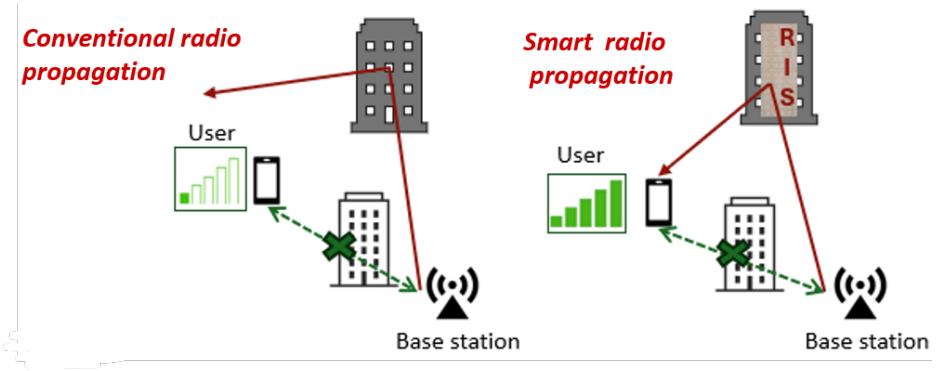

Fig. 1.2 Conventional versus Smart Radio Environment

1.2 From metamaterials to metasurfaces

Throughout history, humans have sought to control and manipulate waves, from the design of ancient Greek amphitheaters that enhanced acoustics, to early uses of lenses and mirrors in ancient Egypt and Greece, laying the foundations of classical optics. These early attempts evolved over centuries, but it was in the 19th century that James Clerk Maxwell's revolutionary theory of electromagnetism [24] provided the foundation for modern wave manipulation. This understanding paved the way for the development of materials specifically engineered to control these waves in ways previously thought impossible. One such breakthrough was the advent of metamaterials, derived from the Greek word *meta*, meaning "beyond" [25], indicating that these materials exhibit properties surpassing those found in natural materials. Metamaterial structures were designed to manipulate the interaction of electromagnetic and

other types of waves when impinging upon them. Metamaterials, first conceptualized by Victor Veselago in 1968 [26], introduced the possibility of negative refraction—a phenomenon in which electromagnetic wave bends in the opposite direction at an interface compared to natural materials. Veselago's work predicted that a material with both negative permittivity and negative permeability could exhibit this unusual property. In the late 1990s and early 2000s, John Pendry advanced Veselago's theoretical work by developing artificial structures capable of exhibiting negative refraction through engineered subwavelength elements such as split-ring resonators. In his landmark paper [27], Pendry demonstrated that metamaterials could overcome the diffraction limit, allowing for super-resolution imaging by focusing both propagating and evanescent waves. This breakthrough linked negative refraction to practical applications like super-lenses and invisibility cloaks, establishing metamaterials as a key field in controlling electromagnetic waves. The aforementioned developments in metamaterial technology paved the way for metasurfaces, a two-dimensional counterpart to metamaterials [25] [28], enabling simpler and more efficient manipulation of electromagnetic waves.

1.3 Key properties of metasurfaces

A metasurface is an engineered two-dimensional thin structure, consisting of a substrate with a distribution of electrically small (i.e, smaller than the wavelength) metal or dielectric patches printed on it, called meta atoms [29]. These meta-atoms can have various shapes, such as spiral, square, rectangular and H-shape. The shape and the size of meta-atoms vary over the surface in order to achieve a desired effect on the wavefront of the re-radiated wave when the surface is illuminated by an incident wave. Metasurfaces aimed at reflecting an incident wave are defined as "Reflective Metasurfaces", whereas those conceived to transmit a wave are defined as "Transmissive Metasurfaces" or "Huygens Metasurfaces". In a reflective metasurface, the surface re-radiates the wave towards the intended user when both the BS and user are on the same side. In contrast, transmissive metasurface is used to transmit a wave through the surface when the BS and user are located on opposite sides, such as in outdoor-to-indoor scenarios [30]. Although the transmissive mode might be important for improving indoor coverage, much of the existing research has primarily focused on reflective RIS [31]. Only recent studies have started to investigate transmissive metasurfaces and their potential to enhance indoor coverage [32–34]. In both reflective and transmissive metasurfaces, thanks to their meta-atom arrangement on the surface, they can manipulate the phase-profile and, to some extent, the amplitude-profile of the reflected or transmitted wavefront to generate a different wavefront compared to what would be obtained from an ordinary surface. By designing these surfaces to manipulate phase, amplitude, and polarization, metasurfaces

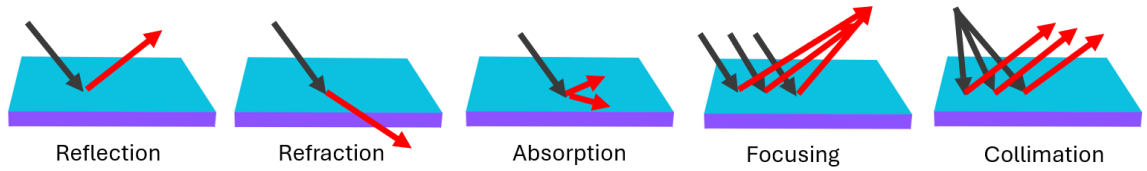

Fig. 1.3 Metasurface functionalities

achieve functionalities that were previously unattainable with natural materials such as anomalous reflection or refraction, total absorption and collimation (see Fig. 1.3). Even more interesting is the ability of a metasurface to function as a lens, which requires applying a curvature to the wavefront, thereby focusing the wave on a specific spot.

But how does a metasurface work? Unlike conventional materials, which rely on gradual phase accumulation through their thickness, metasurfaces achieve wavefront shaping by introducing abrupt phase shifts across their surface. This allows metasurfaces to control wave properties such as phase, amplitude, and polarization with high efficiency and compactness. As known from optics and the Snell's law [35], when a wave impinges on the interface between two different isotropic media (see Fig. 1.4), the angle of incidence and the angle of reflection/refraction are equal. This is known as the Law of Refraction (refer to Eq.1.1)

$$n_1 sin(\theta_i) = n_2 sin(\theta_{r(t)}) \tag{1.1}$$

where n_1 and n_2 are the refractive indices of the two media, θ_i is the angle of incidence, and θ_r or θ_t are the angles of reflection and refraction, respectively. On the contrary, when an electromagnetic wave interacts with a metasurface, its local phase and amplitude are modulated according to the design of the meta-atoms. As a consequence of its microscopic design, a metasurface can "break" Snell's law and modify the phase of the incoming wave in a spatially varying manner, resulting in angles of reflection and refraction that differ from the angle of incidence. This results in an engineered angle of refraction that does not depend solely on the bulk properties of the media but rather on the design of the metasurface itself. This generalized law of refraction [36] is expressed as in Eq. 1.2:

$$n_1 sin(\theta_i) - n_2 sin(\theta_r) = \frac{\lambda}{2\pi}\frac{d\phi}{dx} \tag{1.2}$$

where $\frac{d\phi}{dx}$ is the gradient of the phase shift introduced by the metasurface, which allows the control of the direction of the re-radiated beam, differently from conventional Snell's law. This property opens up new possibilities for designing flat, lightweight components like lenses, gratings, and beam-steering devices.

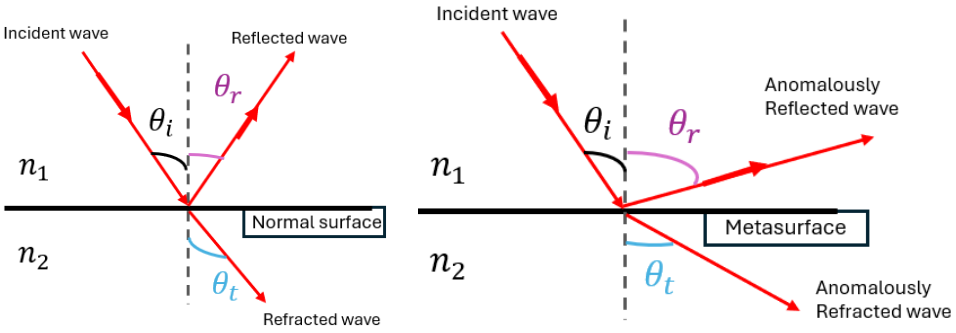

(a) Normal surface (b) Metasurface

Fig. 1.4 Snell's law on normal surface and metasurface

1.4 Reconfigurable surfaces versus Smart Skins

The wireless channel is inherently dynamic, so the ability to reconfigure these metasurfaces in real-time is essential to effectively adapt to changing conditions of the propagation environment. For this reason, metasurfaces are often built using tunable materials necessary for their reconfiguration, such as liquid crystals, phase-changing materials, MEMS, or varactor/PIN diodes [37]. It is worth mentioning that reconfigurable metasurfaces are one of the ways to realize Reconfigurable Intelligent Surfaces (RIS); the other approach is through reconfigurable reflect/transmit arrays. Regardless of whether reconfigurable metasurfaces or reflect/transmit arrays are used, RIS has emerged as a promising solution for real-time environmental customization and propagation channel control. When implemented on a large scale, reconfigurable surfaces are often referred to as Large Intelligent Surfaces (LIS) [18]. RISs/LISs are intended to realize so-called programmable and reconfigurable wireless propagation environments, i.e., wireless environments that are not considered as external, random and uncontrollable entities, but as part of the network components that must be optimized, in order to fulfill the stringent requirements in terms of coverage and channel characteristics of 6G networks [19]. Reconfigurable metasurfaces are dynamic structures capable of adjusting their electromagnetic response in real-time to external stimuli such as voltage. By actively controlling the phase, amplitude, or polarization of incident electromagnetic waves, reconfigurable metasurfaces enable a range of applications, such as adaptive beam steering or real-time holography. Their ability to dynamically change their behavior makes them ideal for systems requiring versatility, such as in smart antenna arrays, radar systems, or wireless communication networks where adaptable beamforming can significantly enhance performance [38] [39]. For instance, reconfigurable metasurfaces allow the same surface to perform multiple tasks dynamically without requiring physical adjustments, making them ideal for versatile systems where the environment is constantly

changing [40]. The key advantage of reconfigurable metasurfaces lies in their tunability and flexibility, providing enhanced performance and functionality at the cost of increased complexity and power requirements. On the other hand, passive smart skins, often referred to as static metasurfaces, are fixed structures designed to manipulate electromagnetic waves passively. These surfaces are designed with pre-determined functionalities and do not require external control to operate. Therefore they must be mounted in strategic locations or on building walls. Also known as "Smart Skins" passive metasurfaces are used in applications where simplicity, low power consumption, and cost-efficiency are critical. Unlike their reconfigurable counterparts, passive smart skins offer excellent performance in fixed applications, providing robustness and reliability without the need for complex control systems. However, their lack of flexibility limits their use to dynamic scenarios. Nonetheless, both technologies provide significant benefits, with reconfigurable metasurfaces offering versatility and smart skins providing simplicity, making them complementary solutions for different use cases. Throughout this thesis, we primarily refer to reconfigurable intelligent surfaces as RIS, regardless of the underlying fabrication technology, whether metasurface-based or reflect/transmit array-based.

1.5 RIS versus active repeaters/base stations

The choice of RIS over active repeaters or network densification with additional base stations (BS) is driven by several key advantages, particularly in terms of energy efficiency, cost-effectiveness, flexibility, and ease of deployment.

1. **Energy Efficiency**: RIS are also referred to as semi-passive devices because they consume minimal energy; they modify the phase of incoming signals without actively amplifying them. In contrast, active repeaters and base stations continuously consume power to amplify and re-transmit signals, making RIS a more energy-efficient solution, especially in large-scale deployments [41] [42]. In general, RIS offers a significant reduction in energy consumption with respect to repeaters/BS by eliminating the need for energy-intensive signal processing.

2. **Cost-Effectiveness**: RIS are more cost-effective to produce and deploy compared to the infrastructure and costs associated with additional BSs or repeaters. The deployment of BSs requires significant investment in site acquisition, energy supply, and maintenance [43]. Meanwhile, RIS can be seamlessly integrated into existing structures, such as building facades, walls, and ceilings, providing a low-cost alternative

for extending network coverage without the complexity and high costs of traditional infrastructure expansion [44].

3. **Low Electromagnetic Interference (EMI)**: RIS can help to minimize electromagnetic interference (EMI) since they simply re-radiate existing waves rather than generating new ones. Network densification with additional Bss and repeaters increases interference due to the overlapping signal transmission, requiring more sophisticated interference management techniques [45]. RIS, being semi-passive, avoids this issue and improves the overall quality of signal transmission in dense urban environments.

4. **Seamless Integration with Construction:** RIS can be directly integrated into building materials such as walls, windows, and other surfaces, aligning with modern construction trends toward smart buildings and cities. This seamless integration enables the technology to enhance communication without the need for aesthetically disruptive or space-consuming hardware [44] [31]. On the contrary, base stations and active repeaters require visible infrastructure, which can conflict with urban design aesthetics, particularly in dense environments.

1.6 RIS Modeling

From a technological standpoint, the most common type of RIS is the so-called Phase Gradient Metasurface (PGM) which is designed to apply a constant phase-gradient to the re-radiated wave by means of a periodic arrangement of its elements along a given direction on the surface, therefore realizing an anomalous reflection or transmission along the same direction (Fig.1.5). PGMs are also referred to as local metasurfaces because their effect on the re-radiated wave, as well as the power balance between the incident, dissipated and re-radiated power fluxes at the surface can be considered local. Unfortunately, PGM metasurfaces being periodic, do not reradiate only one single wave in the desired direction, but also a spectrum of parasitic waves corresponding to the propagating Floquet's modes [46]. Parasitic modes are function of the incident direction and can be suppressed at the expense of power efficiency [36]. Other metasurface technologies are available nowadays that exploit surface-wave propagation within the metasurface substrate to realize non-local designs that can suppress parasitic modes without sacrificing power-efficiency and realize quasi-perfect anomalous reflectors. Their ideal behavior however, only takes place for a single illumination direction of design [36]. Moreover, real-world metasurfaces have a finite size that generates edge diffraction, while illumination conditions are usually far from

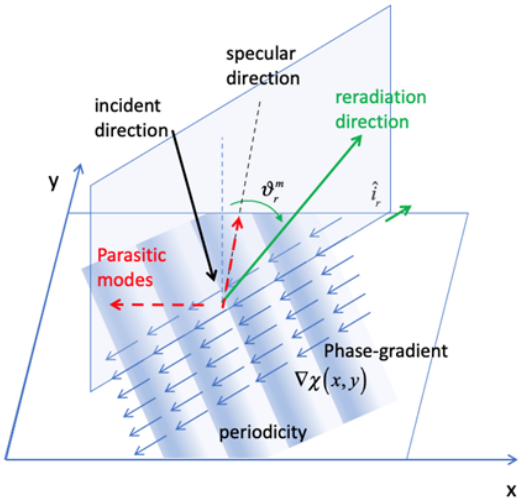

Fig. 1.5 Phase-gradient, periodic metasurface

being far-field, plane wave illumination with a single incident direction. Following the considerations above it is evident that:

1. Electromagnetic propagation in presence of a metasurface is a complex process that involves microscopic propagation phenomena (coupling between meta-atoms, surface waves, etc.) within the metasurface structure.

2. Metasurfaces are far from showing an ideal behavior, i.e. they show dissipation, scattering and multiple re-radiation modes, although usually only one of them is the desired one.

While the aforementioned propagation phenomena are essential for small-scale applications of metasurfaces, such as in antennas and devices, only the overall, macroscopic behavior—particularly in terms of scattering in the radiative near-field and far-field—is relevant for the simulation and design of large intelligent surfaces within wireless networks. Full-wave electromagnetic methods, which are necessary for accurately simulating microscopic propagation phenomena, are impractical for this purpose due to their complexity and computational demands. Instead, simpler and more efficient models are preferred for the large-scale design of intelligent surfaces in wireless systems. At the same time, the analysis of the actual behavior of a RIS within a wireless network and its impact in terms of coverage or spectral efficiency requires electromagnetically consistent, realistic models for RIS scattering which take into account the non ideal phenomena, the RIS's main parameters, the wave transformations it applies, its size, its losses, illumination conditions and re-radiation distance [19]. Motivated by these considerations, a few research investigations have recently addressed

macroscopic scattering from finite-size metasurfaces based on different methods and modeling assumptions [47] [48] [49]. In [47] it is explicitly accounted for the existence of multiple directions of propagation based on Floquet's theory. This theory is, however, rigorously applicable only to periodic (e.g., phase-gradient) metasurfaces. Also, the main analysis is specialized to the far field of the RIS. In [48] authors develop a ray-based representation of scattering from a finite-size RIS under the assumption that the RIS can be represented as locally periodic. The model proposed in [49], although less rigorous, is more general and also accounts for the presence and impact of diffuse scattering that may be caused by, e.g., design trade-offs, construction inaccuracies and dust or raindrops deposit. In this thesis (Chapter 2 and 3) we describe two approaches for general purpose, macroscopic modeling of scattering from a wide variety of RIS configurations for use in link-level and system-level wireless system simulators. The first one is a simplified bilateral (in reflection and transmission) Huygens-based modeling approach [50] that relies on a parametric power balance and on an "antenna-Array-Like" (see C for more details) description of the metasurface [49]. The approach is based on a very simple theory but is limited to single-bounce scattering. The second approach [51] is a more rigorous, albeit more complex, ray-based representation of scattering from the metasurface that can be easily embedded into ray launching propagation simulation tools and therefore can simulate multiple-bounce cases.

Chapter 2

A macroscopic bilateral modeling approach for reflective and transmissive RIS

Index Terms *reconfigurable intelligent surfaces, macrocopic modeling*

2.1 Introduction

In the recent years, there has been a growing interest in RIS technology which enables the manipulation of the reradiated - anomalously reflected or transmitted - radio wave characteristics. Such capabilities give engineers degrees of freedom to tailor the propagation environment [18, 19]. RIS can be implemented by the means of metasurface technology, using electrically-small printed scattering elements on a dielectric substrate or as reflect-arrays and transmit-arrays made with proper antenna elements [21]. The reconfigurability of RIS can be ensured using active elements such as varactors or p-i-n diodes in each unit cell. While the majority of the existing contributions in the literature focus on the ability of RIS to manipulate the reflected wave only, there is a growing interest in exploring other functions of RIS for wireless system application. Transmissive RIS that can manipulate the transmitted wave may play a crucial role, for example in ensuring coverage when the radio link ends are situated on opposite sides of a wall [52]. A potential application of transmissive RIS involves coating windows to improve radio signal transmission for indoor coverage while maintaining light transparency, as demonstrated in [53]. Moreover, to fully exploit their full potential, RIS may need to simultaneously manipulate both the reflected and transmitted wave [54]. The design of the RIS depends on the operating wavelength, the

substrate material, the incidence angle and wave polarization: depending on those parameters and on the chosen technology, RIS can exhibit different power-efficiencies [55, 54, 53]. Other limitations and non-idealities include the finite size of a RIS, scattering generated by realization imperfections and phase discretization, parasitic modes, and restricted angles of operation. Most RISs are limited to phase modulation only. However, amplitude modulation and/or non-local effects can be used to improve performance and efficiency [56].
In order to account for those characteristics while keeping complexity and computation time low enough to allow multi-RIS, system-level simulation, simple and yet realistic macroscopic models for RISs are necessary. Recently, parametric models have been proposed in the literature that take into account the physical structure of RIS, aiming at including all the non-idealities. In [49] a first parametric Huygens-based model was introduced, based on a power balance at the RIS surface. The power balance is based on the power conservation principle between the incident and reradiated waves according to a few macroscopic parameters that depend on the type of RIS and its technology. To account for the phase and amplitude modulation realized by the RIS, a so called spatial modulation coefficient was introduced. Furthermore, a ray-based reradiation model was developed in [51]. However, the mentioned models are conceived to model reflective RISs only.
In the present chapter, we extend the foregoing power-balance approach [49] to the bilateral case, therefore including also the application to transmissive and bilateral RIS, and we carry out a realistic model parametrization with respect to the existing RIS prototypes presented in the literature. Furthermore, we provide a few model application examples.

2.2 Power Balance: Bilateral extension

Here, we extend the model proposed in [49] by considering a general-purpose RIS that can reradiate the incident wave into both half-spaces. Merging the approaches proposed in [49] and [57], we reorganize and extend the model also to transmission, i.e. to the forward half space. The foundation of the model is a power balance defined for the local surface element: while it is local, to take into account non-uniform RIS realizations and non-plane wave illumination, that imply different incidence angles and different behavior at different positions, non-local effects at the wavelength scale can be taken into account through the amplitude factor of the spatial modulation coefficient that is applied at a later stage. Thus, the power balance in [49] at the generic surface element dS takes the following form:

$$P_i = P_R + P_S + P_m + P_d + P_T \tag{2.1}$$

where P_R is the specularly reflected power, P_S is the total diffuse scattered power (due to mechanical or electrical inaccuracies), P_m is the total reradiated power in the anomalous directions, P_d is the power dissipated due to material losses and P_T is the transmitted power through the RIS in the "forward" direction, i.e. the same as incidence direction, but in the transmission half-space.

Since the model needs to consider a general case of a RIS that is designed to both anomalously transmit and reflect the incident wave, we express total diffuse scattered power as:

$$P_S = P_{S_R} + P_{S_T} \tag{2.2}$$

where P_{S_R} and P_{S_T} are the diffuse scattered powers in reflection and transmission respectively. The same holds for

$$P_m = P_{m_R} + P_{m_T} \tag{2.3}$$

where P_{m_R} and P_{m_T} are the anomalously reradiated powers in the backward (reflection) and forward (transmission) half-space, respectively. To characterize the power balance at the generic RIS surface element, we introduce the reradiation coefficients m_R and m_T that determine the fraction of incident power that is reflected and transmitted into anomalous modes. It is worth mentioning that in the case of periodic or locally periodic structures, the coefficients m_R and m_T can represent the power amplitude of Floquet modes, although only one mode is considered up to here. The symbol τ indicates the power transmission coefficient (or transmittance) that accounts for attenuation that transmitted wave undergoes when propagating through the RIS in the forward direction. Similarly, ρ is the power reflection coefficient (or reflectance) that accounts for reradiation in the specular direction. Under these assumptions and similarly to Eq. (2.2) in [49], the power balance in (2.1) can be rewritten as follows, by expressing all its terms as a function of the incident power P_i

$$P_i = R_R^2 \rho P_i + S_R^2 (m_R + \rho) P_i + R_R^2 m_R P_i + R_T^2 \tau P_i + S_T^2 (m_T + \tau) P_i + R_T^2 m_T P_i + \alpha P_i \tag{2.4}$$

In (2.4), dissipated power P_d is also expressed as a function of incident power by using the dissipation parameter α, which accounts for the percentage of the dissipated power. In the above equation we see that a reduction factor R^2 is applied to both specular, forward, and anomalous reradiation modes. Moreover, differently from the definition of S^2 in [49], the diffuse scattering coefficient $S^2_{R(T)}$ is redefined in this work as the ratio between total diffused power in the reflection (transmission) half-space and total reradiated power in the reflection

(transmission) half-space, therefore as:

$$S_R^2 = \frac{P_{S_R}}{P_R + Pm_R} \qquad \text{and} \qquad S_T^2 = \frac{P_{S_T}}{P_T + Pm_T}. \tag{2.5}$$

For both the diffuse scattering coefficient S and the reduction factor R, subscripts "R" and "T" are used to distinguish between the reflection (backward) and the transmission (forward) half-space, respectively. If we assume a perfectly smooth RIS and without physical or electrical imperfections, there would be no scattered power ($S_R = S_T = 0$) and the reduction factors R_R and R_T would become equal to 1: then in this case (2.4) would reduce to:

$$1 = \rho + m_R + \tau + m_T + \alpha \tag{2.6}$$

Here, ρ, m_R, τ, m_T and α are parameters that range from 0 to 1. Furthermore, as previously discussed in [49], this set of parameters may depend on the angle of incidence of the illuminating wave, which changes along the RIS surface for near-field illumination. Therefore, the power balance in (2.4) and (2.6) holds only locally. However, for far-field illumination and for a uniform RIS (on the wavelength scale) this power balance can be applied globally to the whole RIS. Combining (2.4) and (2.6), and assuming that scattering-inducing irregularities don't alter the power balance between the two half-spaces, which means for instance that diffuse scattering in the backward half-space only detracts power from reradiation toward the same half-space, the following relations between S and R are obtained:

$$S_R^2 + R_R^2 = 1, \tag{2.7}$$

$$S_T^2 + R_T^2 = 1. \tag{2.8}$$

Equation (2.7) shows that the higher the diffuse-reflection power , the lower the power reradiated in the backward half-space. The same holds true independently for the forward half-space as per (2.8). As known from electromagnetic theory, in non ideal conditions, RIS can generate multiple parasitic reradiation modes (e.g. Floquet's modes of periodic structures). Let us assume that in general RIS anomalously reflects N propagation modes and anomalously transmits K propagating modes. In order to account for multiple propagation modes, we denote with m_{R_n} the reflected power coefficient of the n^{th} propagation mode and with m_{T_k} the retransmitted power coefficient of the k^{th} propagation mode. Then eq. (2.4) can

be extended to the case of multiple reradiation modes as:

$$1 = R_R^2\rho + S_R^2(\sum_{n=1}^{N} m_{R_n} + \rho) + R_R^2 \sum_{n=1}^{N} m_{R_n} + R_T^2\tau + S_T^2(\sum_{k=1}^{K} m_{T_k} + \tau) + R_T^2 \sum_{k=1}^{K} m_{T_k} + \alpha \quad (2.9)$$

where $\sum_{n=1}^{N} m_{R_n}$ and $\sum_{k=1}^{K} m_{T_k}$ represent total (anomalous) power reradiation in the backward and forward half-space, respectively. The summations above do not include the indices $n = 0$ and $k = 0$ that usually refer to the specular and forward propagating modes, already taken into account through the coefficients ρ and τ. The power balance described in this section ensures that each reradiation mechanism is properly taken into account in the perspective of a macroscopic but physically-sound modeling of a RIS. It is worth noting that macroscopic parameters described above can be defined by measurements on prototypes or computed using electromagnetic simulation.

As a last step, the reradiation parameters m_{R_n} and m_{T_k} that satisfy power balance (2.9) and the proper spatial modulation functions for each reradiation mode are used to compute the reradiated field through the AAL Huygens-based approach, described in previous work that corresponds to modeling the metasurface as a two-dimensional antenna-array: the metasurface is discretized into surface elements, then each element is modeled as an aperture antenna that receives the incident power P_i and reradiates a spherical wavelet of power P_m according to a Huygens source radiation pattern while satisfying basic electromagnetic consistency requirements [49]. All the wavelets generated by all surface elements add up coherently to generate the overall reradiated wavefront. The field contribution of the generic element of the RIS with coordinates (x,y) at the observation point P is:

$$\Delta E_m(P|x,y) \;=\; \sqrt{\frac{m\,60\,P_t\,G_t}{r_i\,r_m}}\,A(x,y)\;e^{j\chi_m(x,y)}\;\frac{3\,\lambda}{16\,\pi}(1+\cos\theta_i)\,(1+\cos\theta_m)\;e^{-jk(r_i+r_m)} \quad (2.10)$$

where $A(x,y)$ and $e^{j\chi_m(x,y)}$ are the amplitude and the phase profile that RIS imposes on the reradiated field, r_i and r_m are the distance from the Tx to the RIS element and from the RIS element to the Rx, respectively, θ_i is the incidence angle and θ_m is the reradiation angle toward the observation point P, whereas P_t and G_t are the transmit power and antenna gain. The overall reradiated field is obtained through summation of the reradiated field by each RIS element. More details can be found in [49].

2.3 Simulation results

In this section some simulation results, obtained by applying macroscopic parameters of RIS prototypes found in the literature in the previous section, are presented. We consider two benchmark scenarios: one involving a transmissive RIS conceived for anomalous reradiation in the forward half-space which also reradiated a parasitic specular reflection in the backward half-space, and a focalizing RIS (meta-lens) that concentrates the incident power into a focus in the forward half-space. For the first case study, a non ideal, 5 x 5 m RIS placed in the xy plane and illuminated with an incidence angle of 20° by a plane wave linearly polarized along the y axis is considered. The operation frequency is 26.5 GHz, the incident field intensity is 1 V/m and the desired reradiation angle is 60°, which is implemented using a constant phase-gradient spatial modulation profile as shown in [49]. In this case, m_T=0.746, α=0.104 ρ=0.15 (values are taken from prototypes in [52] [55]) . As depicted in Fig. 2.1, a portion of the incident power is steered toward the desired reradiation angle while another portion goes toward specular reflection. Additionally, a part of incident power is dissipated in the substrate. This simulation result highlights the potential of the model to reproduce a realistic RIS behavior. For the second case study, we consider a double-focalizing, bilateral lens

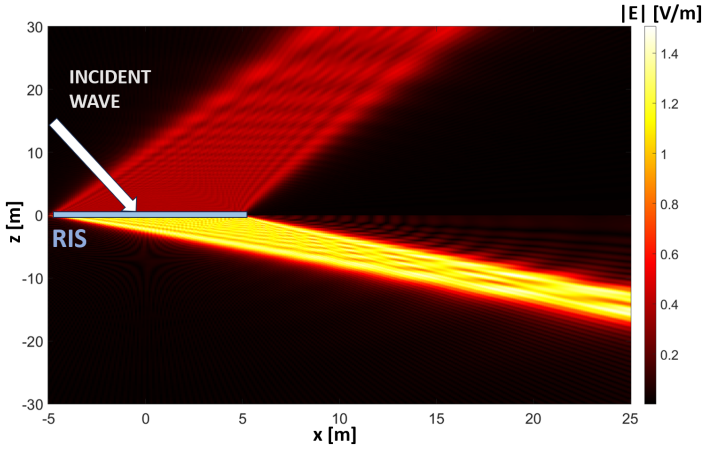

Fig. 2.1 Non ideal transmissive case with m_T=0.746, α=0.103 [50]

that is able to focus a normally incident wave with 1 V/m intensity in two spots located in both the backward and the forward half-spaces, although here we only show the latter. RIS dimensions remain the same as in the previously discussed case except from the operating frequency that is 14 GHz, while parameters are m_T=0.246, m_R=0.2785, α=0.4755 and the desired focus point at (0; 0; -3m) as in [54]. Focusing is implemented using a focalizing, circular symmetry spatial modulation profile as shown in [49], section IV.2. It is worth noting that the electric field intensity at the focus point is 9 times higher than the incident field intensity as shown in Fig. 2.2, where the field on a xz plane orthogonal to the RIS

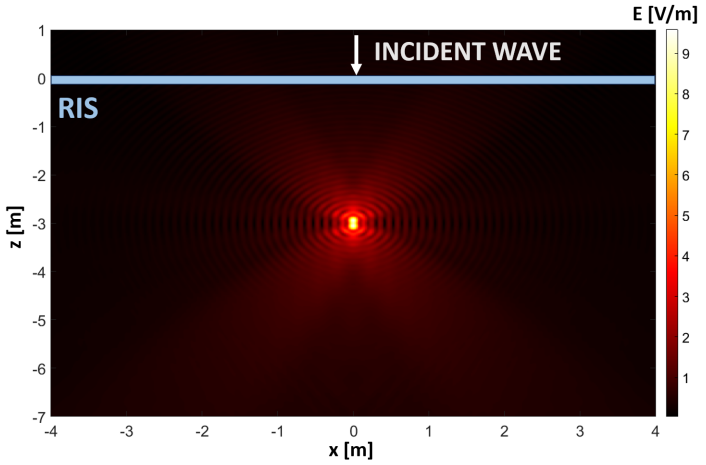

Fig. 2.2 Non ideal forward focus with m_T=0.246, α=0.4755 [50]

passing through the focus is shown. The size of the focal area is similar to the wavelength, in accordance with lens theory.

2.4 Conclusion

In this chapter, we have presented a macroscopic bilateral modeling approach for RIS, extending previous work to incorporate both reflective and transmissive functionalities. By applying a power balance at each RIS element, our extended model accurately predicts RIS behavior. We have demonstrated the effectiveness of our approach through simulation results in two benchmark scenarios: a transmissive RIS and a double-focalizing bilateral RIS. Future work includes refining the model with non-linear effects, alongside experimental validation. Overall, our approach offers a simple yet powerful tool for optimizing RIS-based wireless communication systems, promising advancements in various applications.

Chapter 3

An Efficient Ray-Based Modeling Approach for Scattering from RIS

Index Terms *macroscopic modeling, ray tracing, ray launching, reconfigurable intelligent surface (RIS), metasurface*

3.1 Introduction

Until recently, the design of wireless systems has been based on a probabilistic approach where the propagation channel was considered a largely unknown, random process that engineers had to cope with during the design of transmitter and receiver chains or network architecture. In the last years, RIS technology has been proposed as an opportunity to broaden the design approach, allowing for the first time to engineer the wireless propagation channel. Interesting applications for 6G networks are envisioned to ease coverage limitations at mm-wave and THz frequencies and to perform basic operations on the signal "at the speed of light", limiting therefore the use of active repeaters and digital signal processing, with a reduction in latency and energy consumption [19]. A RIS is an electrically thin slab that can be realized either as a metasurface using electrically small, printed scattering elements, or as a reflect-array or a transmit-array with half-wavelength spaced printed antenna elements. Using control networks employing PIN diodes, varactors or other methods, a RIS can dynamically tailor its local reflection or transmission properties and therefore can manipulate the re-radiated field characteristics and wavefront shape [19, 58]. The scattering behavior of a RIS can be accurately simulated using *microscopic modeling* approaches (e.g. using Electromagnetic simulation or microwave network theory), that are based on a detailed description of the RIS microstructure. Unfortunately, microscopic models are complicated

to use and require considerable computational resources. Therefore, they cannot be used for efficient, large-scale simulation of wireless links or systems employing RIS technology [21, 22].

Thus, path-loss models or channel models for RIS-assisted links have been developed and used for performance evaluations in recent years, see for example [31, 59, 60]. Such models however, being based on a discrete periodic approach that assumes independent scattering elements (unit cells) characterized by a given scattering coefficient and pattern, either overlook or only approximately take into account coupling, parasitic modes and other non-idealities [21].

Several other approaches have been proposed in the literature to try to solve the above-mentioned limitations and to achieve a good trade-off between good electromagnetic consistency and low computational complexity. Some authors propose hybrid approaches where electromagnetic simulation is used to derive a far-field radar cross section of the RIS to be inserted in ray tracing simulation [61]. Such approaches, although efficient, cannot be used to model near-field effects such as focusing, which represents one of the most important RIS applications. Very promising are *macroscopic modeling* approaches that overlook the microscopic structure of the RIS in order to directly address the specific wave transformation it realizes [62, 47, 63, 64, 49]. These approaches assume that the metasurface can be homogenized and described in terms of an effective surface function - e.g. a surface impedance or a surface (or spatial) modulation function - that determines such a wave transformation based on Maxwell's equations. The function can be derived from theory, i.e. from the wave transformation the RIS is intended to realize, or from experiment, i.e. from measurements on the wave transformation that an existing RIS actually realizes.

In particular, in [49], a realistic macroscopic model for evaluating multi-mode re-radiation from generic, finite-size RIS is introduced. The model is based on a hybrid approach combining a Huygens-based method to model anomalously re-radiated modes with well-established ray-based methods to model specular reflection and diffuse scattering that are inevitably present in real-world non-ideal metasurfaces. In particular, diffuse scattering can model the noise-like re-radiation effect of mechanical and electrical non-idealities such as deviation of the RIS from a flat surface, phase-tuning errors or even phase-discretization effects due to the use of a limited number of bits in the control circuit. Specifically, the Huygens-based and the ray-based methods are combined through a parametric power-balance constraint that ensures energy conservation between the incident field, scattered field and dissipation inside the slab. In the present chapter we build on the foregoing macroscopic and parametric approach described in Chapter 2 to develop a ray-based, efficient approach also for anomalous re-radiation, therefore achieving a fully-ray based macroscopic RIS model

that can be easily integrated into efficient RL algorithms for large-scale simulation such as the one proposed in [65]. In particular, we suitably extend GO theory [66] to the case of a reflective RIS illuminated with an astigmatic wavefront. Diffraction is modeled through the UTD [67, 68], and a new formulation of the UTD diffraction coefficients is proposed that can be applied to any re-radiation mode of a RIS and easily implemented in RL tools, following the same approach of [68]. Differently from the study in [48], where a ray-based description of re-radiation from locally-periodic, finite metasurfaces was first proposed, we assume to model re-radiation with a forward ray tracing approach, therefore avoiding the complex and time-consuming *critical point* search step. In the next section of this chapter we describe our approach more in detail: briefly addressing the model's parametric foundation, which is shared with the model described in [49] and Chapter 2, some basic concepts of Geometrical Optics that we have used, and then describe how the ray re-radiated from a generic surface location (*anomalously reflected ray*) or from the surface edge (*anomalously diffracted ray*) are computed in terms of direction and field. The model is then validated in Section 3.3 by comparison with some reference models available in the literature.

Building on the macroscopic bilateral model introduced in Chapter 2, which provides a parametric power balance framework for RIS characterization, this chapter explores an alternative yet complementary approach: a ray-based modeling technique. While the previous model simplifies the re-radiation process through macroscopic coefficients, the ray-based approach explicitly accounts for the geometrical and wave-based interactions at a finer granularity. By leveraging GO principles, this model offers improved accuracy in simulating real-world RIS deployments, particularly for large-scale wireless environments.

3.2 The proposed approach

We propose a macroscopic, ray-based approach that uses the *spatial modulation function* introduced in [49, 21], to model RIS re-radiation. In the following, we make use of GO concepts such as ray, locally plane wave, local wavefront curvature, spreading factor etc. [66]. In [48, 64], an image-ray tracing approach for locally periodic metasurfaces is proposed, where "critical points" are identified using an iterative procedure, in order to trace reflected or transmitted rays for specific transmitter and receiver positions. In the present work, we propose a discrete RL approach where the RIS is discretized into surface elements, rays are launched toward each one of them, reflected/diffracted according to the spatial modulation function at the considered position, and re-launched in space without any need for a critical-point search phase. Therefore, the method can be inserted into a discrete, parallelized RL algorithm as the one presented in [65] for efficient field-prediction over an area or volume:

in this case the sub-set of RIS-re-radiated rays hitting the desired target area or volume will have to be determined and their field can be mapped onto the target domain using some efficient computer graphics method. Surface discretization resolution, i.e. the size of each surface element (or "tile"), determines the spacing of the rays and therefore the resolution of the computed field, similarly to what shown in [69], Fig. 4, for the traditional discrete ray launching model therein described, and should be therefore chosen according to a trade-off between accuracy and computation speed. However, discrete RL computation time can be drastically reduced using parallelization techniques [65, 69]. In this work, we leverage the macroscopic approach presented in [49], Section 3.2, but we propose a more efficient, fully ray-based re-radiated-field computation method in place of the Huygens-based methods there described. The basic assumptions, as in [49], are the following:

1. the homogenized surface properties vary slowly at the wavelength scale (slowly modulated RIS)

2. because of 1), we use the concept of *Spatial Modulation Coefficient* often called also "reflection coefficient"

3. the re-radiated field can be described as a discrete set of re-radiation modes (e.g. Floquet's modes of a locally periodic metasurface)

4. we address the computation of radiative near field and far field, but we neglect for the time being the effect of evanescent modes (i.e. surface waves) and vertex diffraction.

On the base of the foregoing assumptions, we describe each reradiating mode field as a set of rays reflected or diffracted at each surface element. In the rest of this section, after recalling basic GO concepts, the computation of:

(i) re-radiation angle

(ii) Field

(iii) Spreading factor

is described for a reflected or edge-diffracted ray of a single re-radiation mode. For a complete field computation, the procedure will have to be iterated for all the propagating modes. For the sake of brevity, only reflecting RISs are considered: although extension to *transmissive* RISs, that reradiate mainly in the forward half-space, is quite straightforward, it will be addressed in future work.

3.2.1 Relevant Geometrical Optics background

According to GO theory, a propagating wave in free space can be described in terms of rays, i.e. lines that are everywhere orthogonal to the wavefront and therefore represent wave *paths*. In the high-frequency regime, the Electromagnetic field of a propagating wave can be approximated as [66]:

$$\begin{aligned} \mathbf{E}(\mathbf{r}) &\simeq \mathbf{E}_0(\mathbf{r})\, e^{-jk_0\,\psi(\mathbf{r})} \\ \mathbf{H}(\mathbf{r}) &\simeq \mathbf{H}_0(\mathbf{r})\, e^{-jk_0\,\psi(\mathbf{r})} \end{aligned} \tag{3.1}$$

where $\mathbf{r}$ is the position vector of the generic observation point P, $k_0 = 2\pi c_0/f$ is the free space wavenumber, $\mathbf{E}_0(\mathbf{r})$, $\mathbf{H}_0(\mathbf{r})$ are slowly varying complex vectors, representing the local amplitude and polarization of the wave, and $\psi(\mathbf{r})$, also called eikonal function, is an optical-length function that depends on the actual shape of the wavefront. In particular, the gradient of the eikonal function $\nabla\psi$, is normal to the wavefront and then defines the local ray direction, while the Hessian matrix of ψ, indicated as $\nabla\nabla\psi$, takes into account the local curvature of the wavefront. The Hessian matrix of the eikonal function is often indicated with the symbol $\underline{\mathbf{Q}}$ and called the *curvature matrix* of the local wavefront [70, 71]. By substituting (3.1) in Maxwell's equations, the following relations are obtained (*locally plane* TEM wave) [66]:

$$\nabla\psi\cdot\mathbf{E} = 0 \qquad \nabla\psi\cdot\mathbf{H} = 0 \qquad \eta\mathbf{H} = \nabla\psi\times\mathbf{E} \tag{3.2}$$

where $\eta = \sqrt{\mu_0/\varepsilon_0}$ is the free-space impedance, and the symbols $''\cdot''$ and $''\times''$ stand for the dot scalar product and the cross vector product, respectively. Moreover, it can be proved that in a homogeneous medium, the ray trajectories are rectilinear. In particular, in free space the generic ray has constant direction $\hat{\mathbf{s}} = \nabla\psi$, whereas the wavefront has an astigmatic shape so that the E-field propagating along a single ray can be written as [70]:

$$\mathbf{E}(s) = \mathbf{E}(0)\,A(s)\,e^{-jk_0 s} = \mathbf{E}(0)\sqrt{\frac{\mathrm{pdet}\{\underline{\mathbf{Q}}(s)\}}{\mathrm{pdet}\{\underline{\mathbf{Q}}(0)\}}}\,e^{-jk_0 s} \tag{3.3}$$

where s is the local coordinate along the ray, i.e. the distance between the current point and the reference point $s = 0$, $\mathbf{E}(0)$ is the field at the reference point, and $A(s) = \sqrt{\mathrm{pdet}\{\underline{\mathbf{Q}}(s)\}/\mathrm{pdet}\{\underline{\mathbf{Q}}(0)\}}$ is the so-called *spreading (or divergence) factor*, that derives from power conservation on a ray tube and depends on the actual wavefront's shape. In (3.3), the notation $\mathrm{pdet}\{-\}$ stands for the *pseudo-determinant* of the square matrix, i.e. the product of its non-zero eigenvalues.

The curvature matrix of an astigmatic wave can be expressed in the following way [70, 68]:

$$\underline{\mathbf{Q}}(s) = \frac{1}{\rho_1 + s}\hat{\mathbf{X}}_1\hat{\mathbf{X}}_1 + \frac{1}{\rho_2 + s}\hat{\mathbf{X}}_2\hat{\mathbf{X}}_2 \tag{3.4}$$

with ρ_1 and ρ_2 being the principal curvature radii at the reference point, corresponding to the two principal curvature directions $\hat{\mathbf{X}}_1, \hat{\mathbf{X}}_2$. In (3.4) and in the following, the dyadic product is used for ease of notation, which is equivalent in linear algebra to the multiplication of a column vector by a row vector, i.e.

$$\mathbf{ab} \equiv \mathbf{a}\mathbf{b}^T$$

where the superscript $()^T$ stands for the transpose operator.

According to (3.4), in free space the wavefront diverges as it propagates without changing shape, i.e., the two principal directions remain the same while the curvature radii linearly increase with s as $\rho_1 + s$ and $\rho_2 + s$.

By definition (3.4), $\underline{\mathbf{Q}}(s)$ is a rank-2 symmetric matrix, and the wave principal curvatures $\kappa_1 = (\rho_1 + s)^{-1}$, $\kappa_2 = (\rho_2 + s)^{-2}$ are its non-zero eigenvalues, while the principal directions $\hat{\mathbf{X}}_1, \hat{\mathbf{X}}_2$ are the corresponding eigenvectors. This means that, by adopting the local ray-fixed reference system $(\hat{\mathbf{X}}_1, \hat{\mathbf{X}}_2, \hat{\mathbf{s}})$, $\underline{\mathbf{Q}}(s)$ is diagonalized in the form:

$$\underline{\mathbf{Q}}(s) = \begin{bmatrix} \frac{1}{\rho_1 + s} & 0 & 0 \\ 0 & \frac{1}{\rho_2 + s} & 0 \\ 0 & 0 & 0 \end{bmatrix} \tag{3.5}$$

As a consequence of (3.4), (3.5) the following property holds, as the principal directions $\hat{\mathbf{X}}_1, \hat{\mathbf{X}}_2$ lay on the transverse plane with respect to the ray direction $\hat{\mathbf{s}}$:

$$\underline{\mathbf{Q}}\,\hat{\mathbf{s}} = \hat{\mathbf{s}}^T\underline{\mathbf{Q}} = \mathbf{0} \tag{3.6}$$

Finally, according to (3.3) and (3.5), the spreading factor for an astigmatic wave can be expressed as a function of the principal curvature radii in the form:

$$A(s) = \sqrt{\frac{\rho_1\rho_2}{(\rho_1 + s)(\rho_2 + s)}} \tag{3.7}$$

As it can be seen from (3.7), the GO field has singularities on the wave *caustics*, i.e. for those points along rays so that $s = -\rho_1$ or $s = -\rho_2$. GO theory cannot be applied to compute the field in the vicinity of a caustic: in such a case, different methods based on asymptotic evaluation need to be applied [72].

In the following, according to the GO approach, we leverage the locally plane wave assumption to model reflection and diffraction at each surface element of a RIS, while we

account for the wavefront's actual shape through the spreading factor, that gives the actual attenuation-trend of field's intensity with distance. In practice, we linearize both the incident wavefront - with a local plane - and the effect of the RIS on it – with the local phase gradient – in order to simplify computation steps (i) and (ii) above, whereas the actual curvatures of the wavefront are considered for step (iii).

3.2.2 Anomalous ray reflection

Anomalous ray reflection is modeled according to a 3D version of the *generalized law of reflection* [36], which takes into account that, in general, incidence plane and reflection plane can be different. For the sake of simplicity, we limit the analysis to flat surfaces, but the extension to the case of a curved RIS is possible.

Let us then consider a flat RIS of normal $\hat{\mathbf{n}}$, and let be $\mathbf{r}'$ the position of the generic surface element. The position vector can be expressed as a function of 2 local coordinates on the RIS plane (see Fig. 3.1), i.e. $\mathbf{r}' = \mathbf{r}'(u,v)$. When a ray impinges on the surface with propagation direction $\hat{\mathbf{s}}^i$ so that $-\hat{\mathbf{s}}^i \cdot \hat{\mathbf{n}} = \cos\theta_i$, where θ_i is the incidence angle, the field acquires an *incidence phase gradient* on the surface due to the inclination of the locally-plane wavefront of the ray with respect to the RIS. This phase gradient is:

$$\nabla\chi^i = -k_0 \sin\theta_i \, \hat{\mathbf{s}}^i_\tau \tag{3.8}$$

where the unit vector $\hat{\mathbf{s}}^i_\tau$ defines the orientation of the incidence plane with respect to the RIS surface (see Fig. 3.1).

Eq. (3.8) can be rewritten in the equivalent form:

$$\underline{\mathbf{P}}_\tau \hat{\mathbf{s}}^i = \hat{\mathbf{s}}^i - \hat{\mathbf{n}}(\hat{\mathbf{n}} \cdot \hat{\mathbf{s}}^i) = \sin\theta_i \, \hat{\mathbf{s}}^i_\tau = -\frac{\nabla\chi^i}{k_0} \tag{3.9}$$

where $\underline{\mathbf{P}}_\tau$ is the tangent projection operator, defined as:

$$\underline{\mathbf{P}}_\tau = \underline{\mathbf{1}} - \hat{\mathbf{n}}\hat{\mathbf{n}} \tag{3.10}$$

and $\underline{\mathbf{1}}$ is the identity matrix.

Then, according to a macroscopic approach, the RIS applies the additional phase gradient $\nabla\chi^m$ of the considered re-radiation mode so that the *total phase gradient* at the considered surface location becomes:

$$\nabla\chi = \nabla\chi^i + \nabla\chi^m \tag{3.11}$$

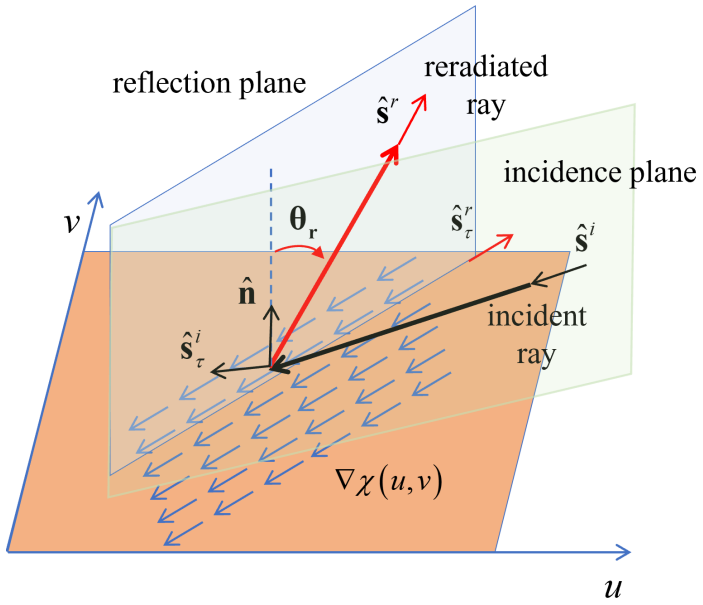

Fig. 3.1 Total phase gradient and anomalous ray reflection at the generic surface element [51]

Anomalous reflection direction takes place according to that total phase gradient. The reflection plane is parallel to the phase gradient direction (see Fig. 3.1); however, as surface points with a greater phase will reradiate before those with a phase lag, the resulting locally-plane wavefront will have opposite orientation with respect to the total phase gradient $\nabla\chi$. It can be easily shown (see Appendix A) that the projection of the reflected ray direction on RIS plane is given by:

$$\underline{\mathbf{P}}_\tau \hat{\mathbf{s}}^r = \sin\theta_r \hat{\mathbf{s}}^r_\tau = \underline{\mathbf{P}}_\tau \hat{\mathbf{s}}^i - \frac{\nabla\chi^m}{k_0} = -\frac{\nabla\chi}{k_0} \tag{3.12}$$

where θ_r is the re-radiation angle, and $\hat{\mathbf{s}}^r_\tau$ defines the reflection (or re-radiation) plane, that generally for a RIS is different from the incidence plane, as shown in Fig. 3.1.

Observing that $|\hat{\mathbf{s}}^r| = 1$, the reflection unit vector can be written using a single compact equation:

$$\begin{aligned}\hat{\mathbf{s}}^r =& \underline{\mathbf{P}}_\tau \hat{\mathbf{s}}^i - \frac{\nabla\chi^m(\mathbf{r}')}{k_0} + \sqrt{1 - \left|\underline{\mathbf{P}}_\tau \hat{\mathbf{s}}^i - \frac{\nabla\chi^m(\mathbf{r}')}{k_0}\right|^2}\ \hat{\mathbf{n}} = \\ =& -\frac{\nabla\chi(\mathbf{r}')}{k_0} + \sqrt{1 - \left|\frac{\nabla\chi(\mathbf{r}')}{k_0}\right|^2}\ \hat{\mathbf{n}}\end{aligned} \tag{3.13}$$

which expresses the *generalized law of reflection*. As in [49, 21], the re-radiated field can be computed using the SMC, that takes into account the overall re-radiation properties of the RIS. According to this macroscopic approach, we assume that the following boundary

condition holds for every point of the RIS surface:

$$\mathbf{E}^r\left(\mathbf{r}'\right) = \underline{\boldsymbol{\Gamma}}\left(\mathbf{r}'\right)\mathbf{E}^i\left(\mathbf{r}'\right) \tag{3.14}$$

In (3.14), instead of a scalar coefficient we make use of the *Spatial Modulation Dyadic* coefficient $\underline{\boldsymbol{\Gamma}}$, in order to take into account the polarimetric effect of the RIS. Such coefficient is defined as:

$$\begin{aligned}\underline{\boldsymbol{\Gamma}}\left(\mathbf{r}'\right) &= \underline{\boldsymbol{\Gamma}}_0\left(\mathbf{r}'\right)\mathrm{e}^{j\chi^m(\mathbf{r}')} = A^m\left(\mathbf{r}'\right)\mathrm{e}^{j\chi^m(\mathbf{r}')}\cdot\underline{\mathbf{R}}^m = \\ &= A^m\left(\mathbf{r}'\right)\mathrm{e}^{j\chi^m(\mathbf{r}')}\cdot\left(R_{\parallel}^m\,\hat{\mathbf{e}}_{\parallel}^i\hat{\mathbf{e}}_{\parallel}^r + R_{\perp}^m\,\hat{\mathbf{e}}_{\perp}^i\hat{\mathbf{e}}_{\perp}^r\right)\end{aligned} \tag{3.15}$$

where A^m and χ^m are the amplitude and phase modulation of the considered re-radiation mode, while the matrix $\underline{\mathbf{R}}^m = R_{\parallel}^m\,\hat{\mathbf{e}}_{\parallel}^i\hat{\mathbf{e}}_{\parallel}^r + R_{\perp}^m\,\hat{\mathbf{e}}_{\perp}^i\hat{\mathbf{e}}_{\perp}^r$ is used to account for the polarization transformation realized by the RIS [73, 68]. The unit vectors $\hat{\mathbf{e}}_{\perp}^{i,r}$ and $\hat{\mathbf{e}}_{\parallel}^{i,r}$ are used to decompose the incident/reflected field into perpendicular (TE) and parallel (TM) components with respect to the incidence/reflection plane on a ray-fixed reference system (see Fig. 3.1), and are easily computed as:

$$\hat{\mathbf{e}}_{\perp}^{i,r} = \hat{\mathbf{s}}_{\tau}^{i,r}\times\hat{\mathbf{n}} \qquad \hat{\mathbf{e}}_{\parallel}^{i,r} = \hat{\mathbf{e}}_{\perp}^{i,r}\times\hat{\mathbf{s}}^{i,r} \tag{3.16}$$

Usually, the phase modulation coefficient χ^m varies on the wavelength scale, while the amplitude modulation coefficient A^m varies on a larger scale and may take into account non-local effects along the RIS surface. In general, A^m and χ^m cannot be arbitrarily chosen, but must satisfy proper constraints in order to be representative of a realistic RIS design, as discussed in detail in [21]. A RIS able to control the polarization, here modeled through the dyadic $\underline{\mathbf{R}}^m$, can be alternatively represented as a tensor impedance sheet (see for example [74, pp. 57-59]). Additional terms may be introduced in (3.15) to take into account additional losses caused by parasitic effects and diffuse scattering, as discussed in [49]. In the following, we assume that the SMD coefficient $\underline{\boldsymbol{\Gamma}}$ is known, either from the design stage, or estimated through measurements.

After defining the local reflection direction $\hat{\mathbf{s}}^r$ and applying the SMD coefficient to the incident field, the last step consists in the computation of the field along the reflected ray, including the spreading factor. This can be derived through the curvature matrix by applying a local phase matching procedure on the RIS surface, following a method similar to the one presented in [70], and also used in [68] to derive the spreading factor of the reflected wave from a curved PEC surface.

Differently from [70], here we express wave curvatures using 3x3 non-diagonal curvature matrices, avoiding the use of a ray-fixed local reference system on the incident and reflected wave to diagonalize them, that would need multiple matrix transformations. As a starting point, by substituting (3.1) and (3.15) in (3.14), we get:

$$\begin{aligned}\mathbf{E}_0^r\left(\mathbf{r}'\right)e^{-jk_0\psi^r(\mathbf{r}')} &= \\ &= \underline{\Gamma}_0\left(\mathbf{r}'\right)\mathbf{E}_0^i\left(\mathbf{r}'\right)e^{j\left[\chi^m(\mathbf{r}')-k_0\psi^i(\mathbf{r}')\right]}\end{aligned} \tag{3.17}$$

and then:

$$\mathbf{E}_0^r\left(\mathbf{r}'\right) = \pm\underline{\Gamma}_0\left(\mathbf{r}'\right)\mathbf{E}_0^i\left(\mathbf{r}'\right) \tag{3.18a}$$

$$k_0\psi^r\left(\mathbf{r}'\right) = k_0\psi^i\left(\mathbf{r}'\right) - \chi^m\left(\mathbf{r}'\right) \tag{3.18b}$$

Eq. (3.18b) is a phase-matching relation that involves the phase of incident and reflected fields, and the phase χ^m imposed by the RIS. By expressing each phase term through its Taylor series expansion about a reference point $\mathbf{r}'_0$ on the RIS, a simple relation between the local curvature matrices of the incident and reflected fields can be derived, as shown in Appendix A:

$$\mathbf{t}\cdot\underline{\mathbf{Q}}^r\mathbf{t} = \mathbf{t}\cdot\left\{\left[\underline{\mathbf{Q}}^i - \frac{1}{k_0}\nabla\nabla\chi^m\left(\mathbf{r}'_0\right)\right]\mathbf{t}\right\} \tag{3.19}$$

where $\mathbf{t} = \mathbf{r}' - \mathbf{r}'_0$ is any vector tangent to the RIS surface at $\mathbf{r}'_0$, and $\nabla\nabla\chi^m$ is the Hessian matrix of the phase profile χ^m imposed by the RIS, computed in $\mathbf{r}'_0$.

In order for (3.19) to be satisfied, the tangent projection of the incident curvature matrix, plus the curvature imposed by the RIS, must equate the tangent projection of the reflected curvature matrix, i.e.:

$$\underline{\mathbf{P}}_\tau\underline{\mathbf{Q}}^r\underline{\mathbf{P}}_\tau = \underline{\mathbf{P}}_\tau\left[\underline{\mathbf{Q}}^i - \frac{1}{k_0}\nabla\nabla\chi^m\right]\underline{\mathbf{P}}_\tau \tag{3.20}$$

Eq. (3.20) only provides the tangential component of $\underline{\mathbf{Q}}^r$. The normal component is determined by imposing (3.6) for the reflected ray, i.e.

$$\underline{\mathbf{Q}}^r\hat{\mathbf{s}}^r = \mathbf{0}$$

In particular, by combining (3.6) and (3.20), through simple algebraic manipulations the final expression of $\underline{\mathbf{Q}}^r$ can be found:

$$\underline{\mathbf{Q}}^r = \underline{\mathbf{L}}^T\left[\underline{\mathbf{Q}}^i - \frac{1}{k_0}\nabla\nabla\chi^m\right]\underline{\mathbf{L}} \tag{3.21}$$

where $\underline{\mathbf{L}}$ is a linear transformation operator, having the following form:

$$\underline{\mathbf{L}} = \left(\underline{\mathbf{1}} - \frac{\hat{\mathbf{s}}^r \hat{\mathbf{n}}}{\hat{\mathbf{s}}^r \cdot \hat{\mathbf{n}}} \right) \tag{3.22}$$

According to GO rules, after reflecting on the RIS the wave continues to propagate along a rectilinear trajectory and the curvature radii increase proportionally to the path length, as the medium above the RIS surface is homogeneous. If the incident ray hits the RIS in the point $\mathbf{r}'$, the GO field on a observation point $\mathbf{r} = \mathbf{r}' + s\,\hat{\mathbf{s}}^r$ along the reflected ray is then expressed by:

$$\mathbf{E}^r(\mathbf{r}) = \underline{\boldsymbol{\Gamma}}(\mathbf{r}')\,\mathbf{E}^i(\mathbf{r}')\,A^r(s)\,e^{-jk_0|\mathbf{r}-\mathbf{r}'|} = \underline{\boldsymbol{\Gamma}}(\mathbf{r}')\,\mathbf{E}^i(\mathbf{r}') \sqrt{\frac{\rho_1^r \rho_2^r}{(\rho_1^r + s)(\rho_2^r + s)}}\, e^{-jk_0 s} \tag{3.23}$$

with ρ_1^r, ρ_2^r being the principal curvature radii of the reflected wave at $\mathbf{r}'$, i.e. the reciprocals of the non-zero eigenvalues of the reflection curvature matrix $\underline{\mathbf{Q}}^r$, computed through (3.21), and s the local coordinate along the reflected ray.

It is worth noting that generally, according to (3.21), RIS reflection changes the wavefront shape into an astigmatic wave even in simple cases, like with a spherical wave incident on a constant phase gradient RIS, i.e. with $\nabla\nabla\chi^m = 0$. For instance, let us consider the case of an anomalous reflector configured with constant anomalous angle θ_r, and re-radiation plane coincident with the incidence plane (i.e. $\Delta\phi = 0$ in Fig. 3.1). If such a RIS is illuminated by a spherical wave, i.e. with $\rho_1^i = \rho_2^i = s'$, using (3.21) it can be easily shown that the reflected wave has curvatures $\rho_1^r = s'$ and $\rho_2^r = s' \cos^2\theta_r / \cos^2\theta_i$: the curvature perpendicular to the incidence plane is unchanged, while the one laying in the incidence plane is modified by anomalous reflection. Therefore, the spherical wavefront shape is unchanged only in the case of specular reflection.

3.2.3 Anomalous ray diffraction

Beside the GO contributions for the RIS scattered field, edge diffracted ray-fields are also included in the model. This type of contribution is important to smooth out the abrupt field discontinuity predicted by GO when crossing the shadow boundaries, and to predict a nonzero field in the GO shadow region. Since an exact solution for the truncated RIS canonical problem is not available, the edge diffracted field has to be evaluated by resorting to an approximate solution. Similarly to the approach adopted for the diffraction from arbitrary impedance wedges, two methods are possible; one can either resort to a PO approximate formulation and derive ray contributions from its asymptotic evaluation [75], or develop

heuristic solutions [76], [77] by modifying the UTD coefficient [68]. While in [48] the former methodology was pursued, here we follow the latter which is more popular and effective for the application to ray-tracing and propagation prediction because of its simplicity. Since the total phase progression along the RIS edges results from the combination of both the incident wave illumination and the surface impedance modulation, edge diffracted rays are launched toward anomalous directions, similarly to what happens for GO reflected rays.

Namely, according to a *generalized law of diffraction*, the diffracted ray direction $\hat{\mathbf{s}}^d$ must obey to (see Appendix B for the proof):

$$\begin{aligned} \cos\beta &= \hat{\mathbf{s}}^d \cdot \hat{\mathbf{e}} = \hat{\mathbf{s}}^r \cdot \hat{\mathbf{e}} = \\ &= \left(\hat{\mathbf{s}}^i - \frac{\nabla \chi^m}{k_0}\right) \cdot \hat{\mathbf{e}} = \cos\beta' - \frac{1}{k_0}\frac{\partial \chi^m}{\partial e} \end{aligned} \tag{3.24}$$

where β is the aperture angle of the Keller-Rubinowicz diffraction cone, β' is the incidence angle with respect to the edge and $\hat{\mathbf{e}}$ is the unit vector along the edge, as shown in Fig. 3.2.

Looking at (3.24), it is evident that the additional term corresponding to the spatial modulation modifies the cone aperture with respect to the standard case, thus leading to an *anomalous diffraction*. Moreover, the transverse component of the reflection direction $\hat{\mathbf{s}}^r$

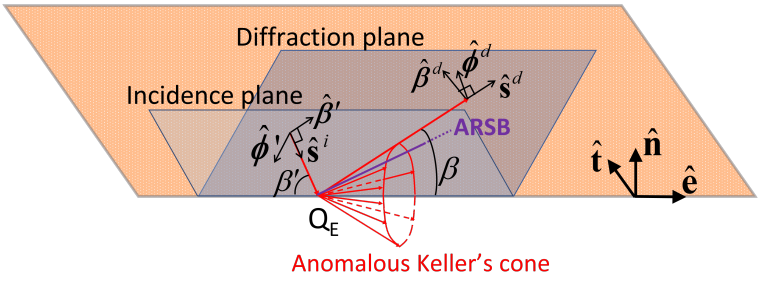

Fig. 3.2 Anomalous Keller's cone and edge-fixed reference system for incident and diffracted ray [51]

with respect to the edge direction $\hat{\mathbf{e}}$ gives rise to an Anomalous Reflection Shadow Boundary. This applies of course to any re-radiation mode of the RIS.

Therefore, one can proceed similarly to the standard UTD case, by recalling that the diffracted wave is astigmatic with one caustic on the edge, and that the diffracted field is computed as [68]:

$$\mathbf{E}^d(s) = \underline{\mathbf{D}} \cdot \mathbf{E}^i(Q_E) \sqrt{\frac{\rho^d}{s\left(\rho^d + s\right)}}\, e^{-jk_0 s} \tag{3.25}$$

In (3.25), $\underline{\mathbf{D}}$ is the dyadic diffraction coefficient, and ρ^d is the edge-caustic distance, i.e. the distance between the caustic at the edge and the second caustic of the diffracted ray.

For a straight edge, ρ^d is related to the incident wave curvature radius on the edge-fixed incidence plane, i.e. ρ_e^i, through the following equation (see Appendix B for the proof):

$$\frac{1}{\rho^d} = \frac{1}{\rho_e^i}\frac{\sin^2\beta'}{\sin^2\beta} - \frac{1}{k_0\sin^2\beta}\frac{\partial^2\chi^m}{\partial e^2} \tag{3.26}$$

Looking at (3.26), it is evident that the curvature of the incident wave on the edge-fixed diffraction plane is modified by anomalous diffraction, similarly to what happens for anomalous reflection. If the RIS has a constant phase gradient along the edge, such curvature ρ^d is also constant along the edge.

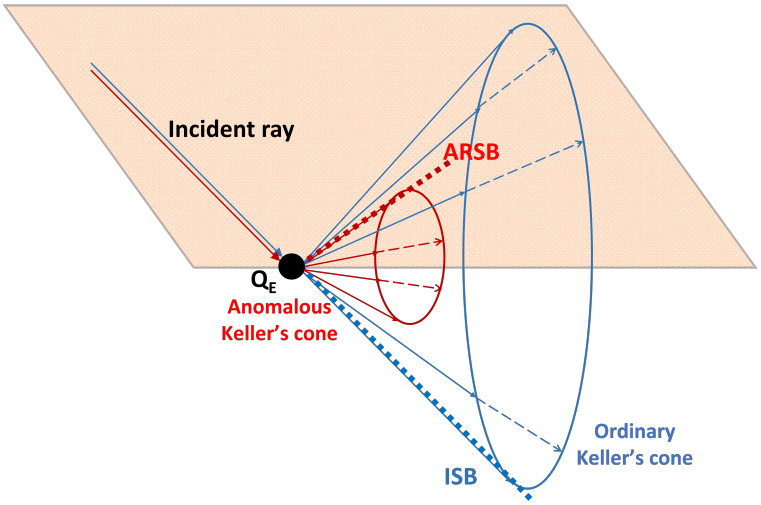

Fig. 3.3 Ordinary and anomalous Keller's cones for a given point along the edge [51]

Diffraction must also compensate for the incident field that vanishes at the Incidence Shadow Boundary (ISB). However, the incident ray boundary is not modified by the surface impedance modulation of the RIS across the edge. This means that, in addition to the anomalous Keller's cone, also an *ordinary* Keller's cone of diffracted rays originates at the diffraction point Q_E (see Fig.3.3), i.e.

$$\cos\beta' = \hat{\mathbf{s}}^i \cdot \hat{\mathbf{e}} = \hat{\mathbf{s}}^{do} \cdot \hat{\mathbf{e}} \tag{3.27}$$

with $\hat{\mathbf{s}}^{do}$ direction of the diffracted ray laying on the ordinary Keller's cone. For those diffracted rays, the incident field curvature is not modified by diffraction on a straight edge, i.e. $\rho^d = \rho_e^i$ [68].

Regarding the dyadic diffraction coefficient $\underline{\mathbf{D}}$ in (3.25), it is expressed as a combination of unit vectors parallel and perpendicular to the incidence and diffraction edge-fixed planes, as in [68]. However, differently from the standard UTD, two separate diffraction coefficients are

defined for the anomalous and ordinary diffracted rays. Therefore, we extend the formulation of the UTD diffraction coefficient to the case of a RIS in the following way:

$$\underline{\mathbf{D}}^i = D^i \left(-\hat{\beta}\hat{\beta}' - \hat{\phi}\hat{\phi}' \right) \tag{3.28}$$

$$\underline{\mathbf{D}}^r = \left(-D_s^r \hat{\beta}^d \hat{\beta}' - D_h^r \hat{\phi}^d \hat{\phi}' \right) \underline{\mathbf{\Gamma}} \tag{3.29}$$

where D^i is the scalar diffraction coefficient that applies to the diffracted rays on the ordinary Keller's cone, D_s^r and D_h^r are the "soft" and "hard" scalar diffraction coefficients [68] for the anomalous diffraction. In (3.29), D_s^r and D_h^r are also multiplied by the spatial modulation coefficient $\underline{\mathbf{\Gamma}}$ to properly compensate for anomalous reflection on the ARSB, following the heuristic approach adopted in [76, 77] for a non-perfectly conducting wedge.

The unit vectors $(\hat{\phi}', \hat{\beta}')$ form a right-handed triplet with the incidence direction $\hat{\mathbf{s}}^i$ (see Fig. 3.2) and similarly, $(\hat{\phi}, \hat{\beta})$ and $(\hat{\phi}^d, \hat{\beta}^d)$ form a right-handed triplet with the ordinary and anomalous diffraction directions $\hat{\mathbf{s}}^{do}$ and $\hat{\mathbf{s}}^d$, respectively. Therefore, they are easily computed as:

$$\begin{aligned} \hat{\phi}' &= -\frac{\hat{\mathbf{e}} \times \hat{\mathbf{s}}^i}{|\hat{\mathbf{e}} \times \hat{\mathbf{s}}^i|} \quad \hat{\phi} = \frac{\hat{\mathbf{e}} \times \hat{\mathbf{s}}^{do}}{|\hat{\mathbf{e}} \times \hat{\mathbf{s}}^{do}|} \quad \hat{\phi}^d = \frac{\hat{\mathbf{e}} \times \hat{\mathbf{s}}^d}{|\hat{\mathbf{e}} \times \hat{\mathbf{s}}^d|} \\ \hat{\beta}' &= \hat{\phi}' \times \hat{\mathbf{s}}^i \quad \hat{\beta} = \hat{\phi} \times \hat{\mathbf{s}}^{do} \quad \hat{\beta}^d = \hat{\phi}^d \times \hat{\mathbf{s}}^d \end{aligned} \tag{3.30}$$

In order to express the scalar diffraction coefficients D^i, D_s^r, D_h^r in (3.28),(3.29) in a similar form to the one introduced in [68] for standard UTD, we need to define the ray angular coordinates with respect to the edge (see Fig.s 3.2-3.4). They can be computed with the following equations [78]:

$$\beta = \arccos\left(\hat{\mathbf{s}}^r \cdot \hat{\mathbf{e}}\right) \tag{3.31}$$

$$\beta' = \arccos\left(\hat{\mathbf{s}}^i \cdot \hat{\mathbf{e}}\right) \tag{3.32}$$

$$\phi^d = \pi - \left[\pi - \arccos\left(\frac{\hat{\mathbf{s}}^d \cdot \hat{\mathbf{t}}}{\sin\beta}\right)\right] \operatorname{sgn}\left(\frac{\hat{\mathbf{s}}^d \cdot \hat{\mathbf{n}}}{\sin\beta}\right) \tag{3.33}$$

$$\phi'^r = \pi - \left[\pi - \arccos\left(\frac{-\hat{\mathbf{s}}^r \cdot \hat{\mathbf{t}}}{\sin\beta}\right)\right] \operatorname{sgn}\left(\frac{\hat{\mathbf{s}}^r \cdot \hat{\mathbf{n}}}{\sin\beta}\right) \tag{3.34}$$

$$\phi = \pi - \left[\pi - \arccos\left(\frac{\hat{\mathbf{s}}^{do} \cdot \hat{\mathbf{t}}}{\sin\beta'}\right)\right] \operatorname{sgn}\left(\frac{\hat{\mathbf{s}}^{do} \cdot \hat{\mathbf{n}}}{\sin\beta'}\right) \tag{3.35}$$

$$\phi' = \pi - \left[\pi - \arccos\left(\frac{-\hat{\mathbf{s}}^i \cdot \hat{\mathbf{t}}}{\sin\beta'}\right)\right] \operatorname{sgn}\left(\frac{-\hat{\mathbf{s}}^i \cdot \hat{\mathbf{n}}}{\sin\beta'}\right) \tag{3.36}$$

with $\hat{\mathbf{n}}$ denoting the unit vector normal to the RIS and $\hat{\mathbf{t}} = \hat{\mathbf{n}} \times \hat{\mathbf{e}}$ the unit vector tangent to the RIS and orthogonal to the edge.

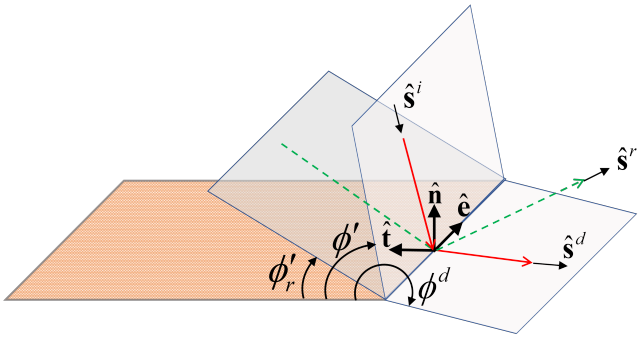

Fig. 3.4 Diffraction angles for anomalous diffraction. Red: incident ray and one anomalous diffracted ray with corresponding incidence and diffraction planes; Green: anomalous reflected ray and its opposite (back-specular) direction [51]

Compared to the standard UTD, in (3.31)-(3.36) three additional angles are introduced, namely β, ϕ^d and ϕ'^r : β is the angle formed by the anomalous Keller's cone with the edge direction $\hat{\mathbf{e}}$, and is different from the incidence angle β', in accordance with (3.24); ϕ^d defines the observation angle on the anomalous Keller's cone, projected on the transverse plane to the edge, while ϕ'^r is the transverse angle defining the specular direction of $\hat{\mathbf{s}}_r$ (see Fig. 3.4) so that the diffraction coefficient exhibits its transition at the ARSB, i.e. when $\phi^d + \phi'^r = \pi$ or $\phi^d + \phi'^r = 3\pi$.

The Incidence Shadow Boundary condition is $|\phi - \phi'| = \pi$ and is unchanged w.r.t. the standard UTD.

Of course, if the RIS has a specular radiation mode, this gives rise to a standard UTD diffraction, where all the diffracted rays lay on the ordinary Keller's cone, i.e. $\beta = \beta'$, and the ARSB becomes the ordinary Reflection Shadow Boundary, i.e. $\phi^d = \phi$ and $\phi'^r = \phi'$. In the standard UTD from a wedge, the diffraction coefficient is formed by two couples of cotangent terms (one for each face of the wedge), that maximize the coefficient on the ISB and on the RSB, respectively. However, since a RIS is a diffracting half-plane, each couple of cotangents degenerates into a single secant term [68]. Moreover, in the case of a RIS these secant terms are not summed together to form a single coefficient as in standard UTD, as they are applied separately to diffracted rays that belong to different Keller's cones.

Therefore, for a RIS properly designed in order to have a single significant (anomalous) re-radiation mode, while the other propagating modes including the specular one are negligible, the scalar UTD coefficients to be used in (3.28),(3.29) are expressed by:

$$D^i = \frac{-e^{-j\pi/4}}{2\sqrt{2\pi k_0}\sin\beta'} \frac{F\left[k_0 L^i a\left(\phi - \phi'\right)\right]}{\cos\left[\left(\phi - \phi'\right)/2\right]} \tag{3.37}$$

$$D^r_{s,h} = \mp \frac{-e^{-j\pi/4}}{2\sqrt{2\pi k_0}\sin\beta} \frac{F\left[k_0 L^r a\left(\phi^d + \phi'^r\right)\right]}{\cos\left[\left(\phi^d + \phi'^r\right)/2\right]} \tag{3.38}$$

where

$$F(X) = 2j\sqrt{X}\, e^{jX} \int_{\sqrt{X}}^{\infty} e^{-ju^2}\, du \tag{3.39}$$

is the UTD Fresnel Transition function, with arguments

$$a\left(\phi \pm \phi'\right) = 2\cos^2\left(\frac{\phi \pm \phi'}{2}\right) \tag{3.40}$$

and distance parameters

$$L^i = \frac{s\left(\rho^i_e + s\right)\rho^i_1 \rho^i_2}{\rho^i_e\left(\rho^i_1 + s\right)\left(\rho^i_2 + s\right)} \sin^2\beta', \tag{3.41}$$

$$L^r = \frac{s\left(\rho^d + s\right)\rho^r_1 \rho^r_2}{\rho^d\left(\rho^r_1 + s\right)\left(\rho^r_2 + s\right)} \sin^2\beta. \tag{3.42}$$

In (3.41), ρ^i_1, ρ^i_2 are the principal curvature radii of the incident wave, while ρ^i_e is the curvature radius of the incident wave on the edge-fixed incidence plane (see Fig. 3.2). Instead, in (3.42) ρ^r_1, ρ^r_2 are the principal curvature radii of the reflected wave, computed through (3.21), while ρ^d is the edge-caustic distance, computed through (3.26). In the small argument limit $F(X \to 0) \simeq \sqrt{j\pi X}$, it is easy to verify that the factor $\sqrt{L^{i,r}}$ transforms the diffracted field spreading factor into the GO one. As a consequence, the distance parameters in (3.41), (3.42) ensure that, at the relevant SB where the arguments (3.40) vanish, the edge diffracted field exhibits a jump discontinuity compensating the GO abrupt disappearance, thus providing a continuous total field across the SB. This property of the standard UTD, is here suitably extended to the ARSB.

As a last remark, it must be noted that the diffraction coefficients (3.37),(3.38) apply to different diffracted rays (ordinary and anomalous) that originate from the same point Q_E on the edge, and the corresponding diffracted fields also have different spreading factors and propagate in different directions, which corresponds to a forward ray-tracing perspective. Therefore, the diffraction coefficients cannot be summed, unlike in standard UTD. Conversely, by assuming a backward ray-tracing perspective, a fixed observation point P in the space might be hit by diffracted rays that originate at two different diffraction points (or "critical points") on the edge [79], i.e. those points which satisfy (3.24) and (3.27). In such a case,

Algorithm 1 Computation of the RIS re-radiated field

```
Read TX information
Define RX grid
for k ← 1 to N_tiles do
    Calculate incident field E^i on tile k
    for n ← 1 to N_modes do
        Use (3.13) to find the re-radiation direction
        Intersect the re-radiated beam with the RX grid
        Compute the SMD Γ on tile k using (3.15)
        Calculate curvature matrix using (3.21)
        Calculate reflected field E^r for mode n using (3.23)
        Add ray contribution to total field at RX
    end for
    if tile k is a "border tile" then
        Calculate incident field on the tile edge
        for n ← 1 to N_modes do
            Find the anomalous Keller's cone with (3.24)
            Intersect Keller's cone with the RX grid
            Calculate UTD coefficient using (3.29)
            Calculate ρ^d using (3.26)
            Calculate diffr. field E^d for mode n using (3.25)
            Add ray contribution to total field at RX
        end for
        Find the ordinary Keller's cone with (3.27)
        Intersect Keller's cone with the RX grid
        Calculate UTD coefficient using (3.28)
        Calculate diffracted field E^d using (3.25)
        Add ray contribution to total field at RX
    end if
end for
```

the total diffracted field in P is expressed by

$$\begin{aligned}\mathbf{E}^d_{TOT}(P) = \underline{\mathbf{D}}^i \cdot \mathbf{E}^i(Q_{E1}) \sqrt{\frac{\rho^i_e}{s_1(\rho^i_e + s_1)}}\, e^{-jk_0 s_1} \\ + \underline{\mathbf{D}}^r \cdot \mathbf{E}^i(Q_{E2}) \sqrt{\frac{\rho^d}{s_2(\rho^d + s_2)}}\, e^{-jk_0 s_2}\end{aligned} \tag{3.43}$$

where s_1, s_2 are the distances between the critical points Q_{E1}, Q_{E2} and the observation point P, respectively, and ρ^d, $\underline{\mathbf{D}}^i$, $\underline{\mathbf{D}}^r$ are computed using (3.26), (3.28) and (3.29). If the RIS

has multiple re-radiation modes, additional critical points arise, and additional terms of anomalous diffraction are added to (3.43).

3.2.4 Computation of the overall re-radiated field

The procedure for the computation of the re-radiated field from a finite-size RIS using the proposed ray approach is summarized in Algorithm 1. The RIS is first subdivided into tiles, and the procedure is iterated over the different tiles and over the different RIS re-radiation modes: finally, the reflected and diffracted fields are coherently summed to get the overall re-radiated field.

3.3 Application examples

As a first simple benchmark case, we consider a "perfect" anomalous reflector [36, 29], illuminated with a plane wave at normal incidence. The RIS has size $7 \times 7\,m^2$, is centered in the origin of an orthogonal reference system $Oxyz$, and lays on the xy plane. Furthermore, the RIS is designed for an anomalous reflection angle $\theta_r = 60^\circ$, and a normal incident wave with perpendicular (TE) polarization with respect to the xz plane, at the frequency of $3.5\,GHz$. This can be accomplished by setting the following expressions in the SMD coefficient (3.15):

$$\chi^m = k_0(\sin\theta_i - \sin\theta_r)x$$
$$A^m = \sqrt{\cos\theta_i/\cos\theta_r}$$
$$\underline{\mathbf{R}}^m = \hat{\mathbf{y}}\hat{\mathbf{y}}$$

This means that the RIS imposes a constant phase gradient $\nabla\chi^m = k_0(\sin\theta_i - \sin\theta_r)\hat{\mathbf{x}}$ along the x axis, the wave polarization is perpendicular to the re-radiation plane and is not altered by the RIS, while the term $A^m = \sqrt{\cos\theta_i/\cos\theta_r}$ accounts for global power conservation [29]. Such kind of "perfect" anomalous reflector with a single re-radiation mode and global power conservation requires a non-local design of the surface impedance through excitation of additional auxiliary evanescent fields or by carefully engineering the surface reactance profile, and can be achieved for example with a nonuniform array of metal patches separated by a dielectric layer from a ground plane, as described in [36].

In Fig. 3.5, the distribution of the re-radiated E-field computed with the ray model on the xz plane is shown, assuming a unitary incident field $\mathbf{E}^i = (-1\,V/m)\hat{\mathbf{y}}$ at the RIS surface. Being an high-resolution image, interference fringes caused by edge diffraction are well visible, both inside and outside the reflection cone. The result of Fig. 3.5 is very similar to the one shown in [49, Fig. 4] except for a small scale factor in the values of the

re-radiated field, as this previous result was obtained using a different model, called "Antenna Array-Like" model, and applied to the case of an *ideal* phase-gradient reflector, by using a "locally-specular" reflection assumption, which can cause a small bias error, as mentioned in [49].

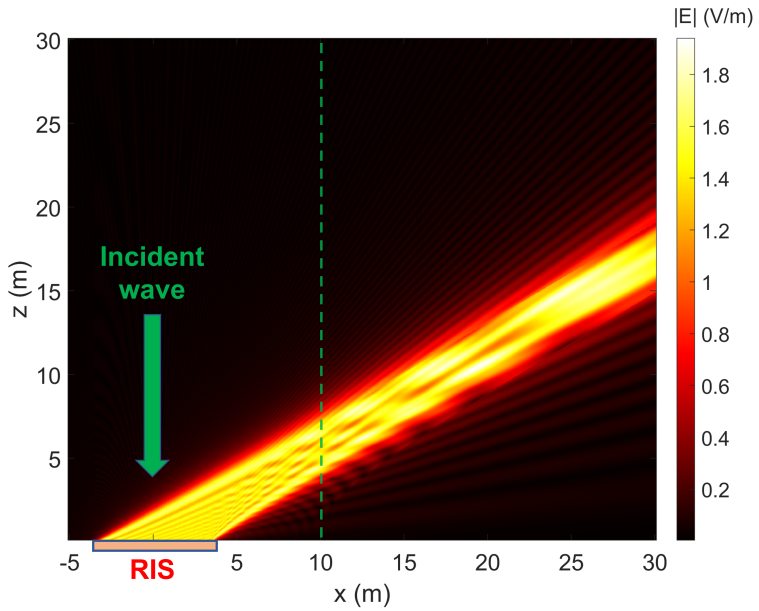

Fig. 3.5 Field distribution for a perfect anomalous reflector, with $\theta_i = 0°$, $\theta_r = 60°$. Frequency: $f = 3.5\ GHz$. TE-polarized incident plane wave, with $\left|\mathbf{E}^i\right| = 1\,V/m$ at the RIS surface [51]

In order to show the effectiveness of the proposed approach, the scattered field computed with the ray model and shown in Fig. 3.5 is compared with the one computed using the PO approach, which is well-proven and widely used [47]. The PO field is computed through the following radiation integral:

$$\mathbf{E}^s_{PO}(\mathbf{r}) = -\frac{jk_0}{4\pi}\int_S \frac{e^{-jk_0|\mathbf{r}-\mathbf{r}'|}}{|\mathbf{r}-\mathbf{r}'|}[\eta\,\hat{\mathbf{r}}\times\mathbf{J}_S(\mathbf{r}')\times\hat{\mathbf{r}} + \mathbf{M}_S(\mathbf{r}')\times\hat{\mathbf{r}}]dS \tag{3.44}$$

where the equivalent surface currents for an impenetrable metasurface are approximated as [47]:

$$\begin{aligned}\mathbf{J}_S &= \hat{\mathbf{n}}\times(\mathbf{H}^i + \mathbf{H}^r)\\ \mathbf{M}_S &= -\hat{\mathbf{n}}\times(\mathbf{E}^i + \mathbf{E}^r) = -\hat{\mathbf{n}}\times(\mathbf{E}^i + \underline{\Gamma}\,\mathbf{E}^i)\end{aligned} \tag{3.45}$$

with

$$\mathbf{H}^{i,r} = \frac{1}{\eta}\hat{\mathbf{s}}^{i,r}\times\mathbf{E}^{i,r} \tag{3.46}$$

By comparing the whole predicted field in Fig. 3.5 with the one obtained using the PO model on the same Rx grid, one obtains that the RMS distance between the two models

is about 2.1% of the unit incident field. The reference PO solution is obtained through numerical computation of the integral (3.44) with a discretization of the RIS into tiles of length $\lambda/2$, the minimum resolution to have a reliable prediction without grating lobes [49]. It is worth noting that both the ray and the PO solutions are slightly approximate, albeit in different ways, the first being based on an asymptotic approximation of the field for high frequencies, and the second on the assumption that the total field is zero on the shadow side of the RIS and the radiating currents are not perturbed near the edges. However, the ray-based approach is intrinsically more efficient. Just to have an idea, to produce the high resolution image of Fig. 3.5 (1.2 Mpixel) with numerical solution of the integral (3.44), using MATLAB on a workstation with Intel(R) Xeon(R) E5-2620 CPU and parallelization on 8 cores, it takes about 17 hours and 45 minutes. On the contrary, the same result can be obtained with the ray model in about 200 seconds. Results are summarized in Table 3.1 in terms of mean error, standard deviation of the error and RMS error with respect to the reference PO model, and computation time. The errors are expressed as a percentage of the unit incident field. Table 3.1 also reports the AAL model of [49], which has intermediate performance: the mean error is slightly worse and the error standard deviation is slightly better than the ray model, but its computation time is of about 2 hours and 26 minutes, which is 43 times slower than the ray model.

Table 3.1 Accuracy and computation time of ray model and AAL model with respect to the reference PO model [51]

Model	Mean error	Error std deviation	RMS error	Computation time (s)
PO model	—	—	—	63918
AAL model	0.19%	1.33%	1.35%	8767
Ray model	0.16%	2.07%	2.08%	200

In order to provide a visual comparison between the proposed ray model and the PO reference model, the re-radiated field shown in Fig. 3.5 is sampled along the RX line at $x = 10$, $y = 0$ (green dashed line) and compared with the one obtained using the PO model in the same Rx locations. The comparison is shown in Fig. 3.6 where the re-radiated field obtained through the ray model is represented by the black curve, while red dotted curve corresponds to the PO model. The AAL is not plotted in this case for readability reasons, as the curves are very close each other. It is evident that the 2 curves in Fig. 3.6 are nearly coincident, thus confirming the validity of the adopted approach. The only small difference that can be appreciated, at $z = 7$, is due to the absence in the model of vertex diffraction, which would allow for a smoother transition when edge ray diffraction ceases to exist.

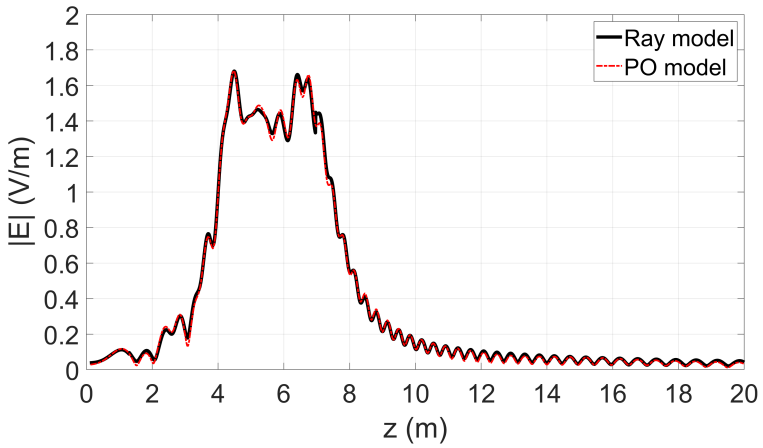

Fig. 3.6 Comparison of the ray model with the PO model along the dashed green line in Fig.3.5 [51]

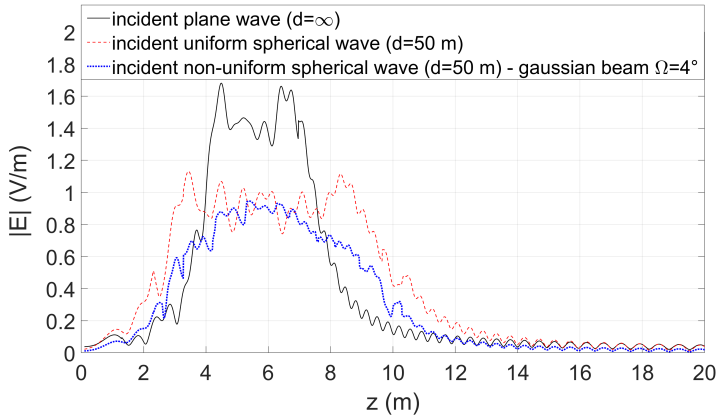

Fig. 3.7 Comparison of the re-radiated field predicted with the ray model along the dashed green line in Fig.3.5 in 3 different cases: a) incident plane wave (black line), b) incident uniform spherical wave (red dashed line), c) incident non-uniform spherical wave with gaussian profile and divergence $\Omega = 4^\circ$ (blue dotted line) [51]

.

Anomalous reflectors are usually conceived and designed for the canonical case of an incident plane wave from a given direction, but in a real environment the incident wave is spherical (or astigmatic), unless the illuminating source is very far. This fact causes an impact on RIS performance, as depicted in Fig. 3.7, where the same RIS of the previous example is considered (perfect anomalous reflector) and the field along the green dashed line in Fig. 3.5 is computed with the ray model for an illuminating spherical source located along the z-axis, at a distance of 50 m from the RIS center. The incident field is normalized so that its maximum value, at the center of the RIS, is $1\,V/m$. Fig. 3.7 shows a significant widening of the reflection cone and a reduction in the amplitude of the re-radiated field for a uniform spherical incident wave (red dashed curve) compared to the reference case of plane wave illumination (black curve). This is mainly due to the fact that the incidence phase gradient is not constant along the RIS surface, and then the phase compensation operated by

the RIS is imperfect. Moreover, the reflected wave is astigmatic, as discussed in Section II, and therefore attenuates faster with distance than a spherical wave.

The re-radiated field intensity is further reduced if the RIS is illuminated with a directive antenna. As a reference example, Fig. 3.7 depicts the case of illumination with a circular gaussian beam (blue dotted curve), that can well approximate the main radiation lobe of a pencil-beam directive antenna [80]. The considered gaussian beam has beam waist $w_0 = 0.39\ m$, corresponding to a divergence angle $\Omega = \frac{\lambda}{\pi w_0} \approx 4°$ at $f = 3.5\ GHz$. As the distance from the source ($d = 50\ m$) is far beyond the Rayleigh distance, the incident wave on the RIS surface is a non-uniform spherical wave, and about 86% of its power is contained on a circular spot with radius $R = \Omega d \approx 3.5\ m$ [81]. As expected, in this case the re-radiated field intensity further decreases compared to the case of incident uniform spherical wave (red dashed curve), especially in the side regions of the reflection cone, where the reduction is of about 6 dB: in fact, since most of the incident power is concentrated around the RIS center, the contribution of edge diffraction becomes less significant in this case.

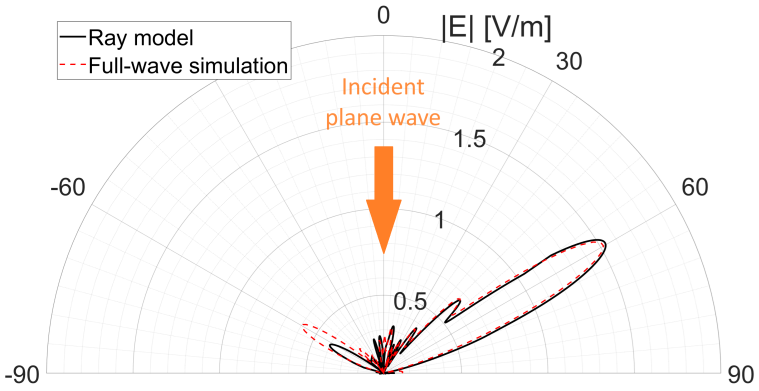

Fig. 3.8 Comparison between ray model and full-wave simulation along a semicircle on the xz plane centered on the RIS, at a distance $r = 1\,m$ [51]

Fig. 3.8 shows a more realistic case of a periodic phase-gradient RIS with multiple propagating modes. The ray model is compared with full-wave simulations performed with the frequency-domain solver (FEM) of CST microwave studio. Similarly to the previous cases, we consider the reference case of a normally incident plane wave, with field amplitude $E_0 = 1\ V/m$ on the RIS surface. The RIS is located in the xy plane, centered at the origin, and consists of a reactive impedance sheet $Z_s(x) = j\eta \tan(\frac{\pi x}{D})$ with period D along the x axis, while the incident field is TE-polarized (i.e. along the y axis). The period can be found as $D = \lambda / |\sin\theta_i - \sin\theta_r|$, in accordance with [36, 47]: therefore, it is chosen as $D = 98.91$ mm in order to give a reflection angle $\theta_r = 60°$ on the xz plane at $f = 3.5\,GHz$. To limit the computation time, the size of the RIS in the CST simulation was chosen to be $7D \times 7D$, i.e. about $0.7 \times 0.7\,m^2$. The surface impedance profile was sampled at 20 points in each period,

so that the RIS model consists of 140 strips of length $7D$ and width $\frac{D}{20}$, each with a constant surface impedance boundary condition. The re-radiated field is sampled along a semicircle in the xz plane at a distance $r = 1\,m$ from the center of the RIS.

In order to compare the full-wave simulation with the ray model, the amplitude and initial phase for the propagating modes have been obtained by first simulating in CST a single periodic cell of the RIS with periodic boundary conditions and Floquet port excitation. According to the Floquet theory, in the considered case of a normally incident plane wave, there are three scattered propagating modes $n = -1, 0, 1$ [47]: $n = 1$ corresponds to the desired re-radiation mode at $\theta = 60^\circ$, while $n = 0$ and $n = -1$ correspond to the specular mode ($\theta = 0^\circ$) and to the opposite mode at $\theta = -60^\circ$, respectively. The S-parameters calculated by CST directly provide the amplitude A^m and phase χ^m of the scattered modes which are used in (3.15) to obtain the spatial modulation coefficient $\underline{\underline{\Gamma}}$ for each mode. Then, the procedure described in Section II is iterated to obtain the total re-radiated field for each of the 3 propagating modes, and such fields are coherently summed to obtain the result shown in Fig. 3.8 (black curve), which is compared with the reference full-wave simulation (red dashed curve). In both curves, the 2 lobes at $\theta = 60^\circ$ and $\theta = -60^\circ$ are clearly visible, whereas the specular mode appears to be almost negligible, except for a few grating lobes. It is apparent that the proposed ray-method can predict the RIS scattering with good accuracy. Overall, the RMS distance between the 2 curves is equal to 0.019, i.e. 1.9% of the unit incident field. The direction and level of the main lobes are quite well estimated except for the underestimation of the lobe at $\theta = -60^\circ$ corresponding to the mode $n = -1$. Such a difference is due to the fact that the ray-method is based on the PO currents, i.e., on the equivalent currents in the infinite periodic problem, which are only an approximation of the the true currents on the truncated structure calculated by the full-wave method. As the difference between the two currents is mainly concentrated at the plate edges, the edge diffraction as predicted under the PO approximation may differ from exact edge diffraction. However, such a difference generally decreases as the electrical size of the RIS increases. In this moderate-size example it is still noticeable, though not dramatic.

As a last example, we consider an *ideal* focalizing reflector, illuminated by a TE-polarized plane wave with $\left|\mathbf{E}^i\right| = 1\,V/m$ and incidence angle $\theta_i = \pi/3$ on the xz plane, at the frequency $f = 3.5\,GHz$: this is achieved by setting $A^m = 1$ and $\chi^m = -\chi^i + k_0\left|\mathbf{r}_F - \mathbf{r}'\right|$ in (3.15), where $\chi^i = -k_0 \sin\theta_i\, x$ is the phase of the incident wave and $\mathbf{r}_F$ is the position vector of the focus point [49]. The RIS has the same size as the one considered in the example of Fig. 3.5, and it is centered in the point $(0, 0, -10)$, while the focus point is located in the origin of the reference system.

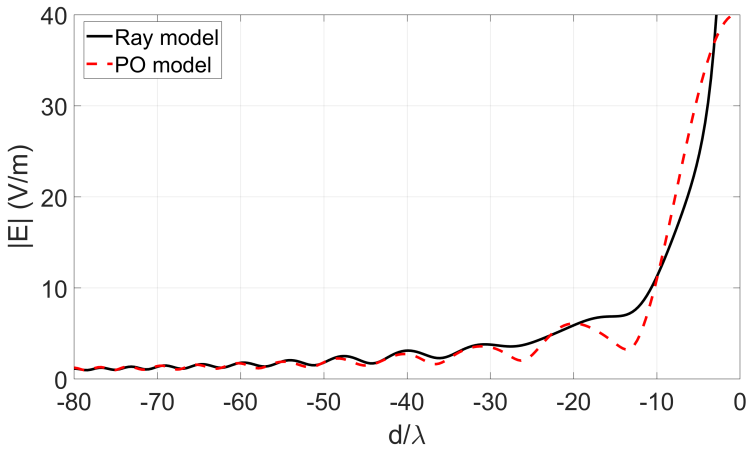

Fig. 3.9 Comparison between the ray model and the PO model in the case of an ideal focalizing reflector. The distance from the focus is normalized with respect to the wavelength [51]

Fig. 3.9 shows the predicted field along the z-axis, starting from the RIS surface up to the focus point, and compares the proposed ray model with the PO model. In the plot, distance from the focus is normalized to the wavelength, to give a clear idea of the focal-spot size that must be related to the wavelength (radius of about 5λ). Recalling that the GO field has singularities on caustics (or focii), as mentioned in Section II, it can be observed that the ray model provides reliable results and in good agreement with the PO model up to a distance of about 5λ from the focus, then the predicted field value starts diverging. Proper handling of singularities in focal points will have to be addressed in future work, together with the introduction of vertex diffraction and extension of the model to transmissive surfaces.

3.4 Conclusions

On the base of the characterization of a finite-size, reflective RIS through a "spatial modulation" dyadic function and a few parameters, in the present work we propose a fully ray-based approach for the computation of the re-radiated field that can be easily embedded in efficient, forward ray tracing algorithms. The model is based on the computation of the anomalous direction of the reflected or diffracted ray based on the phase gradient of the spatial modulation function, and on the computation of its spreading factor using the curvature matrix of the local wavefront. We show that a new Keller's cone, the "anomalous Keller cone", has to be taken into account in addition to the ordinary one and a new, original formulation of the UTD diffraction coefficients is proposed inspired by the heuristic approach in [76, 77]. We validate the proposed model by comparison to well established methods available in the

literature: results show that the ray model is far more efficient in term of computation time, but corresponding results are very similar in a number of benchmark cases.

Chapter 4

Mm-wave building penetration losses: A measurement based critical analysis

Index Terms *Floor penetration loss, mm-wave frequencies, Outdoor-to-indoor propagation*

4.1 Introduction

In the field of wireless communication, ensuring seamless indoor radio coverage, either from outdoor or indoor base stations or access points, is of paramount importance. Unfortunately, wall and floor penetration attenuation heavily hinder it, especially at mm-wave frequencies. Strong attenuation leads to a twofold outcome: it is undesirable when the primary goal is uninterrupted coverage, yet it can suppress interference, which is desirable in many applications. One key propagation mechanism in buildings is O2I propagation, especially in small-indoor residential and industrial environments, where the installation of dedicated micro-cells or repeaters is not cost-effective. In O2I propagation two different elements can be considered: Building Entry Loss and Building Penetration Loss. As per ITU Recommendation [3], the difference between the mean signal level outside of the illuminated façade of the building and the mean signal level just inside the building, in the proximity of the same wall, is defined as BEL. BEL strongly depends on the wall materials, construction technique [82] and on the operating frequency. BPL, on the contrary, includes the BEL plus the attenuation due to propagation inside the building, therefore it includes extra loss due to internal walls and furniture. The recent use of new frequency bands at higher frequencies for fifth- and sixth-generation cellular networks, will aggravate coverage-related problems since both isotropic path-loss and wall/floor insertion loss will become higher [83, 84]. At the same time, going towards very high frequencies determines a very high

cost of RF components. Therefore, the spectrum below 6 GHz and at the low mm-wave bands at around 27 and 38 GHz still represents a good choice for near-future communication systems [85, 86]. Various measurement campaigns related to O2I propagation have been documented in the existing literature [4, 87, 83, 88–90]. Nonetheless, O2I propagation at mm-wave frequencies is still scarcely investigated in old southern-European buildings, that are characterized by thick walls and brick construction.

Another critical propagation mechanism that has received insufficient attention at mm-wave frequencies is through-floor propagation which is essential for minimizing co-channel interference between adjacent floors. The knowledge gap in through-floor attenuation at mm-frequencies is reflected in the lack of standardized models for this case. The only complete characterization of through-floor propagation is limited to lower frequencies [5, 7]. In [91] authors characterize path loss between floors up to 37 GHz, although these measurements were not point-to-point, and no specific correlation between the type of floor and penetration loss was established. O2I and floor propagation heavily depend on the building's structural characteristics and the considered frequency. For this reason, it is essential to conduct multiple measurements with different kinds of buildings and different frequencies. The models proposed by standardization bodies such as ITU/3GPP [3] [92] seem to lack flexibility in accommodating this diversity. Hence, there is a necessity for more adaptable models specifically designed for mm-wave propagation.

The aim of this chapter is to examine O2I propagation - in terms of BEL and BPL - in two distinct buildings as well as through-floor propagation at 27 and 38 GHz across five representative types of buildings, each characterized by different construction materials and techniques. Following preliminary work reported in [93], the same O2I measurement campaign has been repeated employing a fixed transmitter instead of a drone since potential ambiguity was found coming from the unreliable pointing of the illuminating antenna due to drone instability. Moreover, through-floor attenuation in different buildings in terms of both mean attenuation and short-term spatial fluctuations of attenuation over different floor spots has been investigated. Attenuation through 2 floors was also measured when the power-budget was sufficient for the purpose.

Based on the measurements outcome, simple, parametric formulations for both O2I and through-floor attenuation are proposed and tentative parameter values are provided for different building types, frequencies, and number of interposed floors. In particular, the proposed BPL formula is derived as an extension of a previously developed formula for indoor propagation [94] : thanks to the use of simple, physically relatable parameters, the formula is shown to yield good agreement with measurements in the considered scenarios.

In Section 4.2, the measurement setup for both the O2I and through-floor attenuation measurements is described, while the parametric models for O2I and through-floor attenuation are presented in Section 4.3 Measurement results are analyzed and discussed in Section 4.4, and proper parameters are derived for the through-floor attenuation model in different types of buildings. Furthermore the proposed through-floor model has been verified with a blind test in a different sixth building, with same construction characteristics as one of the representative buildings considered in this study. Finally, conclusions are drawn in Section 4.5.

While the previous chapters focused on modeling RIS to engineer the wireless environments, another critical aspect of high-frequency propagation is the attenuation caused by building materials. Therefore, this chapter presents a measurement-based analysis of O2I penetration losses and through-floor attenuation across different buildings, providing insights that can complement and motivate the macroscopic and ray-based RIS models discussed earlier. By quantifying the attenuation of specific materials, we establish a foundation for assessing the effectiveness of RIS in mitigating signal losses in indoor environments

4.2 The measurement campaign

The equipment used during the measurements consisted of a SAF signal generator [95] at the transmitter side and a SAF spectrum analyser [96] at the receiver side. A horn antenna was fed by the signal generator in both campaigns at the transmitter side. Meanwhile, at the receiver side a horn antenna was used to characterize the propagation through floors and an omnidirectional antenna was required for O2I measurements in order to mimic a typical user equipment antenna and to capture all multipath components which contribute to the overall value of the received power. The characteristics of the measurement setups utilized in the two aforementioned campaigns, are summarized in Table 4.1.

4.2.1 Outdoor-to-indoor measurement setup

O2I propagation is a complex propagation process that consists of propagation through the external illuminated wall of the building and additional propagation through inner walls. To identify the different contributions here BEL has been considered as an indicator of the losses that the signal suffers from as it penetrates through the external illuminated wall only. On the other hand, BPL includes the BEL plus the attenuation experienced by the signal while propagating deeper into indoor premises, including indoor partition wall attenuation. In this study, measurements are conducted in a residential area for both 27 and 38 GHz.

Table 4.1 Characteristics of the measurement set-up [11]

Parameter	Model	Features
O2I Campaign		
Transmitter	SAF Tehnika J0SSAG14 Signal Generator	Frequency: 26-40 GHz , for Indoor Tx power : 5 dBm, for Outdoor Tx power : -3 dBm
Receiver	SAF Tehnika J0SSAP14 Spectrum Analyzer	Frequency : 26-40 GHz , Sensitivity : -111 dBm
Amplifier	Eravant SBP-2734033020-KFK-S1	Gain at 27 GHz: 28 dBi , Gain at 38 GHz : 27 dBi
Horn antenna	SAF Tehnika J0AA2640HG03 (Height: 2m)	Frequency: 26-40 GHz, HPBW: 12.5°(E-plane), 15°(H-plane)
Omni antenna	Eravant SAO2734030345-KFS1	Frequency : 26-40 GHz , Gain: 3 dBi , HPBW: 45° (E-plane), omni (H-plane)
Through-floor propagation Campaign		
Transmitter	SAF Tehnika J0SSAG14 Signal Generator	Frequency: 26-40 GHz , Tx power : 0 dBm
Receiver	SAF Tehnika J0SSAP14 Spectrum Analyzer	Frequency : 26-40 GHz , Sensitivity : -111 dBm
Amplifier	Eravant SBP-2734033020-KFK-S1	Gain at 27 GHz: 26 dBi , Gain at 38 GHz : 25 dBi
Horn antennas	SAF Tehnika J0AA2640HG03 (Height: 2m)	Frequency:26-40 GHz, Gain : 21 dBi

In order to understand how the O2I propagation is influenced by the type of buildings, a 19-th century residential building and a more modern office building are chosen as the measurement environments. The mobile terminal is placed on a trolley specifically designed for the measurement campaigns, moving it on both outdoor and indoor locations in order to estimate BEL and BPL. The transmitter is placed 30 m far from the illuminated façade of the building, in order for the façade to fall within the main radiation lobe of the transmitting horn antenna. Firstly, the outdoor measurements have been carried out by moving the receiving antenna close to the illuminated façade of the building, along the route indicated as O1O2 in Fig. 4.1.

Indoor measurements are then performed moving the receiver in different routes inside the building as shown by indoor dashed lines in Fig. 4.1. Measurements have been performed on the same route twice, forward and backward, to verify the repeatability of the measurements and increase the number of samples. The BPL is then computed as the received power difference between outdoor and indoor measurements, in this way some systematic errors cancel each other out. On the other hand, in order to estimate BEL, the receiver needs to be moved only on the indoor receivers located close to the external wall: routes I1, I2 and I8 as shown in Fig. 4.1a for the ground floor and routes I1, I2 in Fig. 4.1b for the first floor of the old residential building are considered; routes I1, I2 as shown in Fig.4.1c and routes I1, I2, I3 in Fig. 4.1d for the ground floor and for the first floor of the modern office building respectively are considered. Being the measurement differential, the impact of the antenna gain is negligible for the scope of this study. Since the buildings under consideration are two-floor buildings, indoor measurements are repeated both on the ground floor and on

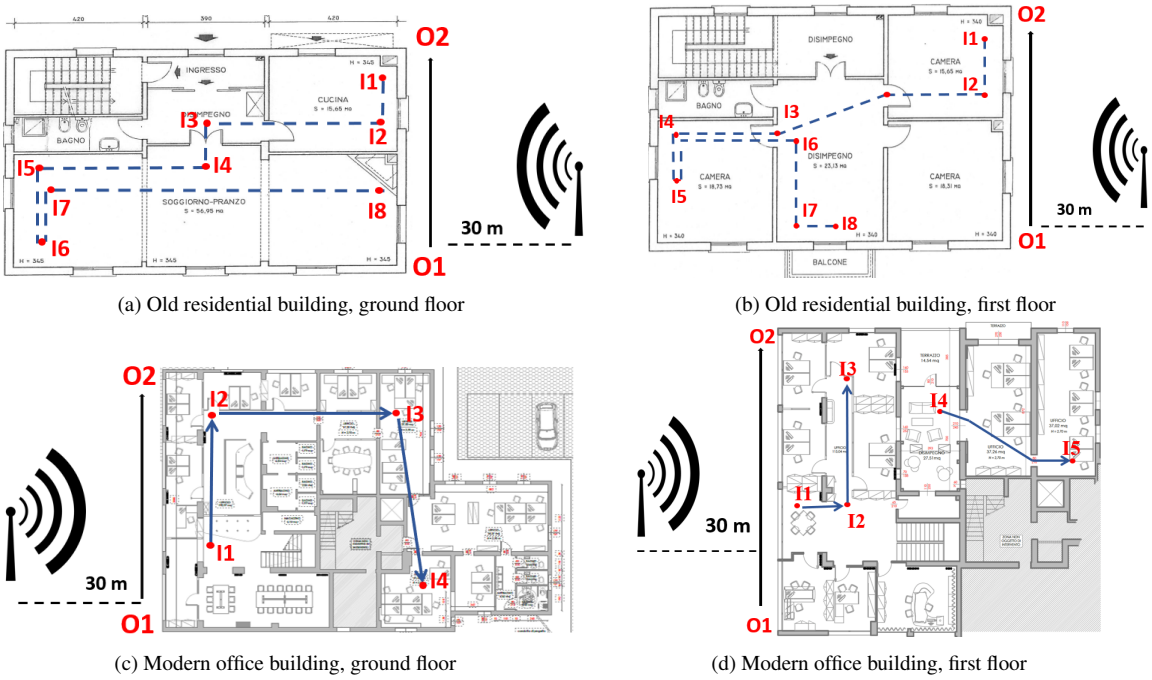

(a) Old residential building, ground floor

(b) Old residential building, first floor

(c) Modern office building, ground floor

(d) Modern office building, first floor

Fig. 4.1 Outdoor/Indoor measurement routes for O2I [11]

the first floor of each building, taking into account the transmit antenna gain values in the direction of each floor. Measurements have also been compared with the 3GPP TR 138 901 model [92], which accounts for O2I propagation for frequencies up to 100 GHz.

4.2.2 Through-floor measurement setup

Measurements regarding the through-floor propagation were performed in five different typical buildings with structures of the floors as shown in Fig. 4.2 where the sixth measurement environment is only used to perform a blind-test on the proposed floor-attenuation model. Both transmitter and receiver antennas have been installed on a tripod designed for

Fig. 4.2 Different environments : Residential 17th century (first) University office of the 1930s (second) University hall of the 1930s (third), University office of the 1980s (fourth), University Hall 2010 (fifth), University building of 1930s used for the blind-test (sixth) [11]

measurement campaigns. Locations of the measured points were chosen in order for the

transmitter and receiver to be vertically aligned in different floors as seen from Fig. 4.3b, obtaining in such way a point-to-point measurement of the floor attenuation. Having a wide set of propagation data is crucial for verifying the measurements reliability. As such, transmitter and receiver are moved to different positions inside the same room/hall where possible, or antennas are rotated by 120° due to a rotor installed in both tripods (see Fig. 4.3a). This way an accurate insight of the losses when signal passes through the floors is achieved. In order to filter out the random like time fluctuations, measurements were repeated 16 times in the same position and the median value of the received power was calculated at the receiver side. Through-floor loss (TFL) in dB is then calculated as the difference between the real measured received power (in dB) and the power one would gain in the free space as if the floor did not exist (in dB), as given by the equation:

$$TFL(dB) = Pr_{measured} - Pr_{Friis} \tag{4.1}$$

Since a considerable number of measured points is obtained in each environment, the mean value of floor loss and its standard deviation are then calculated. These figures can be considered characteristic of each building type, which is related to its construction period, as described in the list below.

1. The first building is an old residential building (first case in Fig. 4.2), constructed in 17-th century, with floors made out of wooden structures. Specifically, the first floor of the building consists of only wooden structures while the second floor has been reinforced lately with a thin layer of concrete, making its structure different with respect to the first floor. Given the differences between the materials that are present in the two floors, floor propagation losses through the first and second floor separately was measured, as well as floor losses through two floors, since the relatively low loss of wooden floors allows to study this case as well. To this aim, since the building is a 3-floor structure, transmitter and receiver are placed in a wing of the building that allows all kind of measurements to be carried out on the same horizontal positions on different floors. Due to potential unevenness in the floor structure of old buildings, measurements of losses through the first floor are repeated 21 times by changing simultaneously with 10 cm step the locations of the transmitter and receiver along a predefined 2m long straight line. The same arrangement is followed for the measurement of losses through the second floor, with a step of 30 cm instead of 10 cm in this case. As for measurements of penetration loss through 2 floors, since furniture did not allow a full 2m scan, measurements on six different spots have been taken, rotating in the same way both antennas on positions A, B, C at an angular distance of

120° from each other, as shown in Fig. 4.3a. This process is repeated twice for each spot.

2. The second scenario is the University office area that was built around 1930 and has floors made of reinforced concrete (second case in Fig. 4.2). In this building, as in the previous old residential building, floor losses on both the first floor and the second floor separately have been investigated. By calculating the losses that each floor exhibits independently, insight on the homogeneity of the building as a whole is achieved, understanding whether measuring attenuation on a single floor alone is sufficient to represent the whole building. Measured points were taken along a straight line, for a total of 16 locations with 30 cm spacing between each-other, forward and backward on the same points for double check.

3. The third measurement environment is the hall of the University building (third case in Fig. 4.2) built around the year 1930, that has floors made of reinforced concrete. Here, apart from the floor thickness (28.5 cm), a 40 cm false ceiling is present, with several cables ducts and pipes. In this scenario, a 2m horizontal scan is performed, moving simultaneously both the transmitter and receiver with a 10cm step on a straight line, as done in the aforementioned old residential building. An attempt to measures losses through two floors was made also in this scenario, but it resulted that, as expected given the reinforced concrete structures, the received signal fell below noise floor.

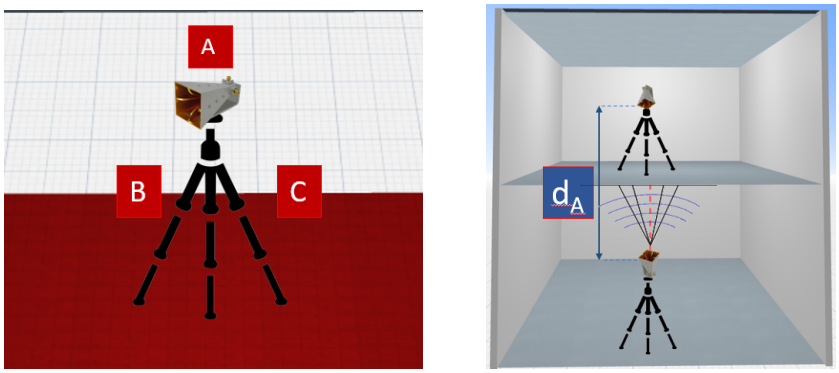

(a) Rotating antennas 120° (b) Antenna setup through 1 floor

Fig. 4.3 Antenna setup for through-floor propagation [11]

4. In the fourth scenario, propagation through floors in more recent University office area built around 1980 is investigated. Metallic beams and metallic supportive structures are present in this type of construction. A 3m scan of the floor with a spacing of 30 cm between different measured points is performed, with some of the points falling directly on a metallic beam.

5. Lastly, the most modern environment is a University building built in 2010 . Floor structure consists of a mixture of reinforced concrete, metal beams, double metal meshes and other metal supportive structures as shown in Fig. 4.7. Here, measurements are performed along a 2m line with a spacing of 10 cm, as before.

4.3 Proposed Propagation Models

On the base of the trends observed in our measurements, we propose in this section simple parametric models for both O2I propagation and Through-Floor attenuation that can adapt to different type of buildings, including southern-European buildings.

4.3.1 Outdoor-to-Indoor path-loss model

Since the 3GPP model [92] does not appear to be very suitable to describe BPL in the southern-European buildings considered in this study, especially when the indoor terminal is located well inside the building, an alternative parametric model is suggested in this section based on a modification of the indoor path-loss formula proposed in [94]. In this study, the formula is extended to account for BEL, as follows:

$$PL_{indoor} = PL_{Friis}(d_0) + BPL \tag{4.2}$$

where PL_{indoor} is the mean path loss (PL) of the outdoor-to-indoor link in dB, PL_{Friis} is free space path loss at the reference distance d_0 at the outer side of the building's wall - assuming free-space outdoor propagation - and BPL is the additional attenuation due to indoor penetration, which includes BEL and indoor propagation as described in [94]:

$$BPL\,(dB) = BEL + 10 * \alpha * log(d/d_0) + \beta * (d - d_0) \tag{4.3}$$

Where, α is the path-loss exponent, β is a specific attenuation constant which accounts for excess attenuation due to the presence of walls or indoor clutter and d is the overall link distance. BEL can be extracted from measurement campaigns in different representative environments, see for example [87, 83, 4, 88–90]. Nevertheless, simple formula such as the one in [97] can be used to compute attenuation through a low-loss slab, if the effective material parameters (real and imaginary part of complex permittivity) of the wall are known at the considered frequencies. As stated in [94], if necessary, a proper fading description can be added to the foregoing formula, that only aims at providing mean O2I attenuation.

4.3.2 Through-floor attenuation model

Since no reference standard model is currently available, in this section we propose a simple parametric model for through-floor attenuation as a function of the number of interposed floors, expressed by (4.4). Let us denote with $\overline{L}$ and n_f, the average floor loss for a single floor and the number of interposed floors, respectively. In equation (4.4), the exponent β is a correction factor (with a value of 1 for propagation through only one floor), which takes into account the non-accumulative nature of losses when passing through multiple floors: β might have a value smaller than 1 in the case of through-multiple floor propagation. χ is a random variable with log-normal distribution that accounts for floor inhomogeneities with σ_L^2 being the building-specific standard deviation of the floor loss.

$$TFL\,(dB) = \overline{L} * n_f^{\beta} + \chi(0, \sigma_L^2) \tag{4.4}$$

Assuming the floor as a homogeneous slab of thickness th floor loss can alternatively be expressed using a specific-attenuation value α_s [dB/cm], that depends on the construction material, as shown in (4.5):

$$\alpha_s\,(dB/cm) = \overline{L}/th \tag{4.5}$$

$\overline{L}$, σ_L^2 and α_s are derived through measurements in buildings of different construction year and type in the present work. Nonetheless, extensive measurements in other building types worldwide are needed to achieve a complete floor-loss table that could lead to the definition of a standard model. Regarding β we don not have enough data available in the present campaign and its determination is left for future work.

4.4 Results and discussion

4.4.1 Outdoor-To-Indoor Propagation

O2I measurements are carried out in two different environments and at two different frequencies: 27 GHz and 38 GHz. The first measurement environment is a brick-wall residential buildings with wooden window frames and wooden window blinds while the second one is an office building with walls made of metal panels, concrete and metal window frames.

Window glass is ordinary glass in both cases. Outdoor reference measurements are collected on O1-O2 routes, while indoor measurements are collected on multiple routes on different floors: see for example ground and first floor routes in Fig. 4.1. A comparison between measured O2I path loss and simulated O2I loss using the 3GPP TR 138 901 model

Table 4.2 Mean BPL and BEL for the old residential building for measurements, 3GPP model [92] and the proposed O2I model [11]

Freq. [GHZ]	**Old residential building**				
	Mean BPL [dB]			BEL [dB]	
	Measurement	***3GPP Model***	***Proposed O2I Model***	***Measurement-Proposed O2I model***	***3GPP Model***
27	28.1	23	29.13	22.4	21.5
38	30.4	25.7	31.74	25.6	22.6

Table 4.3 Mean BPL and BEL for the modern office building for measurements, 3GPP model [92] and the proposed O2I model [11]

Freq. [GHz]	**Modern office building**				
	Mean BPL [dB]			BEL [dB]	
	Measurement	***3GPP Model***	***Proposed O2I Model***	***Measurement-Proposed O2I model***	***3GPP Model***
27	24.1	16.3	26.79	20.3	13.1
38	34.5	18.5	36.42	31.6	15.4

[92] and the model proposed in Section 4.3.1 has been carried out and shown in Fig. 4.4 and Fig. 4.5. $\alpha = 2$ has been used in our proposed O2I path-loss model as suggested in [94] for small and mid-size buildings while β has been set equal to 1.6 for the old residential building and equal to 2.5 for the modern office building, for both the considered frequency bands, in agreement with clutter attenuation values found in other measurement campaigns [98] [99]. Since the new model, differently from the 3GPP model, does not include predefined values for BEL, we used the measured BEL values here: this gives some advantage in terms of lower mean error to the proposed model. However, it will not influence the standard deviation of the error, which is the most relevant performance parameter. Figures 4.4 and 4.5 show the variations of BPL at ground floor vs. link distance as the receiver moves along indoor routes as described in Fig. 4.1. In the old residential building (Fig. 4.4), the receiver moves from I1 to I8 and then turns back on the same route from I8 to I1. In the modern office building, the receiver moves from I1 to I4 and then back from I4 to I1. It is clear that the 3GPP model underestimates losses in deep indoor locations (larger distances) while the proposed path-loss model better follows path-loss increase. This can be due to the denser construction of the considered buildings, that have thick partition walls made of bricks, better described by the β parameter of the new model, with respect to the lighted, open-space buildings considered when defining 3GPP model. The average values for the BPL and BEL at 27 and 38 GHz in the first environment are reported in Table 4.2 for all measurements, 3GPP model and the proposed O2I model. These mean values are computed across all routes on both floors to derive a representative figure for the whole building. It is evident that average BEL values

are well reproduced by the 3GPP model in this environment, while average BPL is slightly underestimated. Also, for the considered building, the 3GPP model estimates a mild variation of attenuation with frequency, which is similar to measurements. For what concerns the modern office building (Fig. 4.5) it can be noticed from the graph that the 3GPP model predicts a lower BPL, especially for deep-indoor locations, with an underestimation of as much as 30 dB at about 10m from the outdoor wall, which is also reflected in Table 4.3. Moreover, while the attenuation predicted by the 3GPP model is still mildly dependent on frequency, measurements show a much higher attenuation at 38 GHz with respect to 27 GHz, due to the construction material of this building with metallic structures used in the reinforced concrete and window frames, differently from the residential house considered above.

Finally, in Table 4.4 the mean error and the standard deviation with respect to measured data calculated on both floors of each building are reported at 27 GHz for both the 3GPP model and the suggested O2I model. As can be noticed the proposed O2I model shows smaller error standard deviation values with respect to the 3GPP model, highlighting the greater flexibility and accuracy of the proposed model, using standard literature values for parameter β.

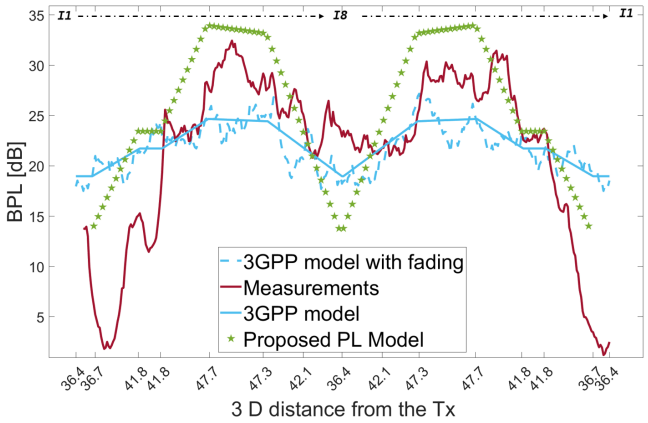

Fig. 4.4 BPL for the old residential building at 27 GHz (ground floor) [11]

4.4.2 Through-Floor Propagation

Propagation through floors is known to be problematic at mm-wave frequencies: here, floor-loss measurements at the 27 and 38 GHz in 5 different kinds of buildings are carried out, with the techniques explained in Section 4.2. Due to the relatively small wavelength, through-floor attenuation depends on the particular microstructure of the floor layer along the Tx-Rx line. In the case of the 17th-century residential building, the initial 30 cm of the

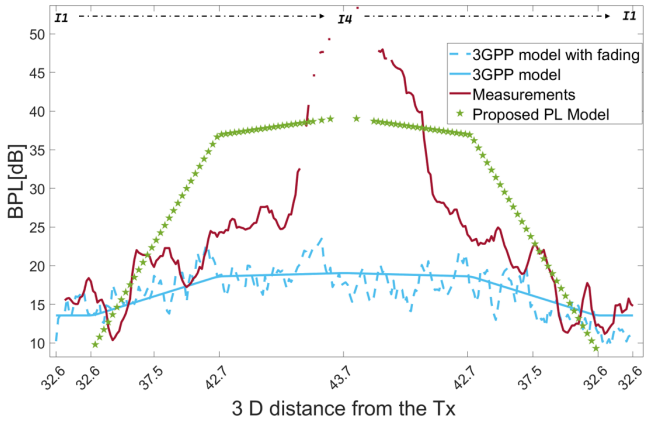

Fig. 4.5 BPL for the modern office building at 27 GHz (ground floor) [11]

Table 4.4 Mean error and standard deviation between measurements and 3GPP model and measurements and the proposed O2I model [11]

Frequency [GHz]	Model-measurement comparison							
	Old residential building				Modern office building			
	3GPP model		Proposed O2I model		3GPP model		Proposed O2I model	
	Mean error [dB]	Error Std. [dB]	Mean error [dB]	Error Std. [dB]	Mean error [dB]	Error Std. [dB]	Mean error [dB]	Error Std. [dB]
27	13.02	6.22	8.95	3.79	18.42	7.67	9.28	4.24

considered scanning length fell under a wooden beam, leading to higher penetration loss in this area as shown in Fig. 4.6a. Furthermore, some variations can be noticed within the same frequency probably caused by irregularities or inconsistencies in floor composition. As expected, through-floor propagation suffers more at 38 GHz as compared to 27 GHz, with a mean attenuation of 49.53 dB and 39.18 dB, respectively, as shown in Table 4.5. Considering the attenuation through the second floor which has an added concrete layer with respect to the first floor, mean attenuation values increase significantly: 62.31 dB at 27 GHz and 80.4 dB at 38 GHz. For a better understanding of the variability of the attenuation through a single floor and thus the need for an evaluation of the mean loss value to be representative of the through floor attenuation, Fig. 4.6a and Fig. 4.6b show the floor scan of both the first and the second floor measurements for the office area of years '30. In Fig. 4.6b, a 2.4 meter scan of the first floor (noted as FF) and second floor (noted as SF) independently is shown while going and coming back. It can be noticed that there is approximately 5 dB of difference in the mean loss between the two floors. Moreover, in both the residential building of 17-th century and the office area of the 1930s, through-floor losses are strongly dependent on the operating frequency. Average losses as well as standard deviation and specific attenuation [dB/cm] are shown in Table 4.5 for all the buildings under consideration. It can be noticed that the

Table 4.5 Summary of penetration losses through one floor [11]

Building type	27 GHz			th	38 GHz		
	$\overline{L}$ [dB]	σ_L [dB]	α_s [dB/cm]	[cm]	$\overline{L}$ [dB]	σ_L [dB]	α_s [dB/cm]
Residential 17-th century (through 1st F)	39.18	5.66	1.78	22	49.53	5.33	2.25
Residential 17-th century (through 2nd F)	62.31	7.92	2.49	24	80.4	4.1	3.22
Hall University building 1930s	77.67	6.93	2.73	28.5	89.88	6.26	3.15
Office area University building 1930s (through 1st F)	61.62	4.26	2.1	30	73.36	2.9	2.45
Office area University building 1930s (through 2nd F)	56.68	8.56	1.89	30	67.18	7.95	2.24
Office area University building 1980s	88.04	5.12	2.52	35	93.95	3.81	2.68
University building 2010	below noise floor			37	below noise floor		

old 17-th century residential building, having floors made of wooden structures, exhibits lower through-floor losses with respect to the newer University buildings. When comparing University buildings of the 1930s and 1980s it can be noticed that through-floor losses are lower for the building of the 1930s, for all the floors considered. However, in the University building of the 1930s, through-floor attenuation depends on the specific part of the building area under consideration, with the hall area having the highest attenuation. The most modern building, dated 2010, with floors equipped with multiple double metallic nets and beams as indicated in Fig.4.7, completely blocks the signal penetration even through only one floor.

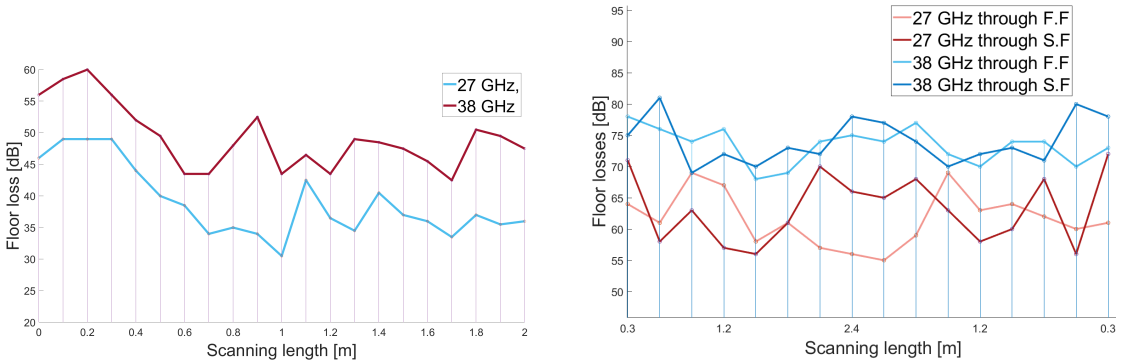

(a) First floor 2m scan : Old residential building

(b) Office area building of the 1930s scan of First Floor (F.F) and Second floor (S.F)

Fig. 4.6 Floor losses versus scanning length [11]

Such a structure becomes of particular interest when interference management is the primary objective. Meanwhile, propagation through two floors is possible in the 17-th century and in some points of the hall of years '30 building, while the received power drops below the receiver sensitivity in modern buildings. Another important observation is that the standard deviation seems to be lower at 38 GHz with respect to 27 GHz in almost all cases. This behaviour is quite peculiar and deserves further investigation. However, the

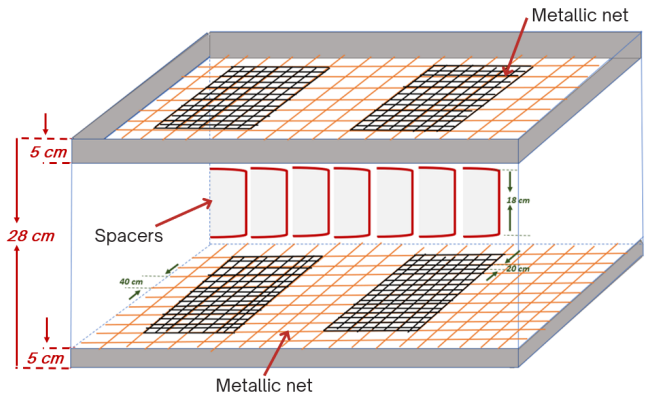

Fig. 4.7 University 2010 : Floor structure [11]

observed general trend is that the more modern the construction technique, the more difficult it is for mm-wave signals to penetrate through floors. Lastly, a blind-test was performed on a new environment (see last picture of Fig. 4.2) that is similar to the Office area of the 1930s University building. By applying the corresponding specific attenuation coefficient proposed in Table 4.5 and considering the floor thickness of 35cm, the new measurement environment shows good agreement between mean attenuation predicted by our through-floor attenuation model ($\overline{L}_{model}$ = 66.1 [dB] at 27 GHz and $\overline{L}_{model}$ = 78.4 [dB] at 38 GHz) and the measured values ($\overline{L}_{meas}$ = 62.3 [dB] at 27 GHz and $\overline{L}_{meas}$ = 73.6 [dB] at 38 GHz), confirming the validity of the proposed model.
This study highlights the need for standard statistical models that can account for through-floor propagation at mm-wave frequencies in different types of buildings of different regions of the world. The proposed Table 4.5 can be further extended by including additional different types of buildings and frequencies carried out with further extensive measurement campaigns. Additional investigations will include the study of the variability range of the considered parameters and, in case, the determination of a general trend.

4.5 Conclusions

O2I and through-floor attenuation are two important mechanisms that become of crucial importance with the recent use of mm-wave frequencies, especially if the focus is on ensuring seamless indoor coverage and interference management. In general, O2I and floor propagation heavily depend on the structural features of buildings and on frequency. In this view, to ensure accurate path loss predictions, a large-scale characterization of the different building types is essential. Furthermore, O2I models proposed by the standardization bodies (ITU/3GPP) seem hardly adaptable to this diversity, while no standard model is currently

available for through-floor propagation. To this aim this study conducts a critical analysis of O2I and through-floor propagation based on multiple measurement campaigns. Comparing O2I measurements with the 3GPP TR 138 901 model, it is observed that the model predicts fairly well the BEL but progressively underestimates BPL as the mobile terminal moves inside the buildings, due to the dense structure of the south-European buildings considered in this study. Moreover, it is highlighted that the frequency dependence of both BEL and BPL is strictly related to the type, thus construction materials, of buildings, with the brick walls of the residential building being weakly frequency dependent, and reinforced concrete being strongly frequency dependent, as for the office building. Overall, this dependence is not taken into account by the 3GPP model, thus there is a requirement for additional measurement campaigns that encompass a wide range of building types, including those found in southern Europe and that can extend the 3GPP model. A simple parametric O2I model based on the formula in [94] is proposed in this work. Results show that the proposed O2I model is able to capture the BPL variations and is more flexible than the 3GPP model.

As for through-floor propagation, having investigated five different buildings, it can be concluded that penetration becomes increasingly difficult with modern and highly insulating construction techniques. Propagation through two floors seems possible only in old buildings with wooden floors. Finally, a first-attempt, simple model formulation for though-floor propagation as a function of the the type of building is proposed in this work.

Chapter 5

Multi-frequency Measurements of Material and Floor Penetration Losses

5.1 Introduction

Indoor communications are of particular interest since the majority of the data traffic nowadays is generated within indoor environments [10]. The introduction of higher frequency bands for various applications in the wireless communication field poses challenges to indoor propagation, especially at mm-wave and sub-THz frequencies where walls, doors, and floors are recognized to heavily hinder the propagation. The strong attenuation due to indoor structures is undesirable when seamless indoor coverage is the primary goal, yet it can have a positive outcome when interference suppression is the main interest.

In order to comprehensively study the signal propagation indoor, an evaluation of how different frequencies interact with various indoor structures should be made [100] [101]. Among common indoor structures, walls and doors play crucial roles. A characterization of frequency-dependent losses exhibited by these structures is fundamental for effective coverage planning. Various measurement campaigns have been reported in the literature regarding the wall and door penetration losses: in [100] for 28 and 140 GHz, in [102] for 73 and 81 GHz, in [103] for 28 and 72 GHz. Nonetheless, a noticeable gap remains in the literature regarding comprehensive studies that consider penetration losses of indoor structures across a wide frequency spectrum encompassing mm-waves to sub-THz frequencies.

Another key mechanism of indoor propagation that is scarcely investigated is the floor penetration loss that heavily depends on the operating frequency and the type of floor under consideration. Notably, the only existing studies belong to low frequency bands as in [104] for 2.4 GHz and [105] for 2.4 and 5.8 GHz. The lack of floor penetration loss knowledge

above 5.8 GHz is reflected in the gap in standardization models such as the ITU-R P.1238-12 recommendation [106], where mean values of floor penetration loss calculated across various buildings are only provided up to 5.8 GHz. Moreover, despite the ongoing research focus on mm-waves and sub-THz frequencies, also the mid-band within 7-24 GHz (known as FR3 band) has gained importance as it has emerged as a possible candidate for early 6G applications. Consequently, a characterization of floor penetration loss within the FR3 band becomes of great importance, thus contributing to international standards.
Therefore, this work addresses the aforementioned gaps in the literature by conducting a measurement campaign to analyze the penetration loss of indoor structures at 25, 77 and 153 GHz and a measurement campaign focused on characterizing floor penetration losses in the FR3 band, specifically within the frequency range from 7.5 to 14.5 GHz.

The O2I penetration loss measurements in Chapter 4 highlighted the significant attenuation faced by mm-Wave signals inside buildings. Expanding upon this, the current chapter extends the analysis across multiple frequency bands to characterize the frequency-dependent penetration loss of different construction materials commonly found in buildings. Understanding these dependencies is crucial when designing RIS-based solutions, as the frequency response of building materials directly influences the optimal placement and tuning of RIS elements. This chapter aims to more accurately bridge measurement-based insights with the RIS modeling techniques presented in earlier chapters.

5.2 Measurement Campaigns

The measurements were conducted in the Department of Engineering at Durham University, UK, built in the 1980s and reconstructed in the 2010s using two different setups as outlined below.

5.2.1 Floor measurements setup

As for floor penetration measurements, three different environments with different floor type inside the Department of Engineering were chosen as can be seen from Figure 5.1. The first environment is the floor of an office area with a thickness of 58 cm where apart from the floor thickness, a 20 cm empty lowered ceiling is present. The second environment is the hall close to stairs with a thickness of 26 cm, while the last environment corresponds to a workshop area with a thickness of 50 cm. Both antennas were installed on tripods designed for measurements and were perfectly aligned vertically on both floors as seen from the schematic representation in Figure 5.2a. The floor penetration losses were measured

using a continuous wave (CW) Gigatronics function generator at the transmitter side and a high-end Keysight spectrum analyser at the receiver side. The transmit power was 15 dBm. Wideband antennas were used for the measurements with the frequency varying from 7.5 to 14.5 GHz : log-periodic antennas were used from 7.5 GHz up to 9 GHz and horn antennas from 10.5 GHz up to 14.5 GHz. The gain of the log-periodic and horn antennas were 6 dBi and 20 dBi respectively. Cable losses of this setup are equal to 6 dB. The floor penetration loss was estimated as the difference between the measured received power and the free space received power, computed through the Friis equation. Generally, floors can be heterogeneous due to construction or pipes passing through them. In order to have a representative figure of the whole floor attenuation, for each environment measurements were repeated 3 times by changing simultaneously the transmitter and receiver along a 1 meter straight line. Furthermore, at each location 8 samples of measurements were recorded, minimizing in this way random fluctuations due to the environment. The mean value and the standard deviation of the floor penetration loss for each environment and for each frequency was then calculated.

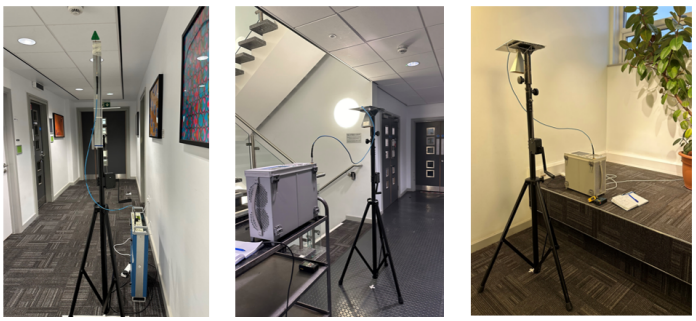

Fig. 5.1 Measurement environment: Hall office area (first), Hall workshop area (second), Hall stairs area (third) [9]

5.2.2 Walls and doors measurements setup

In order to study the impact of indoor structures on signal propagation, a 1.27 cm glass door, a 4.4 cm wooden door, a 16 cm main partition wall between two offices (labeled as wall partition 1) and a 26 cm partitioning wall between two halls (labeled as wall partition 2) were considered as seen from Figure 5.3. In the measurements for the wall penetration loss a custom designed measurement setup to study the impact of precipitation at Durham University was used. The setup uses a programmable phase locked loop (PLL) to generate a CW signal at an intermediate frequency which is then multiplied by 2, 6 and 12 to generate the frequencies at 25.6 GHz, 77 GHz and 153 GHz, respectively. At the receiver side, a similar PLL but with a frequency offset is used to mix with the incoming signals in order to

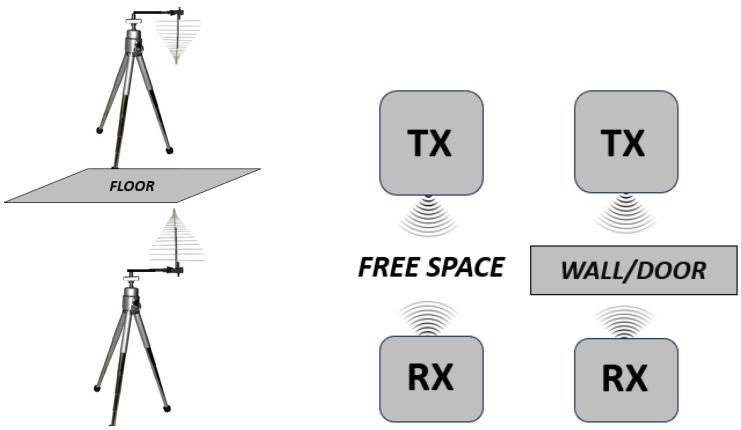

(a) Through floor (b) Wall/door

Fig. 5.2 Schematic setup of measurement campaigns [9]

generate a low frequency beat note at 4 MHz, 12 MHz and 24 MHz respectively. For the present measurements the transmitter and receiver units were set up facing each other, at the same height, and the received signal from the three bands was measured on the Keysight spectrum analyser first without the doors/walls (free space) and then with the walls/doors between the Tx and the Rx, as shown in Figure 2b. To minimize the measurement error, 4 measurements were recorded for each scenario and the mean value was used to estimate the difference between wall/door and free space.

Fig. 5.3 Setup of measurements: Glass door (first), Wooden door (second), Wall partition 1 (third), Wall partition 2 (fourth) [9]

5.3 Results and discussions

5.3.1 Floor penetration loss results

Table 5.2 summarises the results of the evaluated losses as described in Section 5.2.1. It can be noticed that the penetration losses of the "Office area" and the "Workshop area" are quite similar, even though the specific attenuation (evaluated as the mean floor loss divided by the thickness of the floor in cm) is slightly higher for the "Workshop area". As seen from

Table 5.1 Mean penetration and specific attenuation through walls/doors [9]

Frequency [GHz]	**Glass door**		**Wooden door**		**Indoor partition wall (1)**		**Indoor partition wall (2)**	
	Mean loss [dB]	*Specific loss [dB/cm]*	*Mean loss [dB]*	*Specific loss [dB/cm]*	*Mean loss [dB]*	*Specific loss [dB/cm]*	*Mean loss [dB]*	*Specific loss [dB/cm]*
25	4.12	3.24	10.17	2.31	17.39	1.08	26.64	1.02
77	14.08	11.08	21.21	4.82	27.53	1.72	38.40	1.48
153	26.28	20.69	41.97	9.54	53.63	3.35	59.17	2.28

Table 5.2, through-floor losses vary between 44 and 64 dB for the "Office area" and the "Workshop area", for frequencies ranging from 7.5 GHz to 14.5 GHz, while the "Hall Stairs area" exhibits slightly lower losses across all frequencies (from 40 to 58 dB). However, the highest specific attenuation value (1.55 dB/cm at 7.5 GHz and 2.25 dB/cm at 14.5 GHz) is found in the "Hall Stairs area" and this is in agreement with the fact that the stairs are the most solid structure in a building, thus, exhibiting a higher attenuation. In all cases a constant increase of the mean attenuation value with frequency increase is observed (2-3 dB for each 1 GHz increase in frequency). Considering this current trend in mean floor attenuation values, it indicates that in the building under consideration, it is not possible for the signal to propagate through two floors nor for the signal to propagate at mm-wave frequencies, as the value of the corresponding loss would be too high. Furthermore, as it can be seen from Figure 5.4 (different points for one single frequency value) for the "Workshop area" where a 1m scan is performed, the different values for each frequency highlight the presence of small variations in the floor structure. This observation is furthered confirmed by the second location (red dots) which always shows the highest attenuation value while the third location (ciano stars) exhibits the smallest attenuation. However, as frequency approaches 12 GHz, these differences become less evident. For this reason, to account for possible floor unevenness it is advised to take measurement samples in several different locations within the considered environment.

Table 5.2 Floor penetration losses at different environments [9]

Scenario	**Office area**			**Hall Stairs area**			**Workshop area**		
Frequency [GHz]	*Mean loss [dB]*	*Std. [dB]*	*Spec.loss [dB/cm]*	*Mean loss [dB]*	*Std. [dB]*	*Spec.loss [dB/cm]*	*Mean loss [dB]*	*Std. [dB]*	*Spec.loss [dB/cm]*
7.5	44.31	0.223	0.76	40.37	0.161	1.55	44.73	0.785	0.89
8	46.96	0.301	0.81	42.89	0.352	1.65	48.47	0.943	0.97
9	48.97	0.566	0.84	45.92	0.429	1.77	50.15	0.733	1
10.5	53.33	0.343	0.92	47.43	0.332	1.82	54.48	1.152	1.09
12	56.22	0.542	0.97	52.71	0.507	2.03	57.65	1.222	1.15
13	60.88	0.537	1.05	56.21	0.577	2.16	62.20	0.695	1.24
14.5	63.89	0.227	1.1	58.57	0.415	2.25	64.50	0.942	1.29

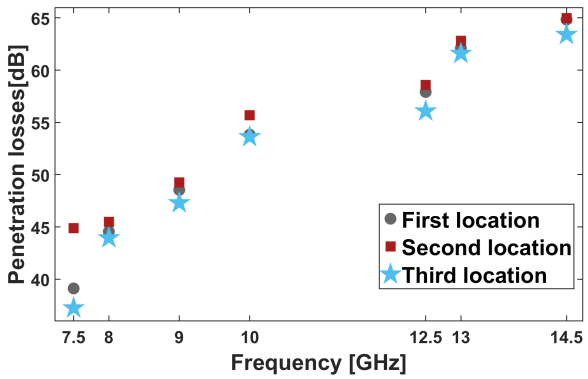

Fig. 5.4 Scanning of Hall Workshop area floor along 3 different locations [9]

5.3.2 Indoor partition losses

The results of the losses across the walls and the doors are summarised in Table 5.1 for the glass door, the wooden door and two partition walls, with wall 1 being the wall between two offices and wall 2 being the wall between two halls. The glass door exhibits smaller mean losses compared to the wooden door and the difference between the two becomes more significant as the frequency increases from 77 to 153 GHz. Yet, the specific attenuation (see Section 5.3.1. for definition) of the glass door is significantly higher than the wooden door. When considering the partition walls, the specific attenuation shows similar values. This characteristic explains the smaller mean loss value of wall 1 which, being thinner than wall 2, exhibits, on average, 8 dB smaller loss than wall 2. Partition wall 1 has a penetration loss of 17.39 dB at 25 GHz which is in good agreement with other measurements such as in [107].

5.4 Concluding remarks

In this study two continuous wave (CW) measurements were carried out aimed at assessing floor penetration loss within the frequency range of 7-15 GHz (FR3 band) and penetration loss through indoor structures at 25, 77, and 153 GHz. Within the FR3 band, losses through floors ranged from 44 to 64 dB across frequencies from 7 GHz to 15 GHz, exhibiting an increase of approximately 18-20 dB for each considered case. The findings in the considered buildings indicate that signal propagation across two floors at millimeter-wave frequencies is impractical, primarily attributed to the significantly high losses. Similarly, indoor partition loss showed a frequency-dependent rise of 22 dB for glass doors and 33 dB for indoor partition walls across the three measured frequency bands. These outcomes underscore the challenge of attaining uninterrupted wireless coverage within indoor spaces, especially at mm-wave frequencies.

Chapter 6

mm-Wave and sub-THz Characterization of various building materials

Index Terms *mm-waves, sub-THz frequencies, building materials, transmission, scattering*

6.1 Introduction

Millimeter wave (mm-wave) and sub-THz communication systems promise high data rates and low latency but face challenges, especially in obstructed indoor environments where most data traffic originates. Effective coverage planning requires understanding how different frequencies interact with various indoor structures and materials. While free-space path loss increases with frequency, the attenuation due to building materials is more complex, with some materials showing low losses even at high frequencies. Understanding the interactions of electromagnetic waves with building materials— transmission, reflection, and scattering—is crucial. These interactions depend on the electromagnetic properties and inner structure of the materials, as well as on surface irregularities and inhomogeneities. Numerous studies have examined indoor and outdoor-to-indoor propagation characteristics, focusing on penetration loss [108, 109], and reflection/scattering up to 300 GHz [110]. However, comprehensive research covering a broad frequency spectrum, including mm-wave and sub-THz frequencies, is scarce. Variations in penetration losses among different concrete blocks, as demonstrated in [111], highlight the need for further measurement campaigns. Building on prior research [11, 112, 113], this study investigates the attenuation characteristics of common building materials at 25.6, 27, 38, 77, 115, 153 and 165 GHz. Using experimental measurements for penetration and reflection loss and a combination of measurements and Ray-Tracing (RT) simulations for scattering, this research aims at providing insights into

material behavior at different frequencies of interest. These findings can support the design and optimization of future communication systems and help calibrate wireless planning simulators. While previous chapters explored penetration loss trends of various building materials, this chapter delves deeper into the scattering properties of construction materials at different frequencies bands. These insights contribute directly to refining the parameters used in the macroscopic and ray-based RIS models (Chapters 2 and 3), ensuring their accuracy in real-world deployments. Ultimately, this chapter supports the broader goal of integrating RIS technology into modern buildings to enhance wireless signal coverage and overcome penetration-related losses. The chapter is organized as follows: Section 6.2 describes the measurement setups for each frequency band, while Section 6.3 presents the results and discussion.

6.2 Measurement setup and methods

Measurements were conducted in Cesena, Italy, and Durham, UK, to analyze diverse construction materials at mm-wave and sub-THz frequencies. The transmitter (TX) and receiver (RX) were consistently aligned at the same height using purpose-built masts and vertically polarized antennas

6.2.1 Mm-Wave measurements

Penetration loss and diffuse scattering measurements from common construction materials-sandstone slab, brick wall, and gypsum board at 27 GHz and 38 GHz. Tx and Rx were horizontally aligned for penetration loss measurements, targeting the material's center with a 0-degree incidence angle. Antennas, TX and RX ends are the ones used in [11]. Penetration loss is then computed as the differential path-loss with and without the Item Under Test (IUT). For scattering measurements, the IUT was illuminated by a TX antenna at a 45° angle to its center. Angle measurements were referenced from the IUT surface: RX was moving on a 140° arc, with locations spaced by 10°. TX-RX distances were chosen to ensure that the -6 dB antenna footprint fell inside the IUT surface, excluding grazing angles (0 to 20° and 160 to 180°).

6.2.2 sub-THz measurements

Measurements at sub-THz frequencies were conducted both in UK and Italy. The first set of penetration measurements was conducted in the UK using a custom-designed setup described in [112] at 25.6, 77 and 153 GHz. Initial measurements focused on building-integrated

materials like glass doors, wooden doors, and partition walls within offices and halls. Additionally, various out-of-structure materials such as MDF, wood flooring, gypsum plasterboard, plexiglass, plywood, single glass, and double-glazed glass were measured. Measurements were conducted with a consistent distance between TX and RX, with integrated materials naturally aligned, and out-of-structure materials positioned using an aligned frame. Subsequent measurements of scattering in the sub-THz band (110-170 GHz) were carried out in Italy with a Keysight Vector Network Analyzer combined with extenders to reach the desired frequencies. Gypsum board wall and brick wall were used as samples. Both penetration and scattering measurements were conducted following the descriptions as in section 6.2.1.

6.3 Results and discussion

6.3.1 Transmission loss measurements

After averaging five measurements with slightly varied incidence points to mitigate multipath fading effects, the transmission (or insertion) loss results for normal incidence together with specific attenuation (attenuation for 1 cm) across different frequencies were determined as shown in Table 6.1. Furthermore, the transmission loss of gypsum board was also measured at the sub-THz band, with results of 14 dB at 115 GHz and 23 dB at 165 GHz. However, the transmission loss of the brick wall at these frequencies could not be calculated due to the noise level of the VNA, but it is estimated to be above 35 dB.

Table 6.1 Mean penetration loss and specific attenuation at sub-THz

Material	25.6 GHz		77 GHz		153 GHz	
	Mean loss [dB]	*Specific atten. [dB/cm]*	*Mean loss [dB]*	*Specific atten. [dB/cm]*	*Mean loss [dB]*	*Specific atten. [dB/cm]*
Glass door	4.12	3.24	14.08	11.08	26.28	20.69
Wooden Door	10.17	2.31	21.21	4.82	41.97	9.54
Indoor partition wall (1)	17.39	1.08	27.53	1.72	53.63	3.35
Indoor partition wall (2)	26.64	1.02	38.50	1.48	59.17	2.28
Plexiglass	0.12	0.3	0.71	1.78	1.14	2.85
Gypsum plasterboard	1.06	0.82	1.28	0.98	1.41	1.08
MDF	1.98	1.65	5.43	4.53	7.25	6.04
Wood flooring	4.02	2.87	7.23	5.16	11.26	8.04
Single glass	1.49	3.73	4.06	10.15	5.96	14.9
Plywood	1.35	4.5	2.73	9.1	4.64	15.46
Double glazed glass	13.17	9.41	18.65	13.32	23.06	16.47

6.3.2 Diffuse scattering measurements

Non-specular reflection from IUT due to surface roughness or internal irregularities was measured, and results were used to tune the Effective Roughness (ER) scattering model [113]. In the ER model the intensity of scattered field is proportional to the scattering parameter S, and the scattering pattern has 2 lobes centered on the specular reflection and

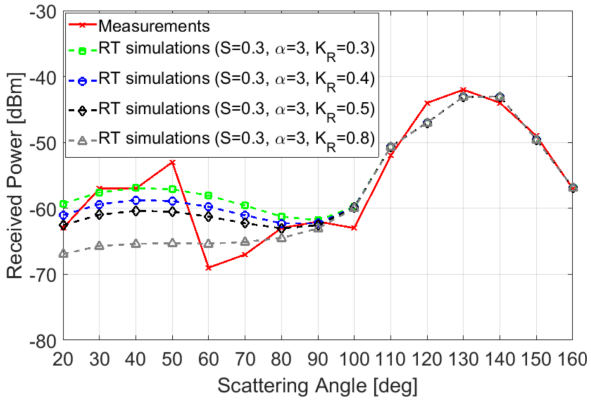

Fig. 6.1 Brick wall sample: measurement vs simulation comparison for different value of the K_R parameter at 27 GHz.

Table 6.2 Scattering parameters at 27 GHz and 140 GHz for Brick-Wall and Gypsum Board.

Material	**27 GHz**			**140 GHz**		
	Best-fit S	**Best-fit** K_R	**Best-fit** α_R	**Best-fit** S	**Best-fit** K_R	**Best-fit** α_R
Brick wall	0.3	0.5	3	0.5	1	3
Gypsum board wall	0.4	0.3	3	0.6	1	3

back-scattering direction, respectively. The lobe widths are set by the parameters (α_R, α_i) while K_R represents the power-repartition between the lobes. At sub-THz frequencies, due to vanishing penetration $K_R = 1$, i.e. the double-lobe scattering pattern becomes a single-lobe around specular reflection. More details can be found in [113]. The ER model was calibrated using RT simulations that replicated the measurement setup: ER scattering model was parametrized to achieve the best match with measurements. At 27 GHz, strong back-scattering is observed in brick and gypsum materials at Rx locations far from specular reflection, likely due to internal structures (see Fig. 6.1). The double-lobe scattering pattern is most accurate for these materials, with the ER model parameters calibrated to match measurements. The angular amplitude of the lobes is fixed at $\alpha_R = \alpha_i = 3$, for optimization simplicity. The best-fit parameters K_R and S are shown in Table 2 for brick-wall and for gypsum board at different frequencies (i.e. 27 GHz and 140 GHz). The results show that for both materials S is higher for gypsum board than brick wall, this can be attributed to the relevant internal inhomogeneities that characterize the former.

Conclusion

The research conducted during this PhD has explored the intersection between modern construction advancements and the increasing requirements of next-generation wireless networks, introducing RIS as a promising technology for addressing high-frequency signal propagation issues. By incorporating RIS directly into structural elements like building walls, this approach offers a dynamic and efficient solution for controlling electromagnetic waves, thus enhancing both indoor and outdoor wireless coverage in ways that align with contemporary building designs.

A core contribution of this thesis is the creation of simple macroscopic models to accurately capture the behavior of RIS while being physically consistent. As a first step, a parametric model based on power balance at each RIS elements was developed and later a ray-based macroscopic model designed to simulate re-radiated wave behavior in environments equipped with reflective RIS was introduced. The latter was thoroughly validated against established physical optics techniques, demonstrating a reliable balance between accuracy and computational efficiency, making it highly applicable for practical use in Ray Tracing software for complex urban environments. Additionally, experimental analyses across mm-wave and sub-THz bands revealed notable signal attenuation through common building materials, which emphasizes the importance of deploying intelligent surfaces to mitigate these losses and improve connectivity.

By aligning the evolving needs of wireless communication with construction innovations, this work suggests that RIS could play a pivotal role in the future of smart city infrastructure. Beyond solving high-frequency signal challenges, this framework enables the seamless integration of communication systems within building structures, laying the groundwork for a new era of interconnected urban spaces.

Future prospects

Despite the advancements in integrating Reconfigurable Intelligent Surfaces into wireless networks, several challenges remain. How can these surfaces be dynamically optimized in real-time to adapt to changing propagation conditions in complex indoor and urban environments? What are the most efficient methodologies for modeling and mitigating multi-path interference in large-scale RIS deployments? Additionally, how can RIS be seamlessly co-designed with emerging sustainable construction materials to enhance signal penetration while maintaining architectural and energy efficiency goals?

Beyond these integration challenges, fundamental modeling issues persist and require further investigation. First, the macroscopic model described in Chapter 3 must be extended to account for the transmission mode of RIS (forward half-space), which is particularly important for O2I propagation. Furthermore, both the macroscopic and ray-based models presented in Chapters 2 and 3 require experimental validation to confirm their real-world applicability. However, it is important to note that the validity of the proposed models is not constrained by manufacturing imperfections or design challenges, as these are inherently incorporated into the macroscopic parameters that give the RIS efficiency. Furthermore, these proposed RIS models are able to account for multipath effects by reapplying the formulation for each incident path and summing the results through the superposition of effects.

Finally, integrating RIS into building structures also depends on the electro-magnetic characterization of construction materials themselves. Future studies should aim to generalize the findings presented in this thesis by expanding measurements to a broader range of materials used in different geographical regions, considering varying environmental conditions (e.g., temperature and humidity) and diverse construction methods. Addressing these challenges will be essential for ensuring the practical feasibility and widespread adoption of RIS in future wireless networks.

References

[1] S. Kang, M. Mezzavilla, S. Rangan, A. Madanayake, S. B. Venkatakrishnan, G. Hellbourg, M. Ghosh, H. Rahmani, and A. Dhananjay, "Cellular wireless networks in the upper mid-band," *IEEE Open Journal of the Communications Society*, vol. 5, pp. 2058–2075, 2024.

[2] A. A. Ayeni, A. A. Yusuf, and S. O. Onidare, "Correlation between the electromagnetic properties of building materials and wireless signal penetration loss," *IEEE Transactions on Antennas and Propagation*, vol. 70, no. 12, pp. 12040–12048, 2022.

[3] I. T. U. ITU-R, Rec. ITU-R P.2040-2, "Effects of building materials and structures on radiowave propagation above about 100 MHz," Sept. 2021.

[4] J. L. Towers, S. Salous, X. Raimundo, and A. Cheema, "Building entry loss for traditional and thermally efficient houses between 0.4 and 73 GHz," in *12th European Conference on Antennas and Propagation (EuCAP 2018)*, pp. 1–4, 2018.

[5] S. M. Yee Aung and M. M. Maw, "Analysis of indoor channel propagation characteristics in multifloored building at 2.4 GHz," in *2017 21st International Computer Science and Engineering Conference (ICSEC)*, pp. 1–5, 2017.

[6] M. Sasaki, M. Inomata, W. Yamada, N. Kita, T. Onizawa, M. Nakatsugawa, K. Kitao, and T. Imai, "Path loss characteristics between different floors from 0.8 to 37 ghz in indoor office environments," in *2016 International Symposium on Antennas and Propagation (ISAP)*, pp. 66–67, 2016.

[7] A. C. M. Austin, M. J. Neve, and G. B. Rowe, "Modelling inter-floor radio-wave propagation in office buildings," in *2008 IEEE Antennas and Propagation Society International Symposium*, pp. 1–4, 2008.

[8] "Ericson report: Demand for indoor connectivity driving the need for enhanced performance." https://www.ericsson.com/en/reports-and-papers/mobility-report/articles/mobile-broadband-indoor-deployment. Accesed on October 2024.

[9] S. Kodra, J. Hu, M. Barbiroli, V. Degli-Esposti, and S. Salous, "Multi-frequency measurements of material and floor penetration losses," in *4th URSI Atlantic RadioScience Conference*, 2024.

[10] Z. Li, H. Hu, J. Zhang, and J. Zhang, "Impact of wall penetration loss on indoor wireless networks," *IEEE Antennas and Wireless Propagation Letters*, vol. 20, no. 10, pp. 1888–1892, 2021.

[11] S. Kodra, M. Barbiroli, E. M. Vitucci, F. Fuschini, and V. Degli-Esposti, "Mm-wave building penetration losses: A measurement-based critical analysis," *IEEE Open Journal of Antennas and Propagation*, vol. 5, no. 2, pp. 404–413, 2024.

[12] F. Firyaguna, J. Kibilda, C. Galiotto, and N. Marchetti, "Performance analysis of indoor mmwave networks with ceiling-mounted access points," *IEEE Transactions on Mobile Computing*, vol. 20, no. 5, pp. 1940–1950, 2021.

[13] A. Schumacher, R. Merz, and A. Burg, "A mmwave bridge concept to solve the cellular outdoor-to-indoor challenge," in *2020 IEEE 91st Vehicular Technology Conference (VTC2020-Spring)*, pp. 1–6, 2020.

[14] D. Liu, W. Hong, T. S. Rappaport, C. Luxey, and W. Hong, "What will 5g antennas and propagation be?," *IEEE Transactions on Antennas and Propagation*, vol. 65, no. 12, pp. 6205–6212, 2017.

[15] H. Chen, H. Chen, X. Xiu, Q. Xue, and W. Che, "Transparent fss on glass window for signal selection of 5g millimeter-wave communication," *IEEE Antennas and Wireless Propagation Letters*, vol. 20, no. 12, pp. 2319–2323, 2021.

[16] L. Vähä-Savo, A. G. Atienza, C. Cziezerski, M. Heino, K. Haneda, C. Icheln, X. Lü, and K. Viljanen, "Passive antenna systems embedded into a load bearing wall for improved radio transparency," in *2020 50th European Microwave Conference (EuMC)*, pp. 424–427, 2021.

[17] L. Vähä-Savo, K. Haneda, C. Icheln, and X. Lü, "Electromagnetic–thermal analyses of distributed antennas embedded into a load-bearing wall," *IEEE Transactions on Antennas and Propagation*, vol. 71, no. 8, pp. 6849–6858, 2023.

[18] Q. Wu, S. Zhang, B. Zheng, C. You, and R. Zhang, "Intelligent reflecting surface-aided wireless communications: A tutorial," *IEEE Transactions on Communications*, vol. 69, no. 5, pp. 3313–3351, 2021.

[19] M. Di Renzo, A. Zappone, M. Debbah, M.-S. Alouini, C. Yuen, J. de Rosny, and S. Tretyakov, "Smart radio environments empowered by reconfigurable intelligent surfaces: How it works, state of research, and the road ahead," *IEEE J. Sel. Areas Commun.*, vol. 38, no. 11, pp. 2450–2525, 2020.

[20] Z. Fu, X. Zou, Y. Liao, G. Lai, Y. Li, and K. L. Chung, "A brief review and comparison between transmitarray antennas, reflectarray antennas and reconfigurable intelligent surfaces," in *2022 IEEE Conference on Telecommunications, Optics and Computer Science (TOCS)*, pp. 1192–1196, 2022.

[21] M. Di Renzo, F. H. Danufane, and S. Tretyakov, "Communication models for reconfigurable intelligent surfaces: From surface electromagnetics to wireless networks optimization," *Proc. IEEE*, vol. 110, no. 9, pp. 1164–1209, 2022.

[22] M. Jian, G. C. Alexandropoulos, E. Basar, C. Huang, R. Liu, Y. Liu, and C. Yuen, "Reconfigurable intelligent surfaces for wireless communications: Overview of hardware designs, channel models, and estimation techniques," *Intelligent and Converged Networks*, vol. 3, no. 1, pp. 1–32, 2022.

[23] S. Kodra, S. Del Prete, E. Bernardi, F. Fuschini, M. Barbiroli, E. M. Vitucci, and V. Degli-Esposti, "On transmissive ris for mm-waves outdoor-to-indoor coverage enhancement," in *2025 19th European Conference on Antennas and Propagation (EuCAP)*, 2025. to appear.

[24] J. C. Maxwell, *A treatise on electricity and magnetism*. Clarendon Press, 1881.

[25] W. W. Skeat, *The Concise Dictionary of English Etymology*. Wordsworth Editions, 1993.

[26] V. Veselago, "About properties of substances with simultaneously negative values of dielectric and magnetic permeabilities," *Soviet Phys.-Solid State*, vol. 8, p. 2853, 1967.

[27] J. B. Pendry, "Negative refraction makes a perfect lens," *Phys. Rev. Lett.*, vol. 85, pp. 3966–3969, Oct 2000.

[28] C. L. Holloway, A. Dienstfrey, E. F. Kuester, J. F. O'Hara, A. K. Azad, and A. J. Taylor, "Characterization of a metafilm/metasurface," in *2009 IEEE Antennas and Propagation Society International Symposium*, pp. 1–3, 2009.

[29] C. Simovski and S. Tretyakov, *An Introduction to Metamaterials and Nanophotonics*. Cambridge University Press, 2020.

[30] S. Zeng, H. Zhang, B. Di, Y. Tan, Z. Han, H. V. Poor, and L. Song, "Reconfigurable intelligent surfaces in 6G: Reflective, transmissive, or both?," *IEEE Communications Letters*, vol. 25, no. 6, pp. 2063–2067, 2021.

[31] W. Tang, M. Z. Chen, X. Chen, J. Y. Dai, Y. Han, M. Di Renzo, Y. Zeng, S. Jin, Q. Cheng, and T. J. Cui, "Wireless communications with reconfigurable intelligent surface: Path loss modeling and experimental measurement," *IEEE Trans. Wireless Commun.*, vol. 20, no. 1, pp. 421–439, 2021.

[32] J. Tang, M. Cui, S. Xu, L. Dai, F. Yang, and M. Li, "Transmissive ris for b5g communications: Design, prototyping, and experimental demonstrations," *IEEE Transactions on Communications*, vol. 71, no. 11, pp. 6605–6615, 2023.

[33] K. Goto, S. Suyama, T. Yamada, K. Arai, and O. Kagaya, "Experimental trials with combination of multiple transmissive metasurfaces and beamforming for mmw coverage enhancement," in *2023 IEEE 98th Vehicular Technology Conference (VTC2023-Fall)*, pp. 1–5, 2023.

[34] S. Danesh, A. Bagheri, and M. Khalily, "Wide-incidence angle and polarisation insensitive transparent metasurface for 5g outdoor to indoor coverage enhancement," in *2022 IEEE International Symposium on Antennas and Propagation and USNC-URSI Radio Science Meeting (AP-S/URSI)*, pp. 239–240, 2022.

[35] D. E. S. Rene Descartes and M. L. Latham, *The Geometry of Rene Descartes (Dover Books on Mathematics*. Kessinger Publishing, 2010.

[36] A. Diaz-Rubio, V. Asadchy, A. Elsakka, and S. Tretyakov, "From the generalized reflection law to the realization of perfect anomalous reflectors," *Sci. Adv.*, vol. 3, no. 8, pp. 1–10, 2017.

[37] M. Merluzzi and A. Clemente, "Anomalous and specular reflections of reconfigurable intelligent surfaces: Configuration strategies and system performance," *IEEE Wireless Communications Letters*, vol. 13, no. 10, pp. 2707–2711, 2024.

[38] T. J. Cui, M. Q. Qi, X. Wan, J. Zhao, and Q. Cheng, "Coding metamaterials, digital metamaterials and programmable metamaterials," *Light Sci Appl*, vol. 3, 2014.

[39] L. Li, T. J. Cui, W. Ji, S. Liu, J. Ding, X. Wan, Y. B. Li, M. Jiang, C.-W. Qiu, and S. Zhang, "Electromagnetic reprogrammable coding-metasurface holograms," *Nature Communication*, vol. 8, 2017.

[40] V. S. A. Shaltout, A. Kildishev, "Evolution of photonic metasurfaces: from static to dynamic," *Journal of the Optical Society of America*, vol. 33, pp. 501–510, 2016.

[41] E. Basar, M. Di Renzo, J. De Rosny, M. Debbah, M.-S. Alouini, and R. Zhang, "Wireless communications through reconfigurable intelligent surfaces," *IEEE Access*, vol. 7, pp. 116753–116773, 2019.

[42] Q. Wu and R. Zhang, "Towards smart and reconfigurable environment: Intelligent reflecting surface aided wireless network," *IEEE Communications Magazine*, vol. 58, no. 1, pp. 106–112, 2020.

[43] E. Bjornson, O. T. Demir, and L. Sanguinetti, "A primer on near-field beamforming for arrays and reconfigurable intelligent surfaces," in *2021 55th Asilomar Conference on Signals, Systems, and Computers*, pp. 105–112, 2021.

[44] C. Liaskos, S. Nie, A. Tsioliaridou, A. Pitsillides, S. Ioannidis, and I. Akyildiz, "A new wireless communication paradigm through software-controlled metasurfaces," *IEEE Communications Magazine*, vol. 56, no. 9, pp. 162–169, 2018.

[45] T. S. Rappaport, Y. Xing, G. R. MacCartney, A. F. Molisch, E. Mellios, and J. Zhang, "Overview of millimeter wave communications for fifth-generation (5g) wireless networks—with a focus on propagation models," *IEEE Transactions on Antennas and Propagation*, vol. 65, no. 12, pp. 6213–6230, 2017.

[46] A. I. Vistnes, *Physics of Oscillations and Waves*. Springer Nature, 2018.

[47] A. Díaz-Rubio and S. A. Tretyakov, "Macroscopic modeling of anomalously reflecting metasurfaces: Angular response and far-field scattering," *IEEE Trans. Antennas Propag.*, vol. 69, no. 10, pp. 6560–6571, 2021.

[48] Y. L. C. de Jong, "Uniform ray description of physical optics scattering by finite locally periodic metasurfaces," *IEEE Trans. Antennas Propag.*, vol. 70, no. 4, pp. 2949–2959, 2022.

[49] V. Degli-Esposti, E. M. Vitucci, M. D. Renzo, and S. A. Tretyakov, "Reradiation and scattering from a reconfigurable intelligent surface: A general macroscopic model," *IEEE Trans. Antennas Propag.*, vol. 70, no. 10, pp. 8691–8706, 2022.

[50] S. Kodra, E. M. Vitucci, M. Barbiroli, M. Albani, and V. Degli-Esposti, "A macroscopic bilateral modeling approach for reflective and transmissive metasurfaces," in *2024 18th European Conference on Antennas and Propagation (EuCAP)*, pp. 1–4, 2024.

[51] E. M. Vitucci, M. Albani, S. Kodra, M. Barbiroli, and V. Degli-Esposti, "An Efficient Ray-Based Modeling Approach for Scattering from Reconfigurable Intelligent Surfaces.," *IEEE Trans. Antennas Propag.*, vol. 72, pp. 1–13, 2024.

[52] J. Tang, M. Cui, S. Xu, L. Dai, F. Yang, and M. Li, "Transmissive RIS for B5G communications: Design, prototyping, and experimental demonstrations," *IEEE Transactions on Communications*, pp. 1–1, 2023.

[53] D. Kitayama, Y. Hama, K. Goto, K. Miyachi, T. Motegi, and O. Kagaya, "Transparent dynamic metasurface for a visually unaffected reconfigurable intelligent surface: controlling transmission/reflection and making a window into an RF lens," *Opt. Express*, vol. 29, pp. 29292–29307, Aug 2021.

[54] J. L. Wu, Y. M. Pan, and S. Y. Zheng, "Design of single-layer polarization-dependent transmissive and reflective focusing metasurface," *IEEE Transactions on Antennas and Propagation*, vol. 69, no. 11, pp. 7637–7646, 2021.

[55] S. Liu, Z. Ma, J. Pei, Q. Jiao, L. Yang, W. Zhang, H. Li, Y. Li, Y. Zou, and X. Tan, "A review of anomalous refractive and reflective metasurfaces," *Nanotechnology and Precision Engineering (NPE)*, vol. 5, p. 025001, 04 2022.

[56] L.-X. Wu, N. Zhang, K. Qu, K. Chen, T. Jiang, J. Zhao, and Y. Feng, "Transmissive metasurface with independent amplitude/phase control and its application to low-side-lobe metalens antenna," *IEEE Transactions on Antennas and Propagation*, vol. 70, no. 8, pp. 6526–6536, 2022.

[57] F. Fuschini, V. Degli-Esposti, and E. M. Vitucci, "A model for forward-diffuse scattering through a wall," in *Proceedings of the Fourth European Conference on Antennas and Propagation*, pp. 1–4, 2010.

[58] J. Huang, C.-X. Wang, Y. Sun, R. Feng, J. Huang, B. Guo, Z. Zhong, and T. J. Cui, "Reconfigurable intelligent surfaces: Channel characterization and modeling," *Proc. IEEE*, vol. 110, no. 9, pp. 1290–1311, 2022.

[59] E. Basar, I. Yildirim, and F. Kilinc, "Indoor and outdoor physical channel modeling and efficient positioning for reconfigurable intelligent surfaces in mmwave bands," *IEEE Trans. Commun.*, vol. 69, no. 12, pp. 8600–8611, 2021.

[60] Z. Lian, Y. Su, Y. Wang, and L. Jiang, "A non-stationary 3-D wideband channel model for intelligent reflecting surface-assisted HAP-MIMO communication systems," *IEEE Trans. Veh. Technol.*, vol. 71, no. 2, pp. 1109–1123, 2022.

[61] Y. Liu and C. D. Sarris, "Efficient propagation modeling for communication channels with reconfigurable intelligent surfaces," *IEEE Antennas Wireless Propag. Lett.*, vol. 21, no. 10, pp. 2120–2124, 2022.

[62] J. Budhu and A. Grbic, "Perfectly reflecting metasurface reflectarrays: Mutual coupling modeling between unique elements through homogenization," *IEEE Trans. Antennas Propag.*, vol. 69, no. 1, pp. 122–134, 2021.

[63] F. H. Danufane, M. D. Renzo, J. de Rosny, and S. Tretyakov, "On the path-loss of reconfigurable intelligent surfaces: An approach based on green's theorem applied to vector fields," *IEEE Trans. Commun.*, vol. 69, no. 8, pp. 5573–5592, 2021.

[64] S. Stewart, Y. L. C. de Jong, T. J. Smy, and S. Gupta, "Ray-optical evaluation of scattering from electrically large metasurfaces characterized by locally periodic surface susceptibilities," *IEEE Trans. Antennas Propag.*, vol. 70, no. 2, pp. 1265–1278, 2022.

[65] J. S. Lu, E. M. Vitucci, V. Degli-Esposti, F. Fuschini, M. Barbiroli, J. A. Blaha, and H. L. Bertoni, "A discrete environment-driven GPU-based ray launching algorithm," *IEEE Trans. Antennas Propag.*, vol. 67, no. 2, pp. 1180–1192, 2019.

[66] L. Felsen and N. Marcuvitz, *Radiation and Scattering of Waves*. IEEE Press Series on Electromagnetic Wave Theory, Wiley, 1994.

[67] J. B. Keller, "Geometrical theory of diffraction.," *J. Opt. Soc. Am.*, vol. 52, pp. 116–30, 1962.

[68] R. Kouyoumjian and P. Pathack, "A uniform geometrical theory of diffraction for an edge in a perfectly conducting surface," *Proc. IEEE*, vol. 62, no. 11, pp. 1448–1461, 1974.

[69] E. M. Vitucci, J. S. Lu, S. Gordon, J. J. Zhu, and V. Degli-Esposti, "Discrete environment-driven GPU-based ray launching: validation and applications," *Electronics*, vol. 10, no. 21, 2021.

[70] G. Deschamps, "Ray techniques in electromagnetics," *Proc. IEEE*, vol. 60, no. 9, pp. 1022–1035, 1972.

[71] G. L. James, *Geometrical Theory of Diffraction for Electromagnetic Waves*. IEE electromagnetic waves series, P. Peregrinus, 1986.

[72] I. Kay and J. B. Keller, "Asymptotic evaluation of the field at a caustic," *J. Appl. Phys.*, vol. 25, no. 7, pp. 876–883, 1954.

[73] C. A. Balanis, *Advanced engineering electromagnetics*. John Wiley & Sons, 2012.

[74] F. Yang and Y. Rahmat-Samii, *Surface Electromagnetics: With Applications in Antenna, Microwave, and Optical Engineering*. Cambridge University Press, 2019.

[75] M. Albani, G. Carluccio, and P. H. Pathak, "Uniform ray description for the PO scattering by vertices in curved surface with curvilinear edges and relatively general boundary conditions," *IEEE Trans. Antennas Propag.*, vol. 59, no. 5, pp. 1587–1596, 2011.

[76] R. Luebbers, "Finite conductivity uniform GTD versus knife edge diffraction in prediction of propagation path loss," *IEEE Trans. Antennas Propag.*, vol. 32, no. 1, pp. 70–76, 1984.

[77] P. Holm, "A new heuristic UTD diffraction coefficient for nonperfectly conducting wedges," *IEEE Trans. Antennas Propag.*, vol. 48, no. 8, pp. 1211–1219, 2000.

[78] D. McNamara, C. Pistorius, and J. Malherbe, *Introduction to the Geometrical Theory of Diffraction*. Artech house, 1990.

[79] F. Capolino, M. Albani, S. Maci, and S. Felsen, "Frequency-domain green's function for a planar periodic semi-infinite phased array. ii. diffracted wave phenomenology," *IEEE Trans. Antennas Propag.*, vol. 48, no. 1, pp. 75–85, 2000.

[80] G. Buttazzoni and R. Vescovo, "Density tapering of linear arrays radiating pencil beams: A new extremely fast gaussian approach," *IEEE Trans. Antennas Propag.*, vol. 65, no. 12, pp. 7372–7377, 2017.

[81] O. Svelto, *Principles of Lasers*. Springer US, 2012.

[82] A. A. Ayeni, A. A. Yusuf, and S. O. Onidare, "Correlation between the electromagnetic properties of building materials and wireless signal penetration loss," *IEEE Transactions on Antennas and Propagation*, vol. 70, no. 12, pp. 12040–12048, 2022.

[83] Y. C. Lee, S.-S. Oh, H. C. Lee, C. Woo Byeon, S. W. Park, I.-Y. Lee, J.-H. Lim, J.-I. Lee, and B.-L. Cho, "Measurements of window penetration loss and building entry loss from 3.5 to 24 GHz," in *2019 13th European Conference on Antennas and Propagation (EuCAP)*, pp. 1–4, 2019.

[84] S. Y. Jun, D. Caudill, J. Chuang, P. B. Papazian, A. Bodi, C. Gentile, J. Senic, and N. Golmie, "Penetration loss at 60 GHz for indoor-to-indoor and outdoor-to-indoor mobile scenarios," in *2020 14th European Conference on Antennas and Propagation (EuCAP)*, pp. 1–5, 2020.

[85] M. Mohsen and D. W. Matolak, "31 GHz path loss measurement and modeling for indoor/outdoor environments," in *2018 Wireless Telecommunications Symposium (WTS)*, pp. 1–8, 2018.

[86] C. L. Zhimeng Zhong, Jianyao Zhao, "Outdoor-to-indoor channel measurement and coverage analysis for 5g typical spectrums," in *International Journal of Antennas and Propagation*, vol. 2019, pp. 1–10, 2019.

[87] J. Du, D. Chizhik, R. Feick, G. Castro, M. Rodríguez, and R. A. Valenzuela, "Suburban residential building penetration loss at 28 ghz for fixed wireless access," in *IEEE Wireless Communications Letters*, vol. 7, pp. 890–893, 2018.

[88] M. Khatun, C. Guo, D. Matolak, and H. Mehrpouyan, "Indoor and outdoor penetration loss measurements at 73 and 81 GHz," in *2019 IEEE Global Communications Conference (GLOBECOM)*, pp. 1–5, 2019.

[89] W. Yang, J. Huang, J. Zhang, Y. Gao, S. Salous, and J. Zhang, "Measurements of reflection and penetration loss in indoor environments in the 39-ghz band," in *2021 15th European Conference on Antennas and Propagation (EuCAP)*, pp. 1–5, 2021.

[90] S. Salous, B. M. Villacieros, and J. Bishop, "Building entry loss and clutter loss at 26 GHz," in *2020 14th European Conference on Antennas and Propagation (EuCAP)*, pp. 1–4, 2020.

[91] M. Sasaki, M. Inomata, W. Yamada, N. Kita, T. Onizawa, M. Nakatsugawa, K. Kitao, and T. Imai, "Path loss characteristics between different floors from 0.8 to 37 GHz in indoor office environments," in *2016 International Symposium on Antennas and Propagation (ISAP)*, pp. 66–67, 2016.

[92] 3GPP, "5g; study on channel model for frequencies from 0.5 to 100 ghz (3gpp tr 38.901 version 16.1.0 release 16)," Tech. Rep. TR 138 901 V16.1.0 (2020-11)", 3GPP, 2020.

[93] F. Fuschini, M. Barbiroli, E. Vitucci, and V. Degli-Esposti, "Multi-band outdoor-to-indoor propagation measurements using a drone," in *2022 16th European Conference on Antennas and Propagation (EuCAP)*, pp. 1–4, 2022.

[94] V. Degli-Esposti, G. Falciasecca, F. Fuschini, and E. M. Vitucci, "A meaningful indoor path-loss formula," *IEEE Antennas and Wireless Propagation Letters*, vol. 12, pp. 872–875, 2013.

[95] "Signal generator website." https://spectrumcompact.com/. Accesed on October 2024.

[96] "Spectrum analyzer website." https://www.saftehnika.com/en/ebandspectrumcompact. Accesed on October 2024.

[97] L. Possenti, J. Pascual-García, V. Degli-Esposti, A. Lozano-Guerrero, M. Barbiroli, M. T. Martinez-Inglés, F. Fuschini, J. V. Rodríguez, E. M. Vitucci, and J. M. Molina-García-Pardo, "Improved fabry-pérot electromagnetic material characterization: Application and results," *Radio Science*, vol. 55, no. 11, pp. 1–15, 2020.

[98] K. Du, O. Ozdemir, F. Erden, and I. Guvenc, "Sub-terahertz and mmwave penetration loss measurements for indoor environments," in *2021 IEEE International Conference on Communications Workshops (ICC Workshops)*, pp. 1–6, 2021.

[99] N. Hosseini, M. Khatun, C. Guo, K. Du, O. Ozdemir, D. W. Matolak, I. Guvenc, and H. Mehrpouyan, "Attenuation of several common building materials: Millimeter-wave frequency bands 28, 73, and 91 ghz," *IEEE Antennas and Propagation Magazine*, vol. 63, no. 6, pp. 40–50, 2021.

[100] B.-E. Olsson, C. Larsson, M. N. Johansson, and S. L. H. Nguyen, "Radio propagation in an office environment at 140 ghz and 28 ghz," in *2021 15th European Conference on Antennas and Propagation (EuCAP)*, pp. 1–5, 2021.

[101] Y. C. Lee, S.-S. Oh, C. W. Byeon, K. Aziding, and B.-L. Cho, "Impact of window penetration loss on building entry loss from 3.5 to 24 ghz," *IEEE Access*, vol. 9, pp. 138571–138579, 2021.

[102] M. Khatun, C. Guo, D. Matolak, and H. Mehrpouyan, "Indoor and outdoor penetration loss measurements at 73 and 81 ghz," in *2019 IEEE Global Communications Conference (GLOBECOM)*, pp. 1–5, 2019.

[103] G. Barb, F. Danuti, M. A. Ouamri, and M. Otesteanu, "Analysis of vegetation and penetration losses in 5g mmwave communication systems," in *2022 International Symposium on Electronics and Telecommunications (ISETC)*, pp. 1–5, 2022.

[104] S. M. Yee Aung and M. M. Maw, "Analysis of indoor channel propagation characteristics in multifloored building at 2.4 ghz," in *2017 21st International Computer Science and Engineering Conference (ICSEC)*, pp. 1–5, 2017.

[105] S. Y. Lim, Z. Yun, and M. F. Iskander, "Radio propagation measurements in multifloor indoor stairwells," in *2010 IEEE International Conference on Wireless Information Technology and Systems*, pp. 1–4, 2010.

[106] I. T. U. ITU-R, Rec. ITU-R P.1238-12, "Propagation data and prediction methods for the planning of indoor radiocommunication systems and radio local area networks in the frequency range 300 mhz to 450 ghz," August. 2023.

[107] V. D.-E. M. Buccioli, E. M. Vitucci, "Analysis of mm-wave scattering from construction materials," in *Proceedings of the XXXIVth URSI General Assembly and Scientific Symposium (URSI GASS 2021)*, pp. 1–4, 2021.

[108] D. Bonefačić and L. Šarolić, "Attenuation of building materials and structures in 5g millimeter wave band," in *2023 17th European Conference on Antennas and Propagation (EuCAP)*, pp. 1–5, 2023.

[109] N. Hosseini, M. Khatun, C. Guo, K. Du, O. Ozdemir, D. W. Matolak, I. Guvenc, and H. Mehrpouyan, "Attenuation of several common building materials: Millimeter-wave frequency bands 28, 73, and 91 ghz," *IEEE Antennas and Propagation Magazine*, vol. 63, no. 6, pp. 40–50, 2021.

[110] F. Taleb, G. G. Hernandez-Cardoso, E. Castro-Camus, and M. Koch, "Transmission, reflection, and scattering characterization of building materials for indoor thz communications," *IEEE Transactions on Terahertz Science and Technology*, vol. 13, no. 5, pp. 421–430, 2023.

[111] A. Asp, T. Hentilä, M. Valkama, J. Pikkuvirta, A. Hujanen, and I. Huhtinen, "Impact of different concrete types on radio propagation: Fundamentals and practical rf measurements," in *2019 4th International Conference on Smart and Sustainable Technologies (SpliTech)*, pp. 1–8, 2019.

[112] S. El Faitori and S. Salous, "Reflection and penetration loss wideband measurements of building materials at 28 ghz and 39 ghz," in *2022 16th European Conference on Antennas and Propagation (EuCAP)*, pp. 1–4, 2022.

[113] V. Degli-Esposti, F. Fuschini, E. M. Vitucci, and G. Falciasecca, "Measurement and modelling of scattering from buildings," *IEEE Transactions on Antennas and Propagation*, vol. 55, no. 1, pp. 143–153, 2007.

[114] P.-S. Kildal, *Foundations of Antenna Engineering: A Unified Approach for Line-of-Sight and Multipath*. Artech, 2015.

Appendix A

Anomalous reflection: computation of the wave curvature matrix

Let's consider a reference point P_0 on the RIS surface, and the corresponding position vector $\mathbf{r}'_0$. The phase of the incident ray in a point P with position vector $\mathbf{r}'$ located in the vicinity of P_0 can be approximated by its Taylor series expansion about P_0, truncated after the 2^{nd}-order term:

$$\begin{aligned}\psi^i\left(\mathbf{r}'\right) &\simeq \psi^i\left(\mathbf{r}'_0\right) + \hat{\mathbf{s}}^i\left(\mathbf{r}'_0\right)\cdot\left[\mathbf{r}'-\mathbf{r}'_0\right] \\ &+\frac{1}{2}\left[\mathbf{r}'-\mathbf{r}'_0\right]\cdot\left\{\underline{\mathbf{Q}}^i\left(\mathbf{r}'_0\right)\left[\mathbf{r}'-\mathbf{r}'_0\right]\right\}\end{aligned} \tag{A.1}$$

where the identities $\nabla\psi^i \equiv \hat{\mathbf{s}}^i$ and $\nabla\nabla\psi^i \equiv \underline{\mathbf{Q}}^i$ have been used, as stated in Section IIA. Similarly, the phase of the reflected field can be locally approximated as:

$$\begin{aligned}\psi^r\left(\mathbf{r}'\right) &\simeq \psi^r\left(\mathbf{r}'_0\right) + \hat{\mathbf{s}}^r\left(\mathbf{r}'_0\right)\cdot\left[\mathbf{r}'-\mathbf{r}'_0\right] \\ &+\frac{1}{2}\left[\mathbf{r}'-\mathbf{r}'_0\right]\cdot\left\{\underline{\mathbf{Q}}^r\left(\mathbf{r}'_0\right)\left[\mathbf{r}'-\mathbf{r}'_0\right]\right\}\end{aligned} \tag{A.2}$$

The same principle also applies to the phase χ^m imposed by the RIS:

$$\begin{aligned}\chi^m\left(\mathbf{r}'\right) &\simeq \chi^m\left(\mathbf{r}'_0\right) + \nabla\chi^m\left(\mathbf{r}'_0\right)\cdot\left[\mathbf{r}'-\mathbf{r}'_0\right] \\ &+\frac{1}{2}\left[\mathbf{r}'-\mathbf{r}'_0\right]\cdot\left\{\nabla\nabla\chi^m\left(\mathbf{r}'_0\right)\left[\mathbf{r}'-\mathbf{r}'_0\right]\right\}\end{aligned} \tag{A.3}$$

For a generic surface, any point P in the vicinity of P_0 is described by the following relation [70]:

$$\mathbf{r}' = \mathbf{r}'_0 + \mathbf{t} - \frac{1}{2}\left(\mathbf{t}\cdot\underline{\mathbf{C}}\mathbf{t}\right)\hat{\mathbf{n}} \tag{A.4}$$

where $\mathbf{t} = t_1\hat{\mathbf{u}} + t_2\hat{\mathbf{v}}$ is a vector tangent to the surface in $\mathbf{r}'_0$ and $\mathbf{C} = \kappa_1\hat{\mathbf{u}}\hat{\mathbf{u}} + \kappa_2\hat{\mathbf{v}}\hat{\mathbf{v}}$ is the curvature matrix of the surface. However, in the present work we are considering only flat surfaces ($\mathbf{C} = \mathbf{0}$), so $\mathbf{r}' - \mathbf{r}'_0$ will be a tangent vector to the surface, i.e.

$$\mathbf{r}' - \mathbf{r}'_0 = \mathbf{t} \tag{A.5}$$

By imposing the phase matching relation (3.18b) in the point P, we have then:

$$\begin{aligned} &\psi^r\left(\mathbf{r}'_0\right) + \hat{\mathbf{s}}^r \cdot \mathbf{t} + \frac{1}{2}\mathbf{t} \cdot \underline{\mathbf{Q}}^r \mathbf{t} = \psi^i\left(\mathbf{r}'_0\right) + \hat{\mathbf{s}}^i \cdot \mathbf{t} + \frac{1}{2}\mathbf{t} \cdot \underline{\mathbf{Q}}^i \mathbf{t} \\ &- \frac{1}{k_0}\left\{\chi^m\left(\mathbf{r}'_0\right) + \nabla\chi^m\left(\mathbf{r}'_0\right) \cdot \mathbf{t} + \frac{1}{2}\mathbf{t} \cdot \left[\nabla\nabla\chi^m\left(\mathbf{r}'_0\right)\mathbf{t}\right]\right\} \end{aligned} \tag{A.6}$$

and then, the following equations must be separately satisfied:

$$\psi^r\left(\mathbf{r}'_0\right) = \psi^i\left(\mathbf{r}'_0\right) - \frac{1}{k_0}\chi^m\left(\mathbf{r}'_0\right) \tag{A.7a}$$

$$\hat{\mathbf{s}}^r \cdot \mathbf{t} = \left[\hat{\mathbf{s}}^i - \frac{1}{k_0}\nabla\chi^m\left(\mathbf{r}'_0\right)\right] \cdot \mathbf{t} \tag{A.7b}$$

$$\mathbf{t} \cdot \underline{\mathbf{Q}}^r \mathbf{t} = \mathbf{t} \cdot \left\{\left[\underline{\mathbf{Q}}^i - \frac{1}{k_0}\nabla\nabla\chi^m\left(\mathbf{r}'_0\right)\right]\mathbf{t}\right\} \tag{A.7c}$$

Eq. (A.7a) just provides the phase matching on the reference position $\mathbf{r}'_0$. Eq. (A.7b) means that the tangent components of the 1^{st}-order terms of the Taylor's expansion are equal, as (A.7b) must be satisfied for any choice of the vector $\mathbf{t}$. So, using the projection operator $\underline{\mathbf{P}}_\tau = \underline{\mathbf{1}} - \hat{\mathbf{n}}\hat{\mathbf{n}}$ we get (3.12):

$$\begin{aligned} \underline{\mathbf{P}}_\tau \hat{\mathbf{s}}^r &= \underline{\mathbf{P}}_\tau \left[\hat{\mathbf{s}}^i - \frac{1}{k_0}\nabla\chi^m\left(\mathbf{r}'_0\right)\right] = \\ &= -\frac{\nabla\chi^i\left(\mathbf{r}'_0\right) + \nabla\chi^m\left(\mathbf{r}'_0\right)}{k_0} = -\frac{\nabla\chi\left(\mathbf{r}'_0\right)}{k_0} \end{aligned}$$

which leads to (3.13) by imposing $|\hat{\mathbf{s}}^r| = 1$.

Finally, by pre-multiplying and post-multiplying with the projection operator the 2^{nd}-order terms (curvature matrices) in (A.6), we immediately get (3.20):

$$\underline{\mathbf{P}}_\tau \underline{\mathbf{Q}}^r \underline{\mathbf{P}}_\tau = \underline{\mathbf{P}}_\tau \left[\underline{\mathbf{Q}}^i - \frac{1}{k_0}\nabla\nabla\chi^m\right]\underline{\mathbf{P}}_\tau$$

which leads to (3.21) by imposing $\underline{\mathbf{Q}}^r \hat{\mathbf{s}}^r = \mathbf{0}$.

Appendix B

Anomalous diffraction: computation of the wave curvature ρ^d

We proceed in a similar way as for reflection, by writing the Taylor series expansion of the phase functions of the incident and diffracted wave, respectively, about a point P_0 on the edge:

$$\begin{aligned}\psi^i(\mathbf{r}') &\simeq \psi^i(\mathbf{r}'_0) + \hat{\mathbf{s}}^i \cdot (\mathbf{r}' - \mathbf{r}'_0) \\ &+ \frac{1}{2}(\mathbf{r}' - \mathbf{r}'_0) \cdot \left\{ \underline{\mathbf{Q}}^i(\mathbf{r}'_0)\left[\mathbf{r}' - \mathbf{r}'_0\right] \right\}\end{aligned} \tag{B.1}$$

$$\begin{aligned}\psi^d(\mathbf{r}') &\simeq \psi^d(\mathbf{r}'_0) + \hat{\mathbf{s}}^d \cdot (\mathbf{r}' - \mathbf{r}'_0) \\ &+ \frac{1}{2}(\mathbf{r}' - \mathbf{r}'_0) \cdot \left\{ \underline{\mathbf{Q}}^d(\mathbf{r}'_0)\left[\mathbf{r}' - \mathbf{r}'_0\right] \right\}\end{aligned} \tag{B.2}$$

and similarly for the phase profile χ^m imposed by the RIS:

$$\begin{aligned}\chi^m(\mathbf{r}') &\simeq \chi^m(\mathbf{r}'_0) + \nabla\chi^m(\mathbf{r}'_0) \cdot (\mathbf{r}' - \mathbf{r}'_0) \\ &+ \frac{1}{2}(\mathbf{r}' - \mathbf{r}'_0) \cdot \left\{ \nabla\nabla\chi^m(\mathbf{r}'_0)\left[\mathbf{r}' - \mathbf{r}'_0\right] \right\}\end{aligned} \tag{B.3}$$

As we assume that the edge is rectilinear, we have

$$\mathbf{r}' - \mathbf{r}'_0 = ds\,\hat{\mathbf{e}} \tag{B.4}$$

and then, by imposing the *phase matching* relation

$$\psi^d(\mathbf{r}') = \psi^i(\mathbf{r}') - \frac{1}{k_0}\chi^m(\mathbf{r}') \tag{B.5}$$

e by substituting (B.1)-(B.4) into (B.5), we get:

$$\begin{aligned}
&\psi^i\left(\mathbf{r}_0'\right)+\hat{\mathbf{s}}^i\cdot\hat{\mathbf{e}}\,ds-\frac{\nabla\chi^m\left(\mathbf{r}_0'\right)}{k_0}\cdot\hat{\mathbf{e}}\,ds \\
&+\frac{1}{2}\left[\hat{\mathbf{e}}\cdot\underline{\mathbf{Q}}^i\left(\mathbf{r}_0'\right)\hat{\mathbf{e}}\right]ds^2-\frac{1}{k_0}\left[\hat{\mathbf{e}}\cdot\nabla\nabla\chi^m\left(\mathbf{r}_0'\right)\hat{\mathbf{e}}\right]ds^2 \\
&=\psi^d\left(\mathbf{r}_0'\right)+\hat{\mathbf{s}}^d\cdot\hat{\mathbf{e}}\,ds+\frac{1}{2}\left[\hat{\mathbf{e}}\cdot\underline{\mathbf{Q}}^d\left(\mathbf{r}_0'\right)\hat{\mathbf{e}}\right]ds^2
\end{aligned} \tag{B.6}$$

Finally, by equating separately the 0-order, 1^{st}-order and 2^{nd}-order terms, we obtain:

1. the phase matching in $\mathbf{r}_0'$:
$$\psi^i\left(\mathbf{r}_0'\right)=\psi^d\left(\mathbf{r}_0'\right) \tag{B.7}$$

2. the *generalized law of diffraction*:
$$\hat{\mathbf{s}}^d\cdot\hat{\mathbf{e}}=\cos\beta=\left(\hat{\mathbf{s}}^i-\frac{\nabla\chi^m}{k_0}\right)\cdot\hat{\mathbf{e}}=\cos\beta'-\frac{\nabla\chi^m}{k_0}\cdot\hat{\mathbf{e}} \tag{B.8}$$

3. the matching of the wave curvatures:
$$\hat{\mathbf{e}}\cdot\underline{\mathbf{Q}}^d\left(\mathbf{r}_0'\right)\hat{\mathbf{e}}=\hat{\mathbf{e}}\cdot\underline{\mathbf{Q}}^i\left(\mathbf{r}_0'\right)\hat{\mathbf{e}}-\frac{1}{k_0}\hat{\mathbf{e}}\cdot\nabla\nabla\chi^m\left(\mathbf{r}_0'\right)\hat{\mathbf{e}} \tag{B.9}$$

In (B.9), we observe that $\hat{\mathbf{e}}\cdot\underline{\mathbf{Q}}^i\left(\mathbf{r}_0'\right)\hat{\mathbf{e}}$ gives the ray curvature of the incident wave on the edge-fixed incidence plane (i.e. $1/\rho_e^i$), projected along the edge, i.e. multiplied by $\sin^2\beta'$, as the component of the edge direction along the ray gives no contribution, in accordance with (3.6). Therefore:

$$\hat{\mathbf{e}}\cdot\underline{\mathbf{Q}}^i\left(\mathbf{r}_0'\right)\hat{\mathbf{e}}=\frac{1}{\rho_e^i}\sin^2\beta' \tag{B.10}$$

and a similar relation holds for the diffracted wave:

$$\hat{\mathbf{e}}\cdot\underline{\mathbf{Q}}^d\left(\mathbf{r}_0'\right)\hat{\mathbf{e}}=\frac{1}{\rho^d}\sin^2\beta \tag{B.11}$$

Finally, recognizing that $\hat{\mathbf{e}}\cdot\nabla\nabla\chi^m\left(\mathbf{r}_0'\right)\hat{\mathbf{e}}$ is the 2^{nd} order derivative of χ^m along the edge direction, i.e.

$$\hat{\mathbf{e}}\cdot\nabla\nabla\chi^m\left(\mathbf{r}_0'\right)\hat{\mathbf{e}}\doteq\frac{\partial^2\chi^m}{\partial e^2} \tag{B.12}$$

and by substituting (B.10)-(B.12) into (B.9) we immediately get (3.26):

$$\frac{1}{\rho^d} = \frac{1}{\rho_e^i}\frac{\sin^2\beta'}{\sin^2\beta} - \frac{1}{k_0\sin^2\beta}\frac{\partial^2\chi^m}{\partial e^2}$$

Appendix C

Antenna-Array-Like macroscopic modeling

The modeling approach introduced here is a simplified, parametric method that, when properly tuned, can still provide realistic results, as described in more detail in [49]. To begin, the RIS is discretized into surface elements, and for each generic element at position (x,y) on the surface, a local power balance is defined. This ensures that the power amplitude, denoted as m_n, of each re-radiation mode of the metasurface is consistently defined relative to the incident power P_i :

$$P_i = \sum_{n=1}^{N} P_n m_n + P_i \tau \quad \Rightarrow \quad 1 = \sum_{n=1}^{N} m_n + \tau \tag{C.1}$$

Here, τ represents the fraction of the incident power dissipated as heat. A slightly more detailed version of equation (C.1) can be formulated to explicitly account for specular reflection and include the contribution of diffuse scattering, as discussed in [49], though this is omitted here for simplicity. It is important to note that typically, only one of the N re-radiation modes in equation (C.1) corresponds to the desired mode, with the others being parasitic. Additionally, all parameters in equation (C.1) theoretically vary as functions of position (x,y), due to the differing illumination angles at each surface element. However, under far-field illumination conditions, the incident wave can be approximated as planar, allowing the parameters in equation (C.1) to be treated as constants across the entire RIS. The parameters in (C.1) can be determined using Floquet's theory for locally periodic metasurfaces, obtained through measurements on a prototype, or computed using electromagnetic simulations. Once these parameters are established, the corresponding field contributions need to be calculated for each of the N reradiation modes. Focusing now on the generic n-th reradiation mode,

and omitting the subscript "n" for simplicity, the contribution of the metasurface to the reradiated field can be described by a spatial modulation coefficient. This coefficient can also be interpreted as a local reflection coefficient, with its expression given as:

$$\Gamma_m(x,y) = \sqrt{m} \cdot A(x,y) e^{j\chi_m(x,y)} \tag{C.2}$$

where $A(x,y)$ and $\chi_m(x,y)$ are the amplitude and phase profiles that the RIS imposes on the reradiated field. Note that amplitude term $A(x,y)$ has been introduced to account for power-transfer effects due to surface waves in non-local metasurfaces: $A(x,y)$ is normalized as it must satisfy:

$$\iint_S A(x,y)\, ds = S_{RIS}\,; \quad A(x,y) \equiv 1 \tag{C.3}$$

for PGM metasurfaces. To compute the reradiated field of the finite-size metasurface, we use a discrete Huygens-based approach, which models the metasurface as a 2-dimensional antenna array. RIS is divided into surface elements, denoted as ΔS, and for simplicity, we assume equal spatial sampling, such that :

$$\Delta S = \Delta x \Delta y = \Delta l^2 \tag{C.4}$$

Each surface element is treated as an ideal aperture antenna element that receives the incident power P_i and reradiates a spherical wavelet with power $P_m = mA^2 P_i$, based on a specified radiation pattern. The wavelets emitted by all surface elements combine coherently, taking into account both their amplitude and phase, to produce the overall reradiated wavefront. To prevent the occurrence of grating lobes, it is essential that $\Delta l \leq \lambda/2$. This approach relies on classical antenna theory, utilizing the concepts of effective aperture A_m and antenna directivity gain $D_m = A_m 4\pi/\lambda^2$ for both the reception and reradiation of each antenna element. The radiation pattern, along with the parameters D_m and A_m, must adhere to the following physical constraint:

$$A_m \leq \Delta S = \Delta l^2 \tag{C.5}$$

If the condition in (C.5) were violated, the power received and reradiated by a square meter of an infinite LIS surface could exceed the incident power, which would be physically impossible. Since an aperture antenna must have a directivity gain greater or equal to 3 [114], it must be:

$$3 \leq D_m = A_m \frac{4\pi}{\lambda^2} \Rightarrow \frac{3\lambda^2}{4\pi} \leq A_m \leq \Delta l^2 \Rightarrow \Delta l \geq \frac{\sqrt{3}\lambda}{2\sqrt{\pi}} = 0.49\lambda \tag{C.6}$$

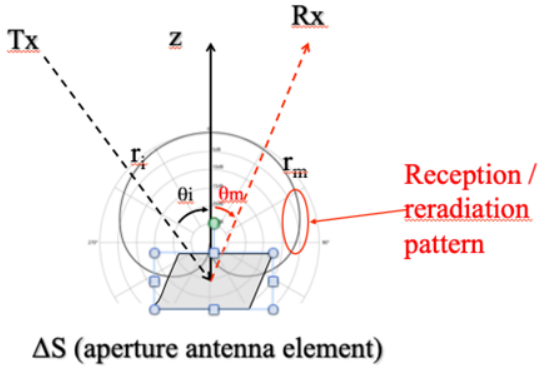

Fig. C.1 Generic antenna element, its cardioid-shaped radiation pattern and the Tx/Rx geometry

If we combine (C.5) and (C.6), we conclude that the only possible spacing step that is physically sound is $\Delta l \simeq \lambda/2$. An antenna that naturally complies with this condition is the Huygens source, whose directivity gain is $D_m = 3$ and whose antenna pattern is

$$f(\theta_m) = \left(\frac{1+\cos\theta_m}{2}\right)^2 \tag{C.7}$$

The electric field intensity $|\Delta E_m|^2$ of the generic antenna element must therefore be:

$$|\Delta E_m|^2 = |\Delta E_{m0}|^2 \left(\frac{1+\cos\theta_m}{2}\right)^2 \tag{C.8}$$

where $|\Delta E_{m0}|^2$ is an amplitude factor to be computed.

With reference to C.1, in order to satisfy the power balance at the generic surface element, we demand that:

$$\begin{aligned} P_m = \Gamma_m^2 P_i = mA^2 \frac{|\Delta E|^2}{2\eta} A_m(\theta_i) = mA^2 \frac{|\Delta E|^2}{2\eta} \frac{3\lambda^2}{4\pi} \left(\frac{1+\cos\theta_i}{2}\right)^2 \\ = \int_{2\pi} \frac{|\Delta E|^2}{2\eta} r_m^2 d\Omega = \int_0^{\frac{\pi}{2}} \int_0^{\pi} \frac{\Delta E_{m0}^2}{2\eta} \left(\frac{1+\cos\theta_m}{2}\right)^2 r_m^2 \sin\theta_m d\phi_m d\theta_m \end{aligned} \tag{C.9}$$

Thus:

$$\begin{aligned} mA^2 |\Delta E_i|^2 \cdot 3\frac{\lambda^2}{4\pi} \left(\frac{1+\cos\theta_i}{2}\right)^2 = \\ 2\pi \Delta E_{m0}^2 r_m^2 \int_0^{\frac{\pi}{2}} \left(\frac{1+\cos\theta_m}{2}\right)^2 \sin\theta_m d\theta_m \end{aligned} \tag{C.10}$$

If the primary source is a transmitter of power and antenna gain P_t and G_t, respectively, we have:

$$\Delta E_t|^2 = \frac{60 P_t G_t}{(r_i)^2} \tag{C.11}$$

Therefore, (C.10) can be easily solved to yield the closed-form solution:

$$\Delta E_{m0}^2 = mA^2 \frac{60 P_t G_t}{(r_i r_m)^2} \left(\frac{3\lambda^2}{8\pi}\right) (1+\cos\theta_i)^2 \tag{C.12}$$

and therefore

$$|\Delta E_m|^2 = mA^2 \frac{60 P_t G_t}{(r_i r_m)^2} \left(\frac{3\lambda^2}{16\pi}\right) (1+\cos\theta_i)^2 (1+\cos\theta_m)^2 \tag{C.13}$$

Here, (C.13) gives the reradiated field intensity of the generic surface element of reradiation coefficient m. It is important to note that since the maximum effective aperture of the Huygens source (for $\theta_i = 0$) is $A_m = 3\frac{\lambda^2}{4\pi}$, and for $\Delta l = \lambda/2$, we have:

$$\Delta S = \left(\frac{\lambda}{2}\right)^2 = \frac{\pi}{3} A_m \approx 1.047 A_m \tag{C.14}$$

The Huygens antenna element will not capture exactly the whole power incident on ΔS and, therefore, the field in (C.13) will correspond to a reradiation coefficient slightly lower than mA^2. This small gap can be compensated by multiplying the field intensity in (C.13) by $\frac{\pi}{3}$, or by considering a surface discretization with a slightly smaller spacing:

$$\Delta l = \frac{\lambda}{2} \cdot \frac{1}{\sqrt{\pi/3}} \tag{C.15}$$

Expression in (C.13) only gives the field intensity, as it is derived from a simple power balance. The phase of coefficient (C.2) must now be applied. Moreover, a proper polarization vector must also be applied to account for the polarimetric properties of the reradiated field. The coherent field contribution of the discrete element located at (x,y) to the field in P can therefore be written as:

$$\Delta E_m(P|x,y) = \frac{\sqrt{m \cdot 60 P_t G_t}}{r_i \cdot r_m} \cdot A(x,y) \cdot e^{j\chi_m(x,y)} \cdot \frac{3\lambda}{16\pi} (1+\cos\theta_i)(1+\cos\theta_m) \cdot e^{-jk(r_i+r_m)} \cdot \hat{p}_m \tag{C.16}$$

The total reradiated field at P can be expressed as a coherent summation of the discrete field contributions ΔE_m:

$$E_m(P) = \sum_{u=1}^{N_x} \sum_{v=1}^{N_y} \Delta E_m\left(P|x = u\Delta l, y = v\Delta l\right) \tag{C.17}$$

and the sum is performed on $N_x \times N_y$ antenna elements, where $N_x = L_x/\Delta l$ and $N_y = L_y/\Delta l$, with L_x and L_y being the linear dimensions of the surface along x and y, respectively. Although the number of elements to be considered can be large, the computation of (C.17) is easily parallelizable on today's parallel computing platforms such as Graphic Processing Units (GPU) or multi-core CPUs, in order to achieve good computation speed. In essence, the Antenna-Array-Like model is a parametric, simple model that relies on a proper parameterization of the metasurface to describe the reradiated field with a simple formula. In reference, far-field illumination cases, parameters m, X_m, and $\hat{p}_m$ can be easily defined and considered constant over the surface.